Application of a Rate Dependent Cohesive Zone Model to Predict Impact Response in Adhesively Bonded Ultra-High Strength Steel Tubes

by

Yi Brian Liu

A thesis

presented to the University of Waterloo

in fulfillment of the

thesis requirement for the degree of

Master of Applied Science

in

Mechanical and Mechatronics Engineering

Waterloo, Ontario, Canada, 2019

I hereby declare that I am the sole author of this thesis. This is a true copy of the thesis, including any required final revisions, as accepted by my examiners.

I understand that my thesis may be made electronically available to the public.

Abstract

The design of multi-material lightweight vehicle (MMLV) structures incorporating structural adhesive joining requires advanced CAE supported by material characterization and computational model validation at the component level. In this thesis, tailored hot stamped (THS) ultra-high strength steel (UHSS) hat sections were joined using structural epoxy adhesive and tested under quasi-static and dynamic loading rates. The experiments were modelled numerically using an existing adhesive model with a cohesive zone method (CZM) formulation that was previously validated at the coupon level. The objectives of this study were two-fold: (i) to assess the performance of adhesive-only joints for UHSS structures; and (ii) to validate the CZM of the adhesive at the structural level.

Three configurations of hot stamped Usibor® 1500-AS hat sections with varying strength and ductility (martensitic, soft flange, and three zone) were joined to form closed tubular structures (tubes) using a two-part toughened epoxy adhesive (IRSA 07333, 3M) applied to the flanges, with a bond line thickness of 0.178mm (0.007"). A custom fixture was used to secure the hat sections while oven-curing the adhesive (80°C for 30 minutes). The tubes were loaded in three-point bend, axial crush, and a novel Mode I opening (Caiman) configuration. Numerical models of the experiments were solved using an explicit dynamic finite element code (LS-DYNA R7.1.2). For validation of the adhesive model at the structural level, the simulated experiments were assessed based on global metrics such as overall loading response, peak load, energy absorption, displacement to failure, visual deformation mode. Where possible, crack extension along the adhesive joint was measured and compared to the model response.

In general, all the experiments for various test conditions exhibited good repeatability in loading response and deformation pattern. One exception was the three-point bend experiments, which demonstrated an asymmetric deformation mode that considerably increased displacement to failure. While the models had difficulty in predicting displacement to failure, the predicted peak loads were in good agreement (7.14%). The axial crush models had good agreement in predicted deformation pattern, peak load (11.5%), and energy absorption (7.65%), but over predicted energy absorption of dynamic three zone model due to excessive oscillation. The Caiman models correlated well with the experiments (within 5%) and provided a controlled Mode I loading for model validation of predicting crack extension.

This work demonstrated that THS UHSS joined with structural adhesives can achieve consistent loading response in support of model validation, and that surface preparation and specimen manufacture were critical factors in reducing test variability. One limitation with this study was that it proved difficult to assess the performance of the adhesive model when the response was dominated by the metal components, since the accuracy of the overall response could be limited by the fidelity of the steel constitutive model. With the exception of a few cases, the CZM adhesive model was able to predict the structural response of bonded components within 16%, based on kinetics and kinematics measured in the experimental tests.

Acknowledgements

I would like to express my profound gratitude to my supervisors Duane Cronin and Michael Worswick, for providing an excellent opportunity to tackle a challenging, yet rewarding project. Their insight and guidance throughout this journey has been invaluable to my personal development.

I would also like to thank Eckhard Budziarek, Tom Gawel, Andy Barber, Neil Griffett, Ryan George, Kaab Omer, Cameron O'Keeffe, Cale Peister, Brock Watson, Chi-Hsiang Liao, and Jose Imbert for all the assistance I was given in the lab, as well as supporting me in conducting all my experimental testing safely and efficiently. Also, special thanks to Chi-Hsiang Liao, as well as the rest of the IMMC crew for all the fun times together in group social events.

Support for this research from Honda R&D Americas, ArcelorMittal, 3M, Canada Foundation for Innovation, Ontario Research Fund, Ontario Centres of Excellence, Ontario Advanced Manufacturing Consortium and the Natural Sciences and Engineering Research Council is also gratefully acknowledged.

Finally, I would like to thank my parents and friends for the support and words of encouragement. Also, a big thanks to Dawn Liao for putting up with all my rants about this thesis, providing emotional support, and for being the best travel companion I needed when recharging my batteries.

Table of Contents

List of Tables

List of Figures

Chapter 1 Introduction

A major driver of innovation in the automotive industry is the mandate to meet ever increasing standards for fuel efficiency, such as the corporate average fuel economy (CAFE) target of 54.5 mpg by the year 2025, without compromising overall vehicle safety (U.S. Department of Transportation, 2012). For multi-material lightweight vehicle (MMLV) structures, these requirements have led to consideration of the use of advanced materials such as hot stamped ultra-high strength steel, aluminum, magnesium, and composites (U.S. Department of Energy, 2015). An example of this is the body-in-white (the assembled sheet metal components of the vehicle structure) of the 2014 Audi A8 (Figure 1.1), in which different materials are strategically distributed in the structure to maximize crashworthiness while minimizing weight.

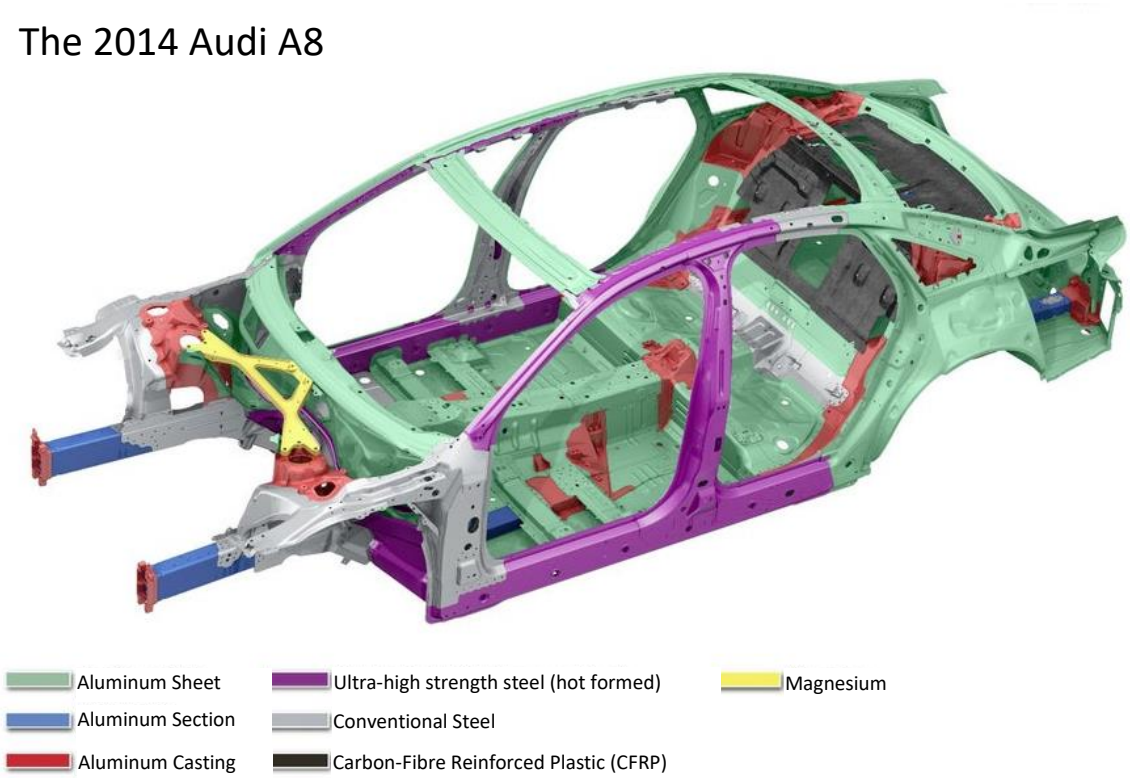

Figure 1.1: The body-in-white of the 2014 Audi A8, demonstrating the strategic use of different materials in a lightweight, crash-optimized structure (ArcelorMittal USA, 2014)

The growing demand for light weight structures has sparked the development of advanced joining techniques for dissimilar materials (Chastel and Passemard, 2014). One such technique is the use of structural adhesives, which has demonstrated a wide array of potential benefits owing to the continuous nature of adhesive joints, including: a large stress-bearing area to reduce stress concentrations and improve joint stiffness; a physical barrier to prevent galvanic corrosion between dissimilar materials; sealing the structure for improved weather resistance; and improved noise, vibration, and harshness (NVH) performance for cabin comfort (He, 2011; Symietz, 2005). In light of these structural and sealing properties, the adhesives have seen increased use in joining automotive structures (Marzi *et al.*, 2009). Evidence of this growth can be found in vehicles such as the 2015 Ford F-150, which used three times the amount of adhesive compared to the previous model (Hagerty and Ramsey, 2014). The 2018 Honda Accord used structural adhesives extensively to increase body torsional and bending rigidity by 32 and 24 %, respectively, improving dynamic performance and ride quality over the previous model (Honda Canada, 2017). In addition, adhesive bonding technologies enabled the "carbon core" construction technique in the 2016 BMW 7-series sedan, in which carbon fiber reinforced polymer composites were bonded to an ultra-high strength steel and aluminum chassis to create a body-in-white with high strength and rigidity, while maintaining light weight and low center of gravity (Benevento, 2016).

While aluminum, magnesium, and composite materials are important candidates for use in achieving lightweight structures, the material cost of steel is considerably lower and ultra high strength steel (UHSS) components can be achieved through the manufacturing process of hot stamping (Mori *et al.*, 2017). In the hot stamping process, steel blanks are pre-heated for

austenization, then hot formed and quenched between cooled dies in a single process, to produce components with a fully martensitic microstructure, exceeding 1500 MPa in strength (Liu *et al.*, 2011; Vaissiere, Laurent, and Reinhardt, 2002). In addition, different microstructures (bainite, ferrite, and pearlite) can be achieved by reducing the cooling rate through the use of heated tooling. By controlling the cooling rate throughout the tooling, components with tailored properties (a strategic distribution of microstructures) can be achieved by a combination of heated and cooled regions within the tooling in a process known as tailored hot stamping (THS) (Merklein *et al.*, 2016). Therefore, the use of hot stamped UHSS will be a critical component of any MMLV structure. However, one challenge facing the use of hot stamped UHSS components in MMLVs is the difficulty in joining them with other materials through traditional methods such as welding or mechanical fasteners involving deformation, due to their high strength (Chastel and Passemard, 2014).

Experimental testing in vehicle development cycles can be time and resource intensive, and therefore the finite element (FE) method is widely used analysis and design tool for assessing vehicle structures (He, 2011; da Silva and Campilho, 2012). As a result, widespread adoption of adhesive joining in vehicle structures requires improved predictive capabilities of FE software to aid CAE engineers in design and analysis of bonded components (Gowda *et al.*, 2017), with a primary requirement being the characterization of adhesives for use in numerical models (Deb *et al.*, 2016; Gowda *et al.*, 2017). To accurately predict the behavior of adhesive joints in the FE environment, the material model must possess the required mechanical properties (*e.g.* stiffness and strength) as well as the fracture toughness of the adhesive in Mode I and Mode II loading (May et al., 2015). These properties are often determined by a variety of coupon level

tests (da Silva and Campilho, 2012) and the subsequent model validation at the coupon level involves simulating the tests used to obtain the model parameters or by simulating another coupon test and comparing against an independent set of experimental data. For validation at the structural level however, no existing study in the literature investigated the validation of a cohesive zone adhesive model derived from material testing, at the component level that involved a wide variety of structural tests at both quasi-static and dynamic deformation rates. In addition, no studies have addressed the adhesive joining of UHSS components to the author's knowledge.

1.1 Objectives, Approach and Outline

The primary objective of this thesis was to validate an existing rate-dependent adhesive model based on the cohesive zone modelling (CZM) formulation (Watson *et al.*, 2018), previously developed from material testing and validated at the coupon level, at the structural level by applying it to a range of modes of loading and varying loading rates. To achieve this objective, adhesively joined hat sections of UHSS (Usibor® 1500-AS) were subjected to three loading scenarios: three-point bend, creating shear (Mode II) loading along the neutral axis of the double-hat section tubes, and mimicking the lateral loading of B-pillar components; axial crush, creating a complex mixed mode loading often experienced within critical energy absorption components at the front of a vehicle; and an adhesively bonded variant of the Caiman test (O'Keefe, 2018) creating Mode I opening at the adhesive joint. Three-point bend and axial crush experiments were tested under quasi-static and dynamic conditions, while the Caiman test specimens were evaluated under quasi-static conditions. Finite element models of the

experiments were created and solved in a commercial finite element code (LS-DYNA R7.1.2, LSTC) to assess the ability of the adhesive model (Watson *et al.*, 2018) in describing the response and failure of the structures.

This thesis is organized by background knowledge of adhesives properties, numerical modelling of adhesives, structural testing of bonded components, the THS process, modelling of THS process, and structural testing of THS components. Followed by experimental testing of bonded UHSS tubes in Chapter 3, detailing the test conditions, sample preparation, and test setup. Chapter 4 outlines the numerical modelling methods used in this work, including the material models of the UHSS and the adhesive, as well as boundary conditions. Chapters 5 and 6 present the experimental and numerical modelling results with discussion, respectively. Chapter 7 wraps up the thesis with conclusions and recommendations for future work.

Chapter 2 Background

2.1 Adhesives

Adhesives are substances capable of joining different parts together by means of a chemical bond between the parts, and are widely used in many industries (Landrock and Ebnesajjad, 2008). Although adhesives have been used throughout human history, derived in ancient times primarily from plant or animal sources (Adhesives & Sealants, 2015), modern adhesives were only developed in the last century with advancements in organic chemistry and polymerization processes (Landrock and Ebnesajjad, 2008). There currently exist a wide range of adhesives for a large variety of applications, and while there is no universally recognized classification, some general categories include alloy, elastomeric, film and tape, hot-melt, rubber-based, water-based, thermoplastic, thermosetting and more (Landrock and Ebnesajjad, 2008). Examples of commonly used adhesives include cyanoacrylates, polyamides, polyurethanes, silicone, epoxies to name a few. Many different types of adhesives are used in the automotive industry, such as anaerobic adhesives for thread locking mechanical fasteners (Landrock and Ebnesajjad, 2008), and structural adhesives for load bearing applications are often based on epoxies, acrylics, urethanes, and cyanoacrylates (3M, 2012). In general, epoxies can be formulated to have the best overall properties for metal bonding, with the right combination of strength, toughness, flexibility, as well as temperature resistance (3M, 2012), and will therefore be the focus of this background section.

2.1.1 Epoxy Adhesives

Epoxy adhesives are classified as thermosetting polymers and are the most commonly used adhesive due to their versatility in formulating to a wide range of specifications to meet various bonding requirements in automotive, aerospace, construction, and more (Landrock and Ebnesajjad, 2008; Petrie, 2006). They are often used as a single part system, requiring high heat for curing, or a two-part system with resins and hardeners that can cure at room temperature (Landrock and Ebnesajjad, 2008). In addition, epoxy adhesives form strong bonds between most materials, and can be engineered to develop specific properties through the use of hardeners, resins, resins, modifiers, and fillers, making them an excellent choice for a wide range of structural applications (Landrock and Ebnesajjad, 2008). Epoxies are inherently brittle (Yahyaie *et al.*, 2013) and are often toughened by the inclusion of reactive liquid rubbers (elastomeric additives) in order to introduce rubber particle precipitates as a second phase (Yee and Pearson, 1986).

2.1.2 Surface Preparation

The formation of a strong adhesive joint may require treatments of the bonding surfaces, depending on the materials being joined. Surface treatment methods generally involve increasing the adhesive contact area by roughening the surface and cleaning the adherend to remove any potential contaminates (Landrock and Ebnesajjad, 2008).

Surface roughening techniques found in the literature include mechanical abrasion, chemical etching, electromechanical treatments, and laser texturing (Landrock and Ebnesajjad, 2008). Most have demonstrated that, in general, adhesive joint strength increases with increasing

surface roughness for metallic adherends (Lonardo and Bruzzone, 1989; Budhe *et al.*, 2015). Although more sophisticated techniques such as laser treatment can enhance the bond strength relative to mechanical abrasion methods (Zhang, Yue, and Man, 1997), the latter includes processes such as grit blasting, which has been demonstrated in certain cases to be effective in treating metallic surfaces with a corrosion resistant coating while being simple and economical (Liao *et al.*, 2017; Liu *et al.*, 2017)

Solvents that are often used to clean adherend surfaces include methyl ethyl ketone, acetone, and methanol (Landrock and Ebnesajjad, 2008).

2.1.3 Adhesive Joint Failure Modes

Bonded systems can fail either cohesively, in which cracks grow entirely within the adhesively layer, or adhesively (commonly referred as interfacial failure), in which the cracks grow along an adhesive-to-adherend interface thereby causing debonding (Figure 2.1) (Landrock and Ebnesajjad, 2008). In material testing of adhesives to construct a constitutive model, it is often desirable to have the bonded samples fail cohesively, as this ensures the full strength of the adhesive is achieved in the joint, rather than interfacial failure in which the lower interface strength dominates the joint strength. Therefore, a properly treated surface should maximize the likelihood of achieving cohesive failure to ensure that the maximum strength of the adhesive is achieved during testing.

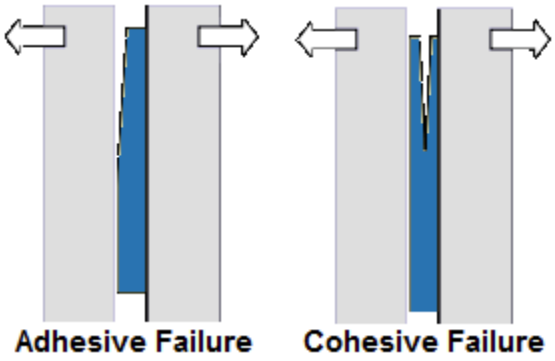

Figure 2.1: Failure modes of an adhesive joint (Steiner, 2011)

2.2 Adhesive Material Properties

An adhesive joint can experience several stress states (Figure 2.2), and while typical loading conditions often involve a combination of these states, coupon level tests for material characterization aim to produce a singular stress state to measure specific properties (Landrock and Ebnesajjad, 2008; Watson et al., 2018). The stress states, and therefore the measured material properties, of an adhesive are dependent on the mode of loading to which the joint is subjected (Figure 2.3), described as tension (Mode I), in-plane shear (Mode II), and a less commonly encountered out-of-plane shear (Mode III).

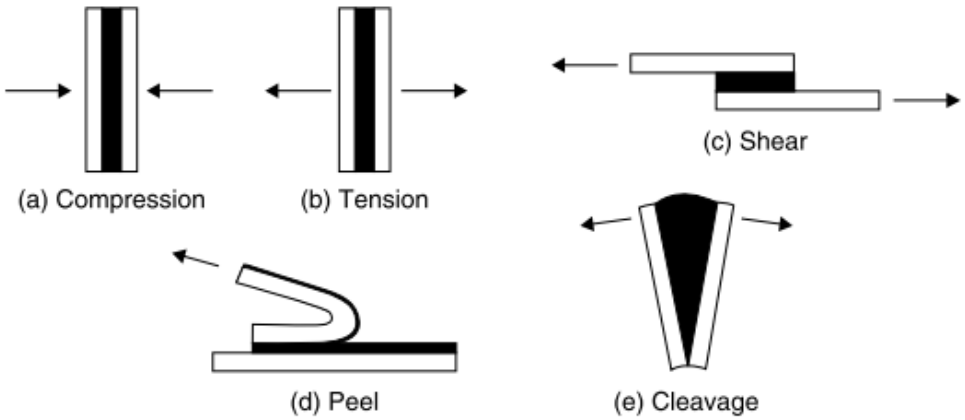

Figure 2.2: Stress states of an adhesive joint (Shields, 1984)

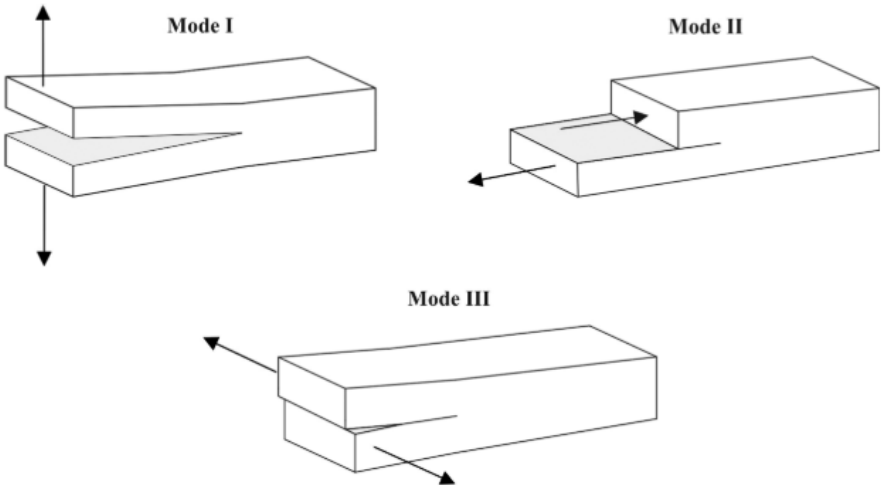

Figure 2.3: Modes of loading in an adhesive joint (Chaves et al., 2014)

The properties of an adhesive required for material models often include the Young's modulus, the tensile and shear strengths, and the fracture toughness (more specifically the energy release rate) in Mode I and Mode II (May *et al.*, 2015). Acquisition of this data requires an abundance of tests to be carried out, including bulk adhesive testing, fracture characterization tests, and coupon level tests for tensile and shear response (May *et al.*, 2015).

2.2.1 Mode I Mechanical Property Characterization

Traditionally, the Mode I critical energy release rate (G_{IC}) of an adhesive is obtained from standardized mechanical tests, namely double cantilever beam (DCB) (ISO 25217, 2009) and tapered double cantilever beam (TDCB) (ASTM D3433-99, 2014). In both tests, two bonded beams are loaded in tension until crack propagation is observed in the joint, and the Irwin-Kies equation (Ripling, Mostovoy, and Patrick, 1964) can be used to calculate the critical energy release rate. However, to fully define a traction separation response in Mode I, additional testing is required to obtain the peak traction and initial stiffness, which is often done by

conducting butt-joint testing. Moreover, to accurately describe the adhesive behavior over a wide range of loading scenarios, high rate testing is required to develop a strain rate-dependent material model. This poses a challenge for the DCB and TDCB tests since the standardized specimens have a high mass and can therefore potentially introduce inertial effects when loaded at a higher velocity (Watson *et al.*, 2018).

To address these challenges, Dastjerdi, Tan, and Barthelat (2013) proposed a method to directly measure the Mode I traction-separation response with a single test, using a rigid double cantilever beam (RDCB) geometry. This technique was initially applied to measure the traction-separation response of soft biological adhesives (Dastjerdi *et al.*, 2012), then later adapted to structural adhesives (Watson *et al.*, 2018). To satisfy the rigid adherend assumption, the material was chosen to be steel, which had significantly higher stiffness than the adhesive, with a geometry corresponding to a large second moment of area. Moreover, to minimize inertial effects for future dynamic testing, the geometry of the test samples was specifically designed to minimize mass while maximizing bending stiffness. The analysis conducted by Dasterdi (Figure 2.4), assumed that the adherends would rotate about the far end of the sample away from the loading pins, such that the entire joint was in tension.

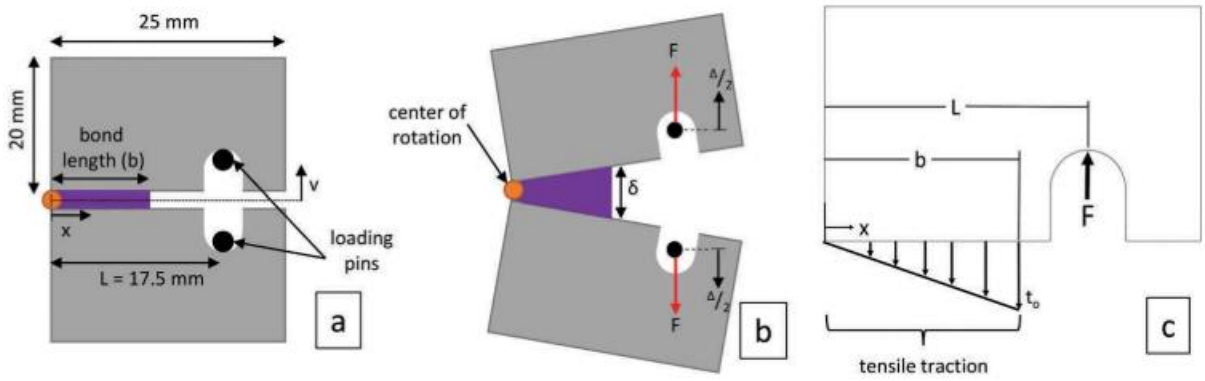

Figure 2.4: Analysis of RDCB developed by Dastjerdi, showing the dimensions (a), load applied (b), and free body diagram (c) (Watson et al., 2018)

Early FE analysis by Watson *et al.* (2018), however, discovered that part of the joint was in compression. Therefore, the analysis was modified such that the center of rotation was arbitrarily displaced a distance μ from the far end of the sample away from the loading pin (Figure 2.5). Given a set of load point opening displacement and experimental force-displacement data, an expression was derived to solve for μ and to generate the corresponding Mode I traction-separation response of the adhesive.

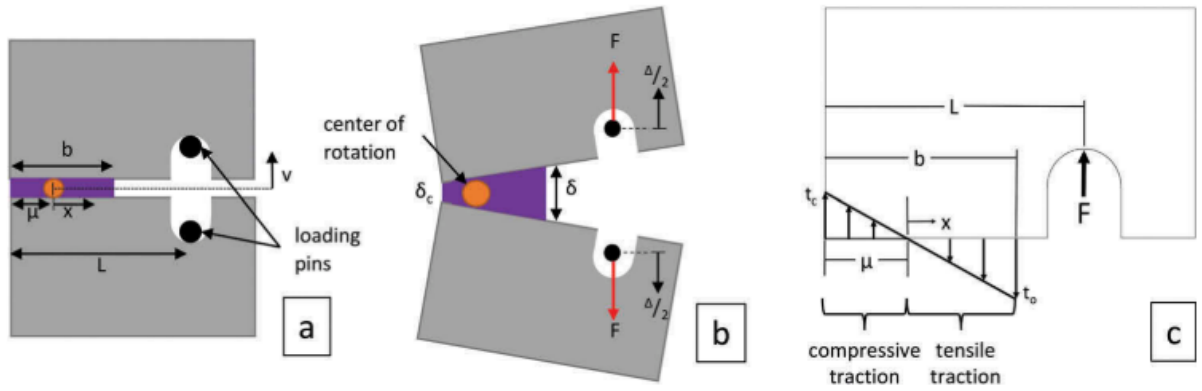

Figure 2.5: Enhanced RDCB analysis (a), sample kinematics (b), and free body diagram (c) (Watson *et al.*, 2018)

2.2.2 Mode II Mechanical Property Characterization

The Mode II critical energy release rate (G_{IIC}) is generally obtained by conducting the end notch flexure (ENF), end-loaded split (ELS) or the four-point end-notched flexure (4ENF) test (Cricrì, 2018). The ELS test is reported to have a source of variability due to the need to clamp down an edge of the specimen, thereby increasing the complexity of data reduction, while the 4ENF involves a complex setup and the results are affected by proper compliance calibration as well as friction (Schuecker and Davidson, 2000; da Silva and Campilho, 2012). Hence, the ENF is one of the most commonly used tests for obtaining the Mode II fracture properties and has been used by Alfredsson, Biel, and Salimi (2015), Arrese *et al.* (2019), and Fernandes *et al.* (2015) with success. However, the ENF is still susceptible to unstable crack growth if the specimen dimensions were not accurately selected. Moreover, similar to Mode I characterization, the shear strength of the adhesive needs to be obtained through additional tests, usually the single- or thick-adherend lap shear, making this process time and resource intensive. While single-lap shear is the most commonly used joint configuration due to its simplicity in design and manufacture, the rotation of the joint (Figure 2.6) during loading induces peel stress that can affect the accuracy of shear strength characterization (Kelly, 2004). The thick-adherend lap shear test reduces bending of the adherends, thereby reducing mixed mode loading, and can therefore produce better shear data (Boqaileh, 2015).

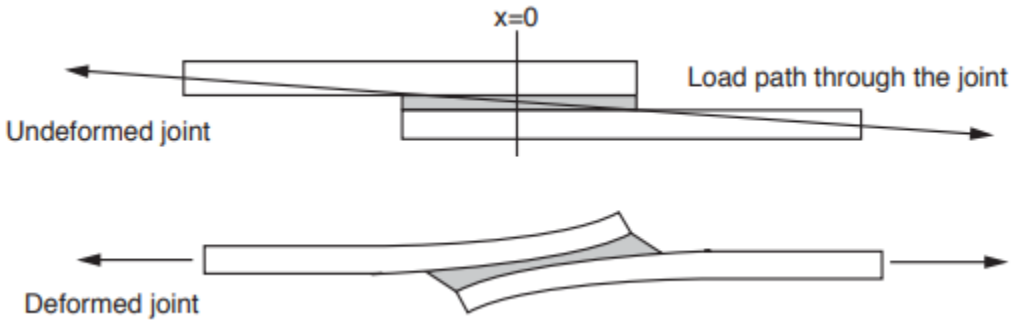

Figure 2.6: Undeformed and deformed single-lap joint, demonstrating the rotation of the joint due to the bending of adherends, inducing peel stress in the joint (Kelly, 2004)

To overcome these limitations, bonded shear samples, based on a modified geometry of the thick-adherend lap shear, were fabricated and tested to obtain the force-displacement response in shear loading for various strain rates (Watson *et al.*, 2018). In addition, the joint deformation and crack propagation were optically tracked so that a full Mode II traction-separation response could be defined with a single test, bypassing the traditional fracture characterization tests (Watson *et al.*, 2018).

2.3 Numerical Modelling of Adhesive Joints

The FE method is the most widely used numerical method for analysis of bonded adhesive joints and is built on the concept of discretizing a body into many elements (da Silva and Campilho, 2012). This technique was first pioneered by Hrennikoff (1941) and Courant (1943). Further advancements were made with the rapid development of computing power and the extensive use of the technique in the aerospace industry, and now the FE method is a critical component of many engineering analyses (da Silva and Campilho, 2012). Adhesive joints can be

represented numerically by tiebreak contacts, cohesive elements, and continuum solid elements (Dogan *et al.*, 2012; Trimino and Cronin, 2016) (Figure 2.7).

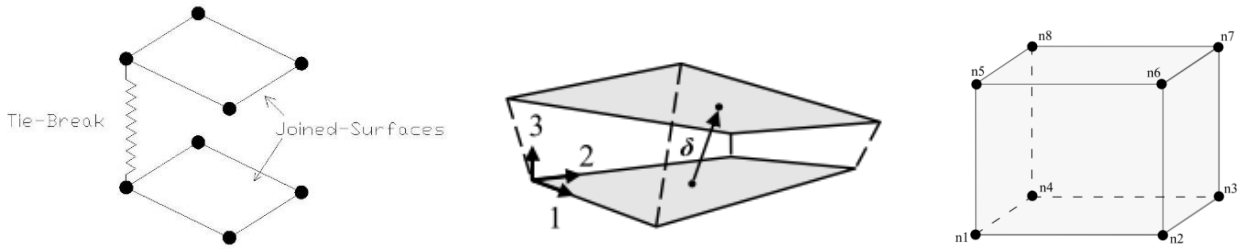

Figure 2.7: Element types to numerically represent an adhesive joint include tiebreak (left) cohesive element (center) and solid continuum elements (right) (LSTC, 2012)

Typically, an adhesive joint can be most accurately represented by a large number of solid elements, often requiring multiple layers of elements through the thickness of the joint (Boqaileh, 2015). However, this approach can be cost prohibitive as it is time and resource intensive computationally (Zachariah, 2006). Alternatively, tiebreak contacts can be used to represent an adhesive joint with minimal computational resources (Trimiño, 2012). In simple terms, a tiebreak contact can be conceived as springs joining nodes on one body to nodes on an adjacent body. Tiebreak contacts share the same behavior as other common types of contact definitions under compressive loads, but could be defined with a failure criterion in tension to simulate separation of the joined surfaces (Zachariah, 2006). Although tiebreak contacts are simple and efficient numerical implementations, they are known to have numerical instabilities commonly referred to as “unzipping” (Trimiño and Cronin, 2016). Unzipping is a phenomenon in which a large portion of the load is held by the first element in a crack front, and once the element deleted due to a failure criterion, the load is immediately released and passed onto the next element, which will likely cause it to fail and delete as well, resulting in a rapid non-

physical crack propagation behavior (Trimiño, 2012). While this issue can be addressed with the addition of damage criteria to promote gradual unloading during failure, tiebreak contacts generally lack the inclusion of strain-rate effects, making them unsuitable for impact simulations (Trimiño and Cronin, 2016). More recently, cohesive zone modelling (CZM) was developed to address the limitations of the tiebreak contact (da Silva and Campilho, 2012), and is capable of capturing the elastic behavior of the joint as well as the damage accumulation process by means of a traction-separation law (Marzi *et al.*, 2009). Although the CZM is a more comprehensive approach compared to the tiebreak method, requiring additional material properties, it has been shown to be capable of producing accurate results when compared to solid element implementations while being more computationally efficient (Trimiño and Cronin, 2016). As such, the CZM is widely used in the analysis of bonded joints (da Silva and Campilho, 2012).

2.3.1 Cohesive Zone Modelling

The CZM technique uses both material strength and energy parameters to simulate the material response, damage accumulation, and material fracture process (da Silva and Campilho, 2012). CZM can be applied in the local approach (Figure 2.8), where cohesive elements represent a zero volume path (*i.e.* a surface) where damage may accumulate, usually between the adhesive and the adherend, and the constitutive behavior of the adhesive is simulated by solid elements (da Silva and Campilho, 2012). This is useful for numerically modelling the interfacial (adhesive) failure that occurs during the debonding of the adherend from the adhesive. Alternatively, CZM can be applied in the continuum approach (Figure 2.8), whereby a

single layer of cohesive elements models the equivalent response of the entire adhesive joint, including damage accumulation (da Silva and Campilho, 2012). This approach is computationally efficient due to its inherent simplicity, while being capable of predicting material response in Mode I and Mode II loading, provided that the CZM law parameters are thoroughly and accurately calibrated (Watson *et al.*, 2018). Therefore, this technique has been widely used in the damage modelling of bonded joints. A study was done by Campilho, de Moura, and Domingues (2005) comparing the two CZM approaches in modelling the response of a plastic wedge-opened double-cantilever beam test. They noted that although the simpler continuum approach underestimated the bond toughness, for most applications, where thin adhesive layers made of tough or moderately tough epoxies were used, the approach provides reasonably good results while minimizing computational cost.

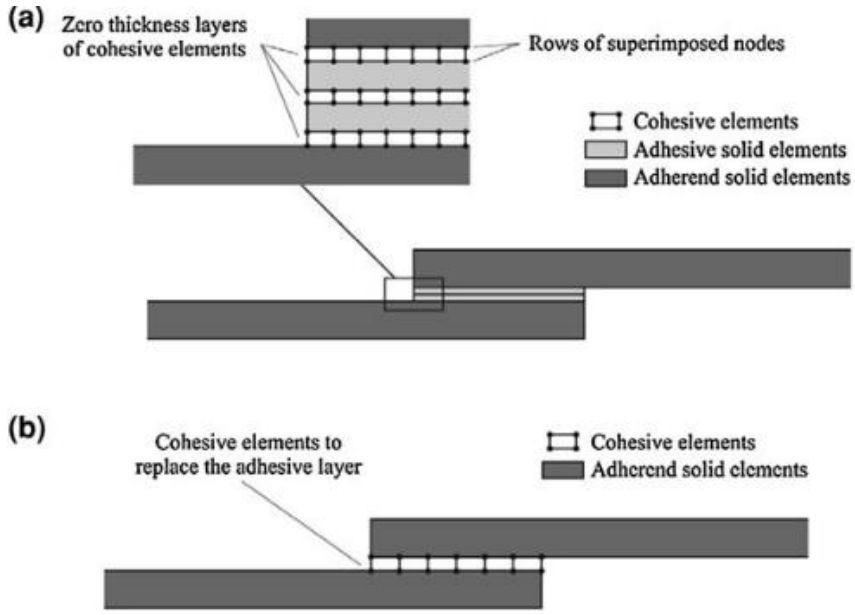

Figure 2.8: (a) Local approach of CZM, with adhesive and adherend solid elements joined by zero thickness cohesive elements and (b) continuum approach of CZM, where cohesive elements represent the adhesive itself and its thickness (da Silva and Campilho, 2012)

CZM simulate the loading of an adhesive joint and the subsequent progressive unloading, due to material damage, through the use of traction-separation laws (da Silva and Campilho, 2012). The traction-separation (stress-displacement) response (Figure 2.9) of adhesive joints are often trapezoidal or bilinear (triangular shape) (da Silva and Campilho, 2012). To properly select the appropriate response to use, Campilho *et al.* (2013) investigated the effect of cohesive law shape in predicting the loading response of a single-lap joint bonded with a brittle and a ductile adhesive. They concluded that cohesive law shapes have a significant effect on joints bonded with ductile adhesives, noting that the trapezoidal response better described the damage accumulation (plastic flow) process. On the other hand, the cohesive law shape had a minimal effect on predicting the response of brittle adhesives.

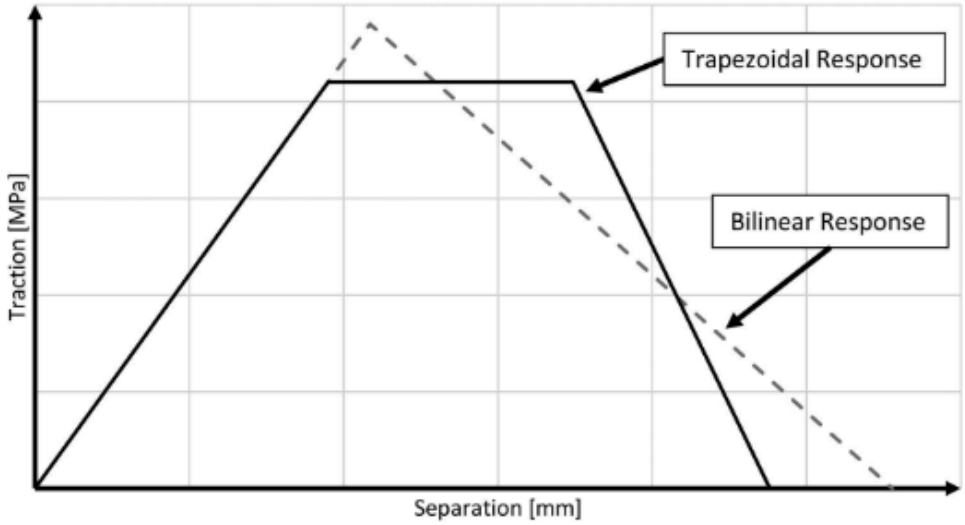

Figure 2.9: Examples of cohesive traction-separation law shape (Watson et al., 2018)

Regardless of the cohesive law shape, the basic formulation of the CZM approach is such that the traction-separation load curves (TSLC) (Figure 2.10) in Mode I and II are defined by the material stiffness prior to onset of damage, peak tractions T and S at the onset of damage

accumulation, and critical energy release rates G_I^C and G_{II}^C (area under traction-separation curve) (Watson *et al.*, 2018; LSTC, 2012). Based on these definitions, the maximum separation (displacement to failure) δ_I^F and δ_{II}^F for a CZM is given by:

$$\delta_I^F = \frac{G_I^C}{A_{TSLC} \cdot T} \quad , \quad \delta_{II}^F = \frac{G_{II}^C}{A_{TSLC} \cdot S}$$

where A_{TSLC} is the area under a normalized traction-separation curve. In general, each mode of loading requires its own traction-separation curve, and while a mixed-mode response (Figure 2.11) can be modeled, the exact "mode-mixity" formulation is dependent on the specific constitutive model being used.

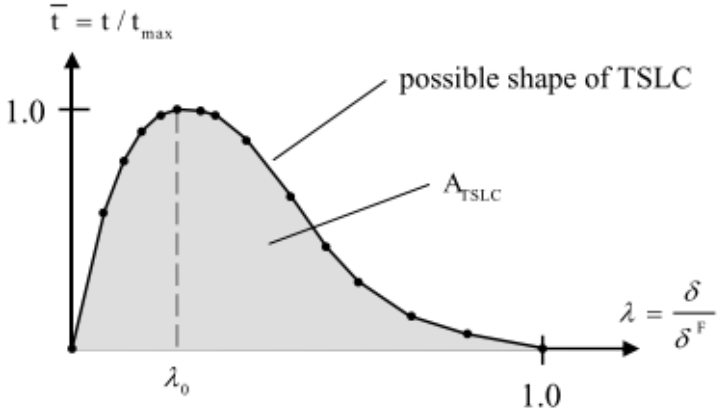

	Mode I	Mode II
t_{max}	T	S
δ^F	$\frac{G_I^c}{A_{TSLC} T}$	$\frac{G_{II}^c}{A_{TSLC} S}$
G^c	G_I^c	G_{II}^c

Figure 2.10: An arbitrary normalized traction-separation law and the parameters required to define it (LSTC, 2012)

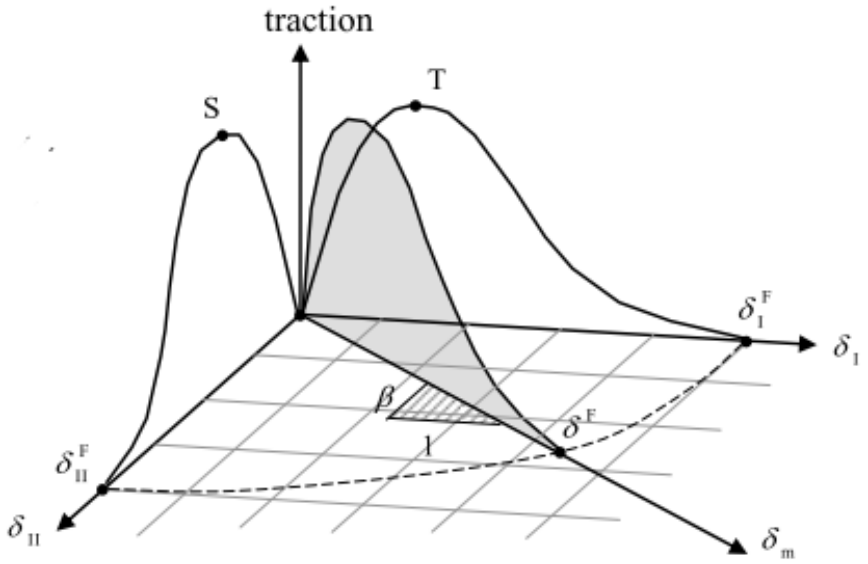

Figure 2.11: Visualization of a full traction-separation law, including mixed-mode response (LSTC, 2012)

The material model used in this work was implemented in LS-DYNA as MAT_240, which utilized a tri-linear elastic-ideally plastic traction-separation law (Figure 2.12) and accounted for strain rate effects. In addition to the usual CZM parameters, the ratio of plastic deformation to the total deformation (area under flat region over the total area under tri-linear curve) needed to be determined in order to define the precise shape of the cohesive law (Marzi *et al.*, 2009, Watson *et al.*, 2018).

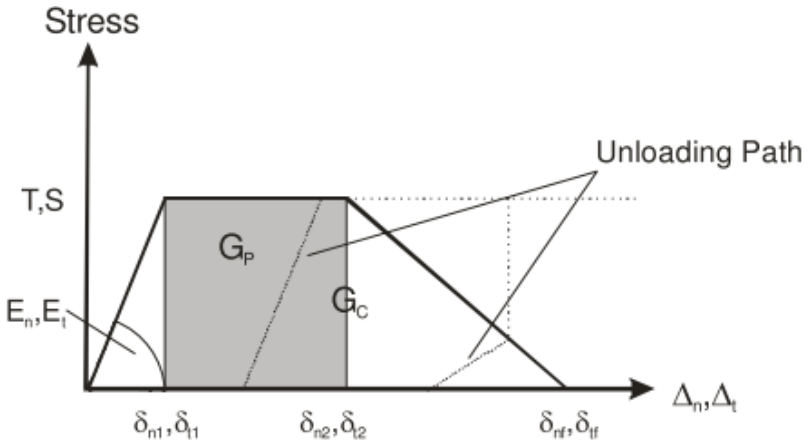

Figure 2.12: Parameters defining precise shape of a tri-linear traction-separation law (LSTC, 2012)

2.4 Testing and Numerical Modelling of Adhesively Joined Structures

In addition to experimentally studying the impact response of adhesively joined structures, it is of critical importance to develop numerical models capable of predicting their impact response. An extensive study conducted by Lanzerath and Pasligh (2014) investigated an adhesive modelling approach incorporating both cohesive elements and simplified contact definitions. The model was first calibrated in a single element simulation, assuming only cohesive failure, then the same model was used to simulate coupon tests, component tests, substructures and eventually a full vehicle, after which the predictions were compared to experimental data. However, the experiments were primarily focused on utilizing weld bonding (hybrid joints comprising adhesives and spot welds) to reduce the total number of spot welds in representative or actual automotive components, while maintaining or surpassing the performance of purely spot welded components in energy absorption. Furthermore, there was limited information on the adhesive characterization process, and the adhesive-only

component level validation lacked different test modes before proceeding to larger scale testing with weld bonding.

A study conducted by May *et al.* (2015) investigated the characterization of an adhesive to develop a fully rate-dependent model using an extended CZM formulation, then validating the model at the component level by simulating a T-joint impact test (Figure 2.13) as well as a T-peel test.

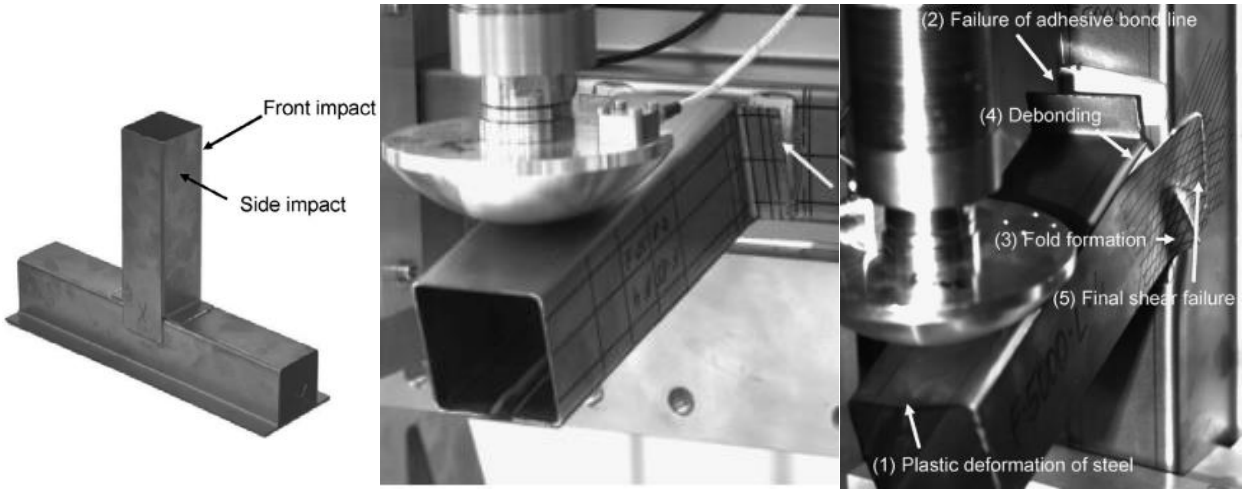

Figure 2.13: T-joint impact directions (left), and resulting deformation during frontal impact (center) and side impact (right) (May et al. 2015)

Normally, constant strain rate is assumed upon damage initiation, and the traction-separation law is fixed throughout the entire damage accumulation process. This assumption may not always be valid, and therefore the authors extended the traditional CZM formulation to continuously update the shape of the traction-separation curves. While both the extended and traditional CZM formulated models were in good agreement with the T-joint experiments, the extended formulation performed noticeably better (5-10%) in the T-peel test. However, the authors noted that this was due to relatively high variation in local strain rate in a T-peel

adhesive joint and could not conclude if the extended formulation would universally perform better in other load cases. In addition, while the T-joint had the versatility of testing two modes of loading in a single geometry, the loading was primarily isolated to the adhesive joint, as opposed to the combined deformation response (adhesive and adherend) of a bonded structure representative of an automotive component.

Other studies that focused on the systematic development and validation of an adhesive model at the component level included an investigation by Yang *et al.* (2012) in which a simplified FE model was developed for toughened adhesive joints, that was validated at the coupon level with single lap shear (SLS), double lap shear (DLS), and coach peel (CP) specimens and then at the structural level with dynamic axial impact on a hexagonal tube. A single part, heat-curing, crash-toughed epoxy adhesive was cast into bulk dog bone samples that were tested at quasi-static and dynamic rates to obtain the stress-strain response of the adhesive under uniaxial tension at various strain rates. A modified isotropic elasto-plasticity model (*MAT_SPOTWELD) was used to model the adhesive response in a finite element code (LS-DYNA 971), in which the stress-strain response was simplified to bilinear curves with the Young's Modulus and yield strength defined as functions of effective strain rate. However, the adhesive model was based on a von Mises failure criterion such that the shear response was linked to the tensile response, which was generally applicable to metals but could be inaccurate for many polymeric materials (Trimiño and Cronin, 2016). Moreover, the authors omitted a damage law in the adhesive model, since the material failure strain was far smaller than the steel adherends used (DP600 and DP780) and it was assumed that the joint softening due to damage would be a negligible in the overall structural response. The component level validation of a double-hat hexagonal tube

(Figure 2.14), with a 0.25 mm bond line thickness modeled with a single layer of solid elements, axially impacted by a 276 kg rigid wall travelling at 10.15 m/s resulted in good correlation in terms of force-displacement, energy absorption, and deformation pattern. Despite the good correlation, this simplified model had limited versatility since the lack of damage law based on the assumption of relatively small failure strain of the adhesive may not be applicable to a wide range of adherend materials, particularly UHSS.

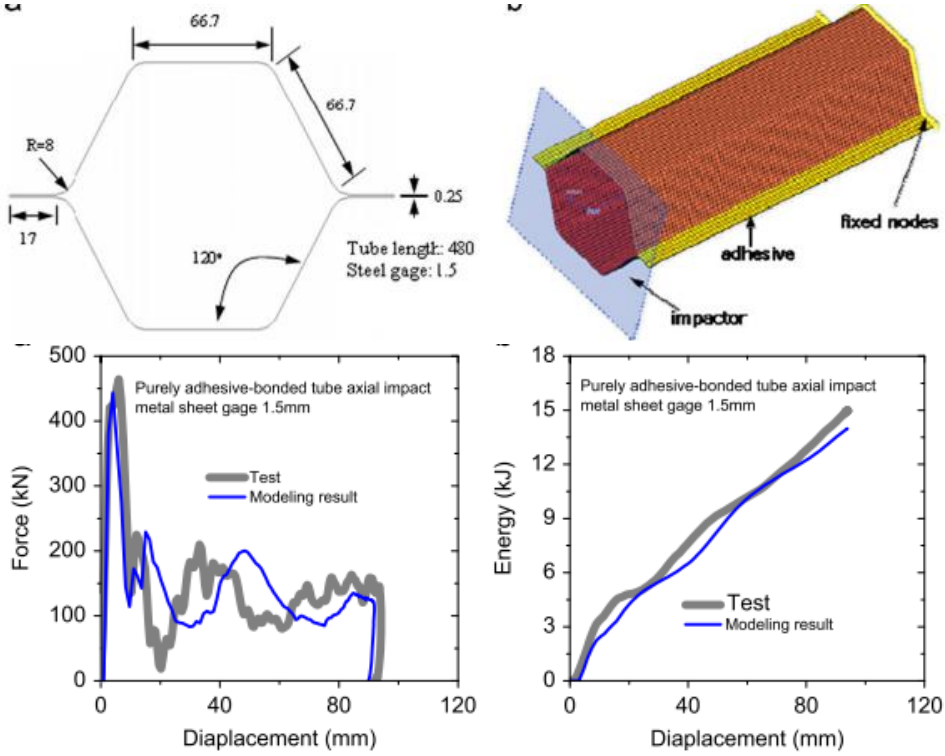

Figure 2.14: Dimensions and numerical setup of bonded tube (top), measured vs. simulated force and energy-displacement response of axial impact (bottom) (Yang et al. 2012)

Another study similar to the current work was conducted by Gowda *et al.* (2017), in which development and validation of an adhesive model was done at the coupon level before simulating a dynamic axial compression experiment using a drop tower to impact adhesively bonded double-hat section tubes. A general purpose epoxy-based adhesive (Araldite AV198,

Huntsman) with a hardener (HV998) was modeled using MAT_024 (PIECEWISE LINEAR PLASTICITY) and a single layer of solid elements with a von Mises yield criterion in LS-DYNA. An existing curve describing the post-yield stress *versus* effective plastic strain behavior was digitized and assigned to the material model, and the Cowper-Symonds parameters describing the strain rate effect were obtained from a similar epoxy-based adhesive. The resulting simulation of single lap shear and T-peel tests demonstrated good correlation with the experiments. For validation at the structural level, double-hat section tubes made of mild steel were joined with a bond line thickness of 0.3mm and axially compressed with a 134 kg impactor at a velocity of 4.3 m/s. The predicted force-displacement response (Figure 2.15) was in good agreement with the experiment, and the predicted peak load, mean load, and energy absorbed were all within 5% of experimentally measured values. Similar to the study by Yang *et al.* (2012), the limitations of the study by Gowda et al. (2017) included use of von Mises yield criterion and lack of damage law in the adhesive model.

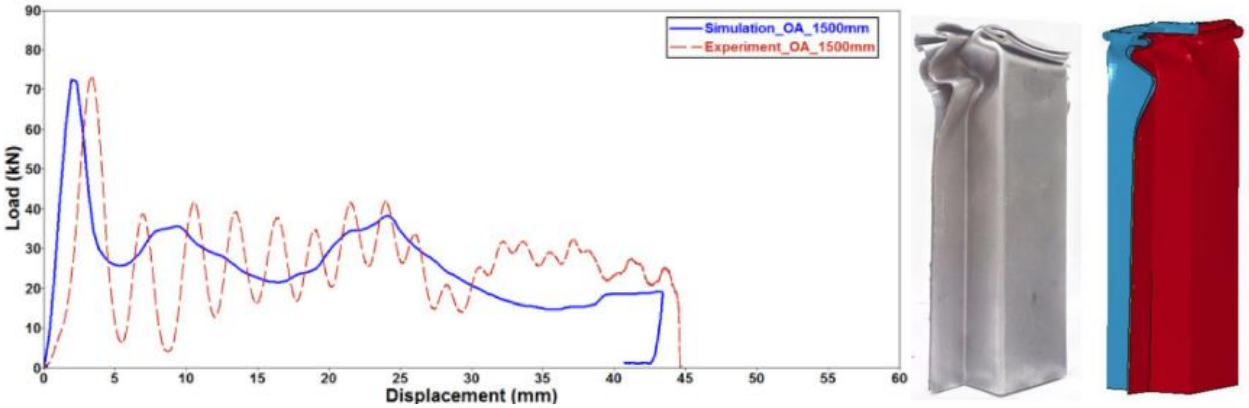

Figure 2.15: Comparison of measured and simulated force-displacement response for bonded tubes under axial impact (left), and comparison of deformed specimen and predicted deformation (Gowda et al. 2017)

In a study by Trimiño and Cronin (2014), dynamic axial impact of sub-scale adhesively joined double-hat section tubes made of DP800 steel were investigated. The objective of the study was to evaluate the application of the non-direct similitude (NDS) technique to bonded structures, in which scaled up numerical models of the tubes under axial impact were validated against experimentally tested sub-scaled tubes. An inherent limitation of the study was the equipment, in which the drop tower used for the dynamic axial impact lacked sufficient amount of energy to generate multiple folds in the tube. The NDS calculations also did not account for the adhesive layer, and while it was found to be acceptable in this particular specimen geometry, the authors noted that there may be cases where a second material had a more significant role in the overall structural response. A key outcome of the study was the demonstration that CZM elements provided a good representation of adhesive joints. A follow-on study (Boqaileh, 2015) drew a similar conclusion, whereby adhesive joint represented with cohesive elements using bulk material and coupon-level test data was able to efficiently predict structural response and failure of bonded joints.

Although a multitude of studies can be found in the literature regarding impact testing of adhesively joined structures, most are focused on benchmarking the crashworthiness of bonded structures relative to other joining methods (Peroni, Avalle, and Belingardi, 2009; Lee, Kim, and Oh, 2006, or even hybrid joining methods involving adhesives (Mcgregor, Seeds, and Nardini, 1990; Deb *et. al*, 2016; Gowda *et al.*, 2018). Few studies have been found that addressed the adhesive bonding of UHSS components. There is also a lack of published research considering three-point bending (lateral impact) of adhesively joined double-hat section tubes. The one study conducted by Gowda *et al.* (2018) investigated impact response of double-hat

section tubes when they were joined with adhesive, spot welds, and weld bonding (Figure 2.16). However, this study was mainly focused on benchmarking the different types of joining methods, and did not characterize or model the adhesively bonded structures subjected to loading. Of the studies that focused on adhesive modelling and component level validation, the adhesive model properties were often not derived from thorough material testing or lacked damage mechanics formulations due to simplifications, or that different types of component level experiments at different strain rates were omitted (Steidler, Bonde, Ljungquist, 2003; Lanzerath, Nowack, Mestres, 2009).

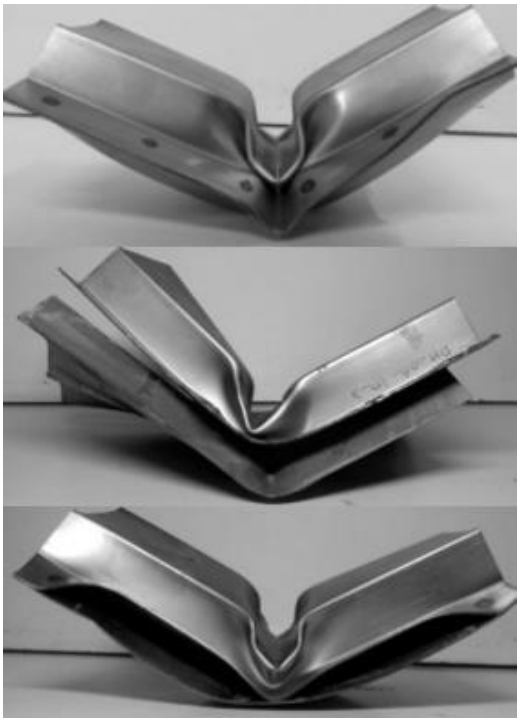

Figure 2.16: Double-hat section joined with spot welds only (top), adhesively only (middle), and weld bonded (bottom) (Gowda *et al.*, 2018)

2.5 Tailored Hot Stamping of Boron Steel

The motivation for the development of hot stamping was initially to produce steel sheet components with a fully martensitic microstructure, allowing ultra-high strength parts of complex geometry to be formed at elevated temperatures. Performing this operation at room temperature would be impossible due to the low ductility of martensite. To this end, steel blanks are heated to austenization temperatures before hot forming with chilled dies, since a high cooling rate is required to produce a martensitic microstructure. It was later discovered that by altering the temperature of the forming tooling, different cooling rates could be achieved resulting in different microstructures in the as-formed part (Liu *et al.*, 2011), as seen from the continuous cooling transformation (CCT) diagram in Figure 2.17 (Bardelcik et al., 2010). While any steel sheets with high quenchability can be hot stamped, the 22MnB5 boron steel (commercially referred to as Usibor®1500-AS) manufactured by ArcelorMittal is a commonly used steel grade for hot stamping due to their high quenchability (Mori *et al.*, 2017). In the as-received condition, Usibor® 1500-AS has an aluminum-silicon (Al-Si) intermetallic coating to provide corrosion protection, and to prevent oxidation and decarburization during the hot stamping process (Eller *et al.*, 2014). While this Al-Si coating also provides enhanced weldability of the hot stamped components (Mori *et al.*, 2017), the coating may result in interfacial failure within adhesive joints and removal was recommended prior to adhesively joining components (Liao et al., 2017; Liu et al., 2017).

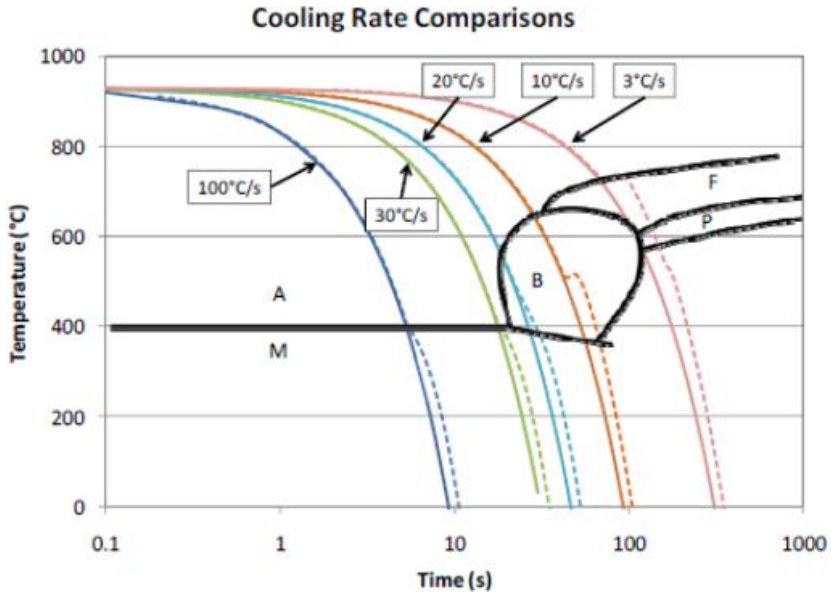

Figure 2.17: A continuous cooling transformation diagram for Usibor® 1500-AS (George, 2011)

The process of tailoring a component by controlling the temperature at different regions of the tooling to obtain different properties for specific functions is known as In-Die Heating (IDH) Tailoring. For a given automotive component, a more ductile region can be obtained by heating that specific portion of the tooling and maintaining the desired temperature. This achieves a lower cooling rate, which results in more formation of bainite and ferrite. In areas where intrusion resistance is critical, the same component can have regions of high strength martensite, accomplished by a high cooling rate maintained with water channels through those regions of the tooling. The primary advantage of THS is the ability to produce components with variable hardness distribution to optimize for crash performance and passenger safety.

2.5.1 Numerical Modelling of Tailored Hot Stamping of Usibor® 1500-AS

Before these modern hot stamped components can be fully exploited for their potential, it was critical to develop reliable predictive models to accurately capture their crash response (Eller *et al.*, 2014). To accomplish this, the distribution of material properties throughout the part must be accurately predicted, therefore complex forming simulations (Figure 2.18) were developed to model the decomposition of austenite into bainite, ferrite, or martensite. One such model was developed by Åkerström, Bergman, and Oldenburg (2007) and implemented in LS-DYNA commercial finite element software, which had been shown to be able to predict the final phase composition and micro-hardness distribution of the formed component to reasonable degree of accuracy. Using a modified version of the Åkerström model, Omer *et al.* (2017) developed a methodology to numerically model the THS process, which was divided into four sequential stages: transfer, forming, quenching, and cooling. Each stage involved an independent simulation and the output of the previous simulation was fed into the next. Each of the four stages utilized a coupled thermo-mechanical solver, in which the mechanical solver determined the strains, stresses, and deformation in each element, while the thermal solver determined temperature profiles and heat flow in each node and element. The mechanical solver also received thermal properties from the thermal solver, which were then used to calculate thermal stresses and strains, as well as to predict micro-hardness in the part based on cooling rates. The final material properties of the steel were developed based on the predicted micro-hardness.

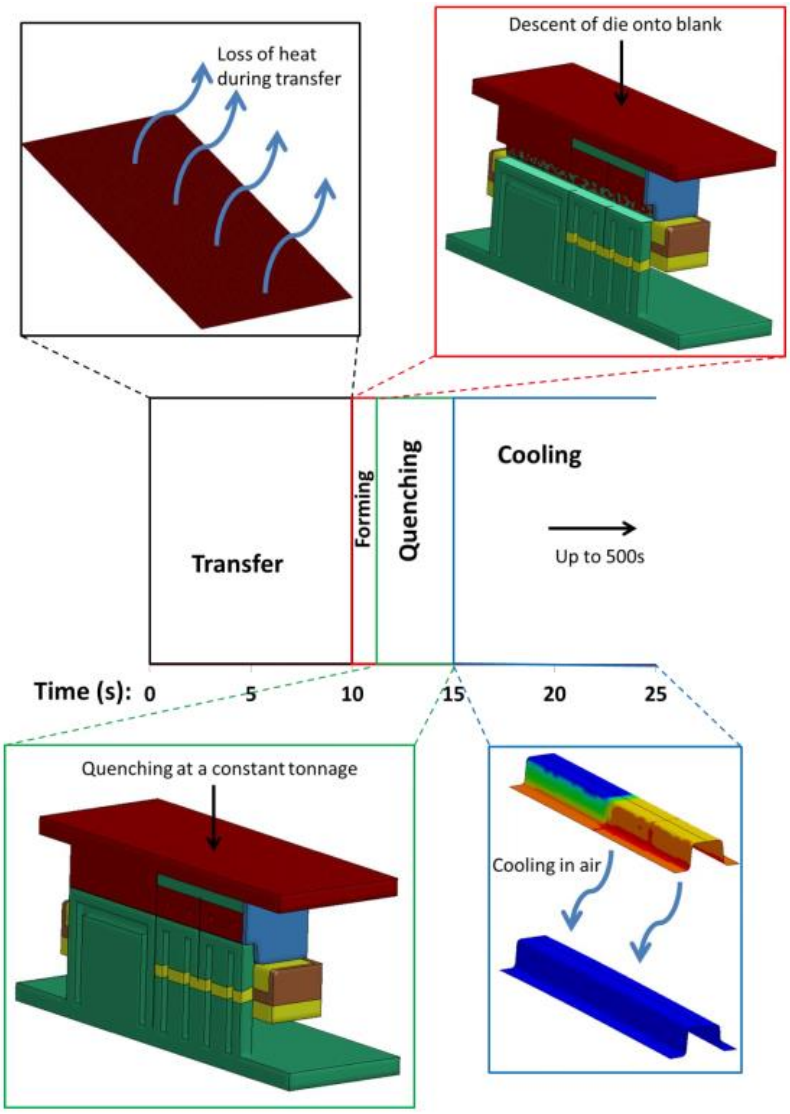

Figure 2.18: Stages of the THS process in the numerical model

To characterize a constitutive material model for the predicted tailored microstructures, Bardelcik *et al.* (2012) used a phenomenological approach by assuming a Voce hardening model and that the coefficients are functions of the micro-hardness (Vickers hardness). This model was referred to as the Tailored Crash Model (TCM). While the flow stress responses predicted by TCM for different micro-hardnesses at different strain rates are in good agreement with the experiments (Figure 2.19), this model alone is insufficient in accurately predicting the deformation of a component. The ability to predict initiation of cracks is also important in

complex loading conditions found in crash events, therefore the fracture behavior must be characterized and accounted for in the material model as well. The Generalized Incremental Stress State Dependent Damage Model (GISSMO) (Haufe *et al.*, 2010) is a commonly used phenomenological damage (fracture) model that uses Equation (1) to define damage by a scalar damage variable D. Equation (1) consists of a user defined damage exponent *n*, the plastic strain at failure (ε_f) as defined by a set of fracture *loci*, and the equivalent plastic strain (ε_p). ten Kortenarr (2016) characterized a set of fracture *loci* for Usibor® 1500-AS various tailor hot stamped conditions (Figure 2.20). A regularization scheme could also be specified within GISSMO to scale the fracture curves according to element size, since the rate of plastic strain accumulation is mesh dependent.

$$\Delta D = \left(\frac{n * D^{\left(1-\frac{1}{n}\right)}}{\varepsilon_f} \right) \varepsilon_p \tag{1}$$

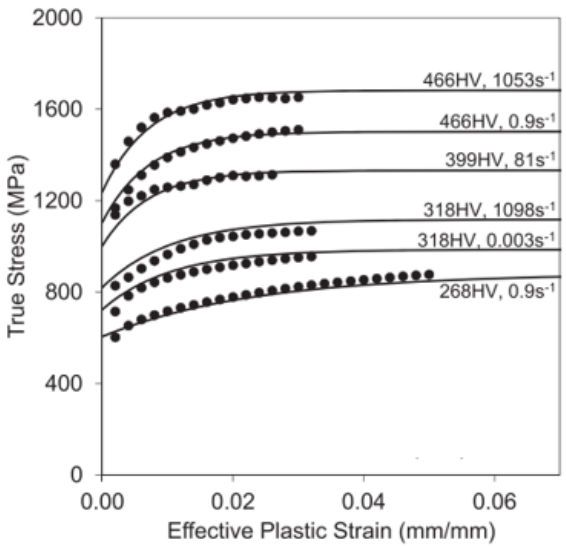

Figure 2.19: Comparison between predicted (solid line) and measured (dotted line) flow stress curves for various Vickers hardness and strain rates (Bardelcik *et al.* 2012)

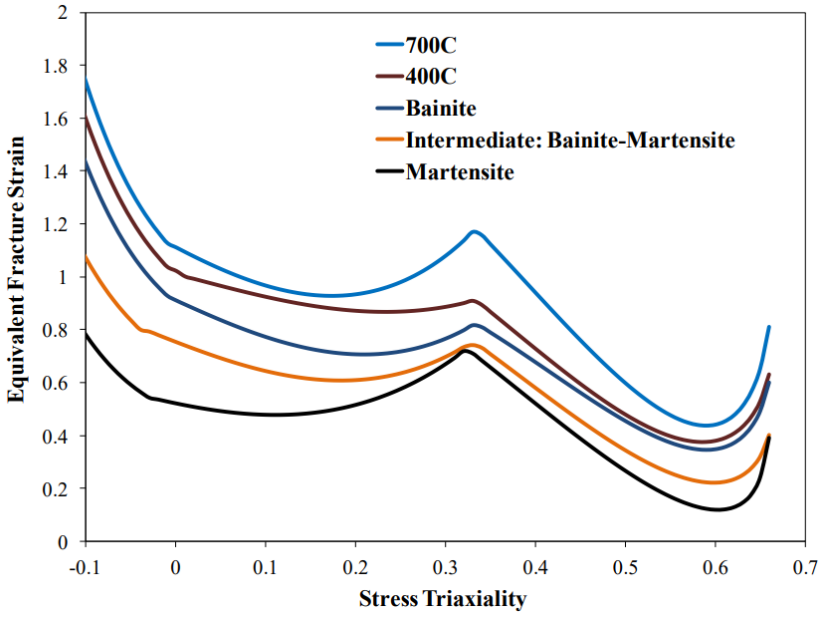

Figure 2.20: Fracture loci corresponding to different quench conditions (ten Kortenarr, 2016)

2.5.2 Testing and Numerical Modelling of Tailored Hot Stamped Usibor® 1500-AS Tubes

Using the aforementioned characterization and constitutive modelling methodologies, Omer *et al.* (2017) modeled the THS process to produce numerical models of hat sections with a fully martensitic microstructure as well as an axially tailored model (called three zone) with graded distribution of Vickers hardness (Figure 2.21).

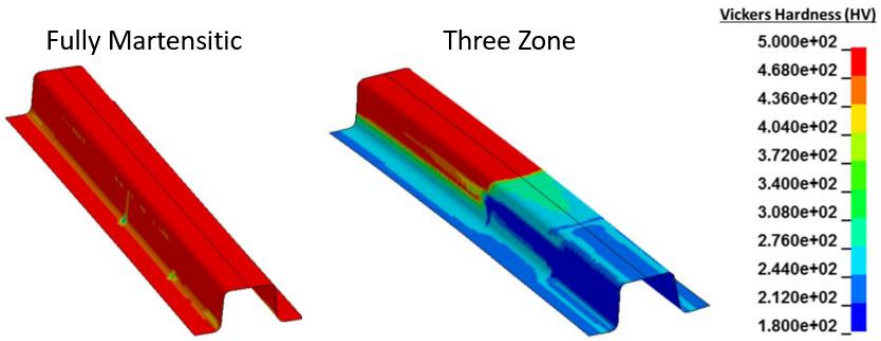

Figure 2.21: Vickers hardness distribution for each condition as predicted by the forming model developed by Omer (2014)

The final output of the THS model from the cooling stage was then fed into a remapping program developed by George (2011). The program read in the properties of each element from the final model, then outputted a hat section model with the elements sorted into five bins based on its Vickers hardness value (Omer *et al.*, 2017). The material model of each bin was determined by its weighted average Vickers hardness, in which flow stress curves at various strain rates were generated based on the Voce hardening model by Bardelcik *et al.* (2012) and applied to all the elements within each bin. The final binned fully martensitic hat section is shown in Figure 2.22, and the final binned three zone hat section with examples of flow stress curves is shown in Figure 2.23. Omer *et al.* (2017) implemented these flow stress curves into a piecewise linear plasticity material model in LS-DYNA (*MAT_024) with a von Mises yield criterion in his investigation of forming, impact testing, and numerical modelling of tailored axial crush members, which is of particular interest to the current work due to its relevance.

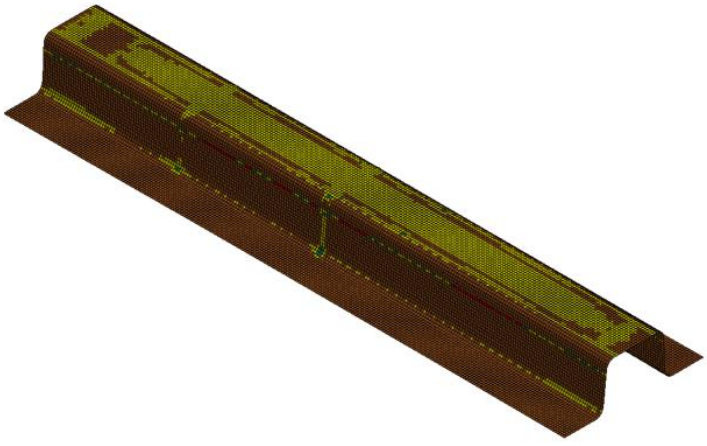

Bin Number	Vickers Hardness Range (Weighted Average)
1	456 – 462 (459.4)
2	463 – 468 (465.5)
3	469 – 474 (471.6)
4	475 – 480 (477.6)
5	481 – 487 (483.7)

Figure 2.22: Fully martensitic hat section model and bin distribution by Omer *et al.* (2017)

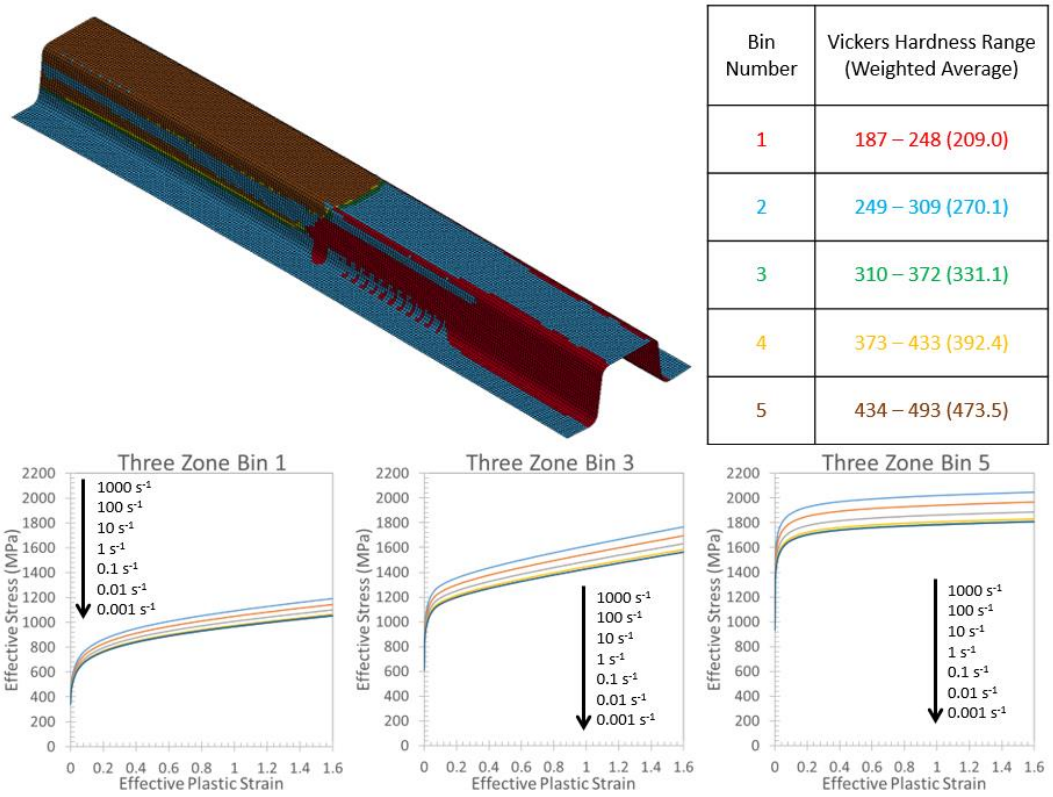

Figure 2.23: Three zone hat section model and bin distribution by Omer *et al.* (2017), including flow stress curves for various material bins

Using a similar approach, Prajogo (2015) investigated the effect of tailoring the flange of a hat section, spot welded to a full or split backing plate, on its impact response in a three-point bend test. Prajogo (2015) demonstrated that by softening the flanges of hat sections through IDH, the extent of fracture observed in the part could be reduced. Using the same forming and material modelling approach as Omer *et al.* (2017), Prajogo (2015) developed impact simulations that correlated well with the experiments, using the tailored flange hat section model (called soft flange) shown in Figure 2.24. However, in the context of loading an adhesive joint in a bonded structure in shear (Mode II) for the purpose of the current work, the backing plate specimen geometry was not ideal since it did not position the joint at the neutral axis.

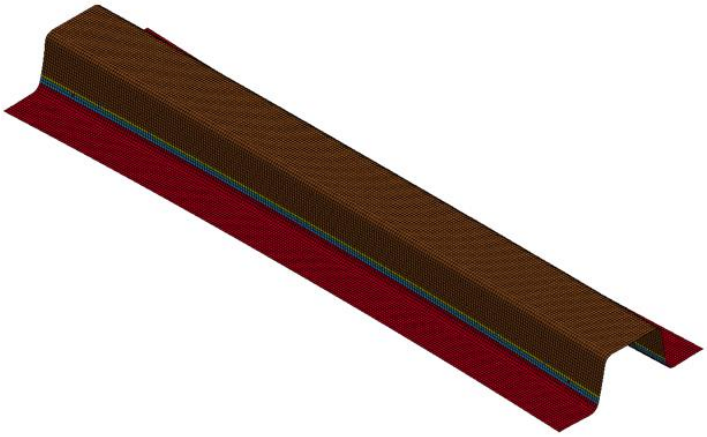

Bin Number	Weighted Average Vickers Hardness Range
1	254.1
2	301.4
3	358.3
4	424.2
5	486.2

Figure 2.24: Soft flange hat section model and bin distribution by Prajogo (2015)

O'Keeffe (2018) developed a novel Mode I opening test called the "Caiman" and used it to characterize weld group failure in partially spot welded Usibor® 1500-AS double-hat section tubes (Figure 2.25). The crosshead displacement loads the spot weld joints in tension (Figure 2.26), causing a crack to form and propagate progressively due to weld failure. In addition to a dynamic mixed-mode loading scenario provided by an axial crush test, the Caiman could be an effective test in providing a controlled and highly repeatable structural testing data for model validation, particularly for investigation of predicting adhesive joint crack propagation.

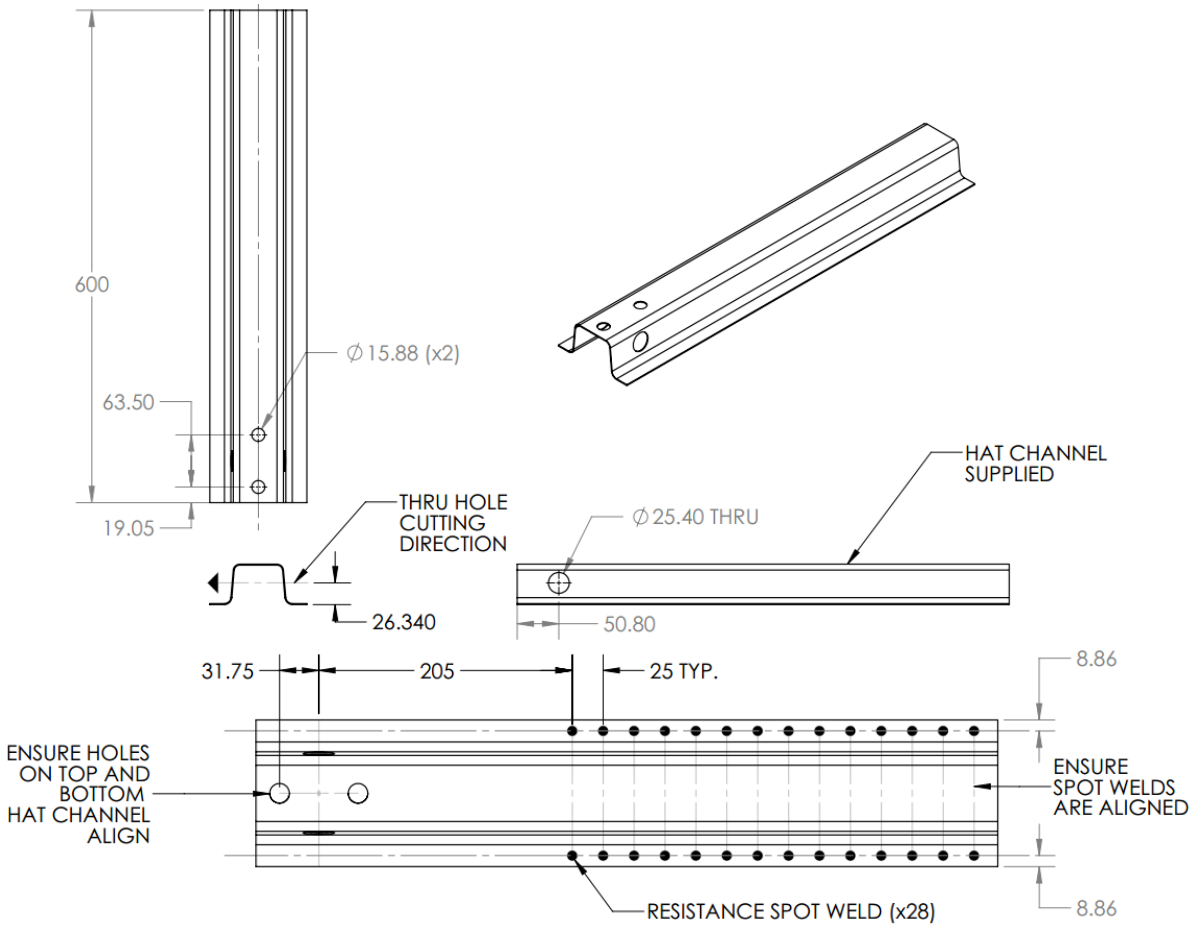

Figure 2.25: Fabrication drawings for Caiman specimens (O'Keeffe, 2018)

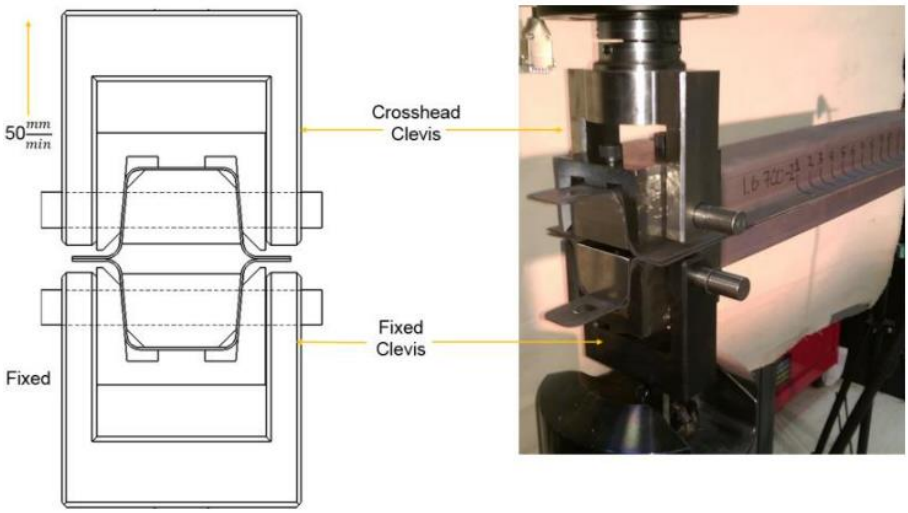

Figure 2.26: Schematic and fixturing of the Caiman test (O'Keeffe, 2018)

While a wealth of studies has investigated THS experimentally and numerically, the method of joining and assembling the components was primarily spot welding. With the rapid emergence of adhesive joining as a promising candidate in achieve multi-material lightweight vehicles, it is important to investigate the effect of tailoring the base metal on the impact response of adhesively joined structures. Furthermore, it is critical to develop and validate a robust adhesive model capable of accurately predicting the joint behavior and failure in complex loading scenarios at the structural level.

Chapter 3 Experimental Testing of Bonded UHSS Tubes

3.1 Overview of Experimental Programme

The focus of this work was to assess the adhesive model, previously developed by Watson *et al.* (2018) based on testing of adhesive material and coupon-level adhesive joints, at the structural level. In the current study, the structure-level assessment was performed by measuring the mechanical response of adhesively joined double-hat section tubes and comparing them against numerical model predictions. A key objective of this thesis was to quantitatively evaluate the accuracy of the numerical model in predicting the impact behavior of adhesively joined structures, subjected to different modes of loading, tailoring configurations, and loading rates.

To achieve this objective, a combination of three different modes of loading (Figure 3.1), three tailoring configurations (of the metal adherend) (Figure 3.2), and two loading rates (quasi-static and dynamic, or QS and DM) were conducted on adhesively joined hat sections made of Usibor® 1500-AS UHSS (Table 3.1).

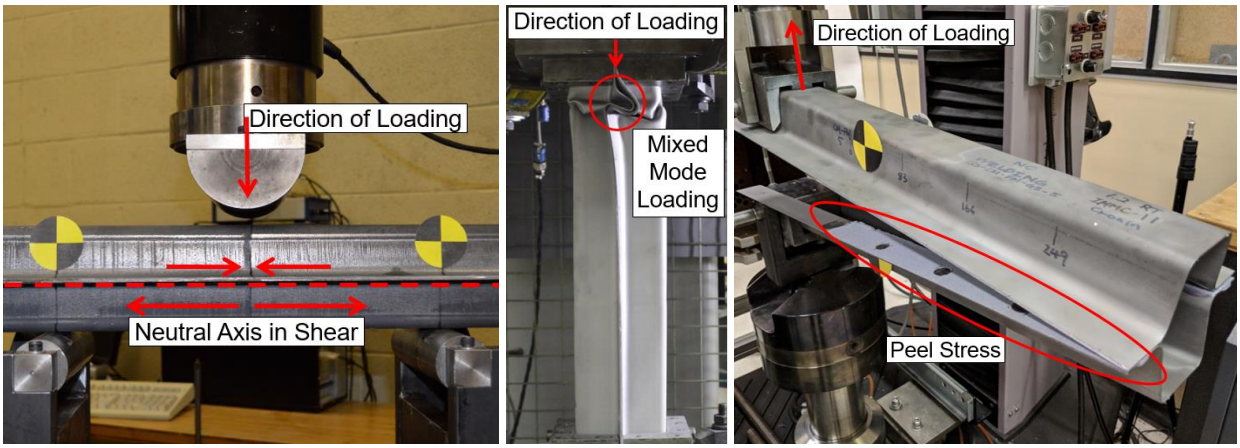

Figure 3.1: Modes of loading induced by the experiments, namely Mode II in three-point bend (left), mixed-mode in axial crush (centre), and Mode I in Caiman (right)

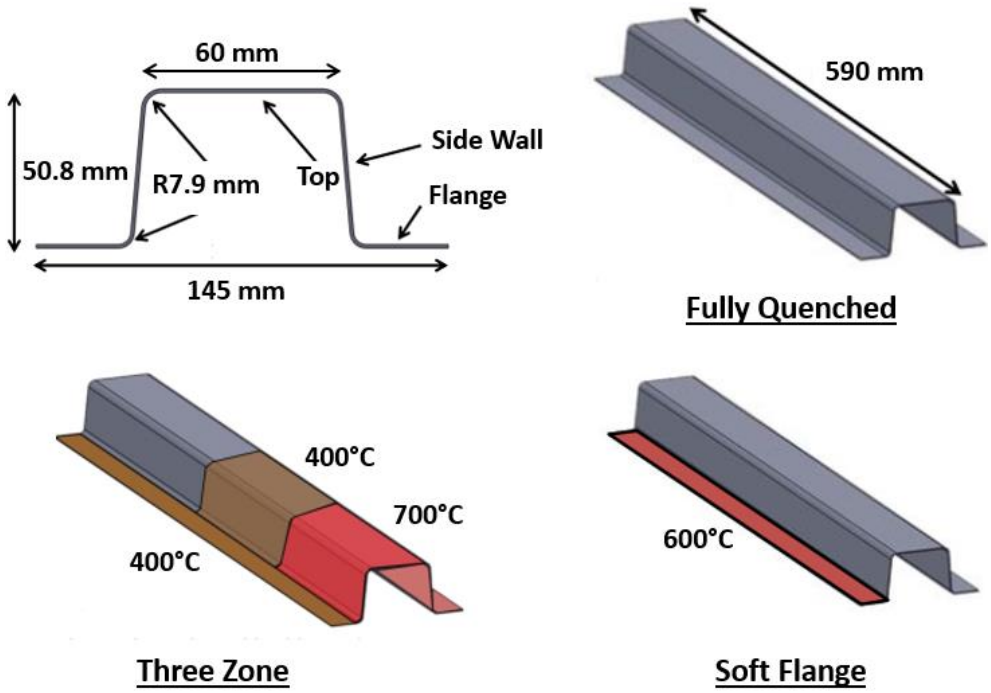

Figure 3.2: Nominal geometry of hat sections and tailoring configuration (Omer, 2014; Prajogo, 2015)

The specimen geometry involved two hat sections adhesively joined together at the flanges to form a tube (Figure 3.2). Although the hat sections were formed according to the procedure outlined by Omer (2014), Prajogo (2015) and O'Keeffe (2018), the blanks used to form the hat sections in this study were 20 mm wider. This change was made to increase the total flange surface area for adhesive bonding. While the majority of specimens were grit blasted (GB) prior to bonding to maximize joint strength, two test conditions used as-formed (AF) (no surface preparation) specimens to evaluate the effect of surface preparation on the loading response. Three-point bend (3P), axial crush (AX), and Caiman (CM) tests were conducted to measure the loading response of the adhesively joined specimens in shear (Mode II), mixed loading (Modes I and II), and tension (Mode I opening), respectively (Figure 3.2). The tailoring configurations

were achieved during forming of the hat sections through tailored hot stamping. A detailed description of the forming tooling can be found in section 3.2, and the forming process of the hat sections is described in section 3.3. The nominal cross section dimensions of the formed hat sections and a visualization of all the tailoring configurations are shown in Figure 3.3. The tailoring configurations included: (i) fully martensitic (non-tailored) (FM) specimens that were fabricated using full quenching of the hat section; (ii) so-called "soft flange" (SF) specimens in which the die sections adjacent to the flanges were heated to 600°C; and, (iii) so-called "three zone" (3Z) specimens in which the tooling surfaces contacting the flanges and the middle of the C-channel were heated to 400°C and the end of the C-channel first impacted by the sled were heated to 700°C.

Table 3.1: Structural component test matrix. Note that "FM" (fully martensitic) refers to a fully quenched, non-Tailored condition.

Surface Preparation	Test Mode	Tailoring Configuration	Loading Rate	Test Designation	Test Repeats
Grit Blast	3 Point Bend	Fully Martensitic	Quasi-static	QS-3P-FM-GB	3
Grit Blast	3 Point Bend	Fully Martensitic	Dynamic	DM-3P-FM-GB	3
Grit Blast	3 Point Bend	Soft Flange	Quasi-static	QS-3P-SF-GB	3
Grit Blast	3 Point Bend	Soft Flange	Dynamic	DM-3P-FM-GB	3
Grit Blast	Axial Crush	Fully Martensitic	Quasi-static	QS-AX-FM-GB	3
Grit Blast	Axial Crush	Fully Martensitic	Dynamic	DM-AX-FM-GB	3
Grit Blast	Axial Crush	3 Zone	Quasi-static	QS-AX-3Z-GB	3
Grit Blast	Axial Crush	3 Zone	Dynamic	DM-AX-3Z-GB	3
Grit Blast	Caiman	Fully Martensitic	Quasi-static	QS-CM-FM-GB	3
Grit Blast	Caiman	Soft Flange	Quasi-static	QS-CM-SF-GB	3
As-formed	3 Point Bend	Fully Martensitic	Quasi-static	QS-3P-FM-AF	3
As-formed	Axial Crush	3 Zone	Quasi-static	QS-AX-3Z-AF	3

The goal of tailoring the hat sections was to better allow the test samples to achieve the desired mode of loading during each of the test modes. For example, a stable collapse *via* local folding pattern involving mixed mode loading of the adhesive joint was desired in axial crush

experiments. In a similar loading scenario with spot welded tubes, Omer *et al.* (2017) reported that a three zone tailored tube had significantly more consistent deformation behavior than the fully martensitic tubes, and were the least prone to buckling. The low ductility of a martensitic microstructure may prohibit a stable collapse by encouraging a more global buckling deformation mode, causing extensive metal fracture as well as rapid debonding of the adhesive joint. On the other hand, having a gradual transition of soft to hard zone could assist in triggering a folding pattern early on, and help to maintain it throughout the experiment, allowing any cracks in the adhesive joint to propagate progressively.

After forming, the hat sections were prepped for bonding into the double-hat section test specimen tube geometry following the procedure described in Section 3.5. The tubes were then tested using the quasi-static setups described in Section 3.6 and the dynamic setups in Section 3.7. The force-displacement response was recorded from the experiments and used to validate the numerical models, along with the general deformation patterns, which will be discussed in detail in Chapters 5 and 6.

3.2 Description of Forming Tooling

Three different configurations of tooling were used to form the fully martensitic, soft flange, and three zone hat sections.

The three zone hat sections were formed using the three zone tailored in-die heating tooling (Figure 3.3) (Omer *et al.* 2017). The tooling was divided into major sections separated by an air gap of 3.2 mm: heated sections corresponding to the soft zone(s) of the formed parts, and

water-cooled sections corresponding to the hardened martensitic zone in the formed parts. A steady state temperature of 12 °C was maintained in the cooled punch and die with chilled water circulated through the tooling. The heated section was subdivided into two zones separated by an air gap of 2 mm that allowed the soft zone to be graded due to independently controlled temperature zones. Heat was provided by 3/4" diameter cartridge heaters supplying 550 W at 600 V, and the temperature in the heated section was held constant using PID controllers.

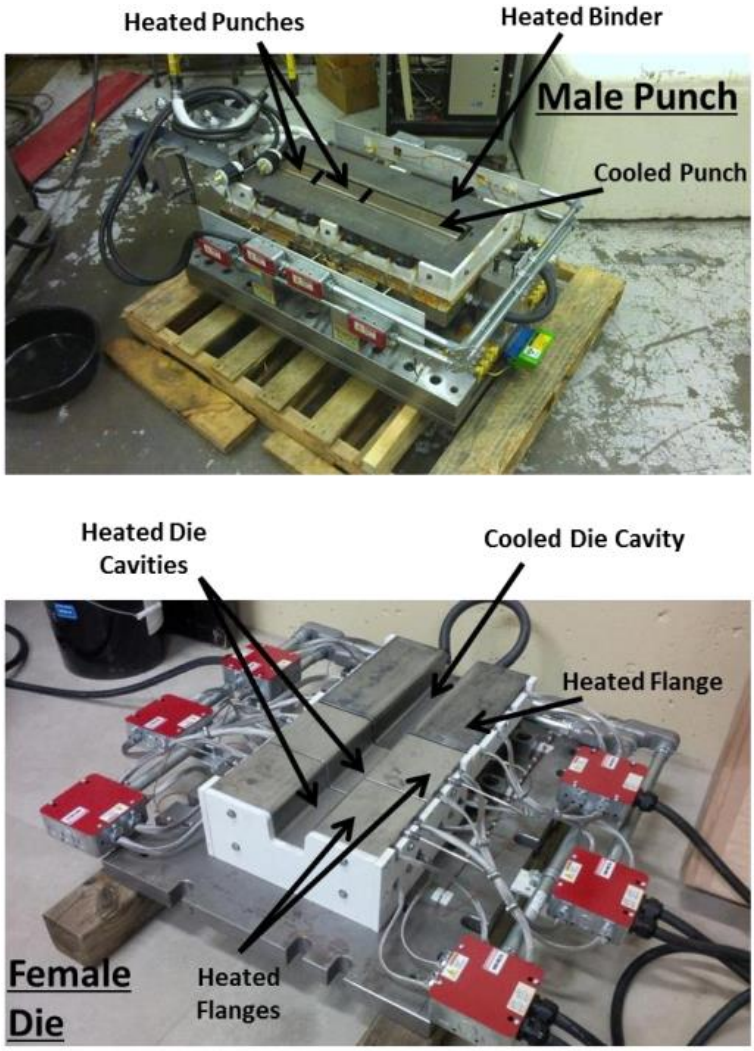

Figure 3.3: Male punch and the corresponding female die used to form the three zone hat sections, detailing the heated and cooled regions (Omer, 2014)

To account for differences in expansion of tooling due to different temperature targets, the cooled punch and die were designed to allow for easy insertion of shims. As illustrated in Figure 3.4 and 3.5, the cooled punch and die were attached to the bottom and top plates using four screws that were on the “visible” side when the tooling was in the press. Furthermore, four cutouts were present in the cooled punch block where levers could be inserted to lift the punch, allowing the insertion of shims. However, while both the heated and cooled punch/die were leveled with one another at room temperature, two ridges were created between different heating control zones of the tooling. Feeler gauges were used to measure the height of the ridges, which were found to be 0.016” in the die and 0.006” in the punch for the 400 °C zone, an 0.023” in the die and 0.026” in the punch for the 700°C zone. Due to a limitation on the design of mounting and wiring for the 400°C zone die and punch, they are very difficult to shim. This meant that only one ridge between different zones could be removed by either shimming the cooled die and punch to align with the 400°C or 700°C, while the other ridge will remain. Therefore, a decision was made to shim the cooled die and punch to align with the 400°C zone, leaving a ridge between the 400°C zone and the 700°C zone, as illustrated in Figure 3.6.

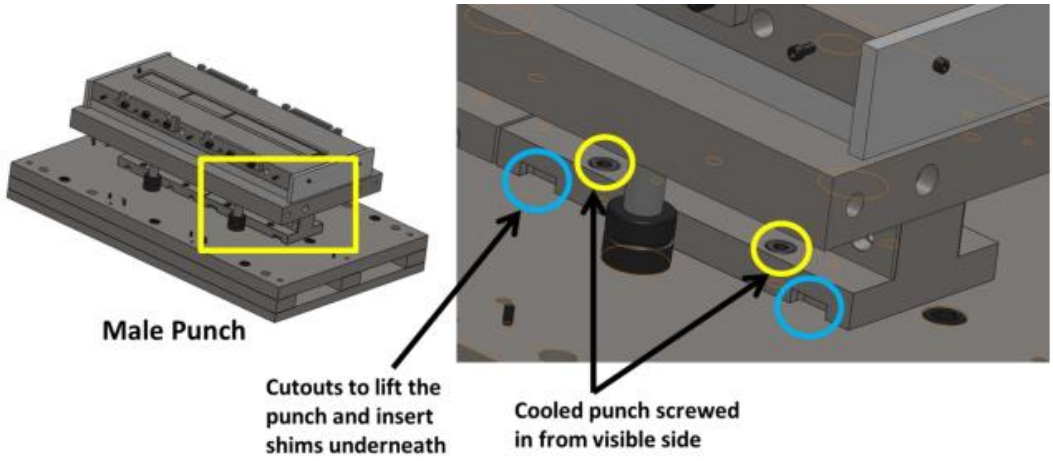

Figure 3.4: The mounting and cut-out location on the male punch used during shim insertion

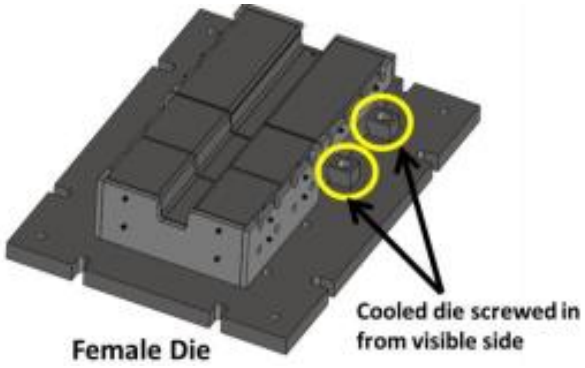

Figure 3.5: The mounting location of the female die, no cutout required since die is suspended

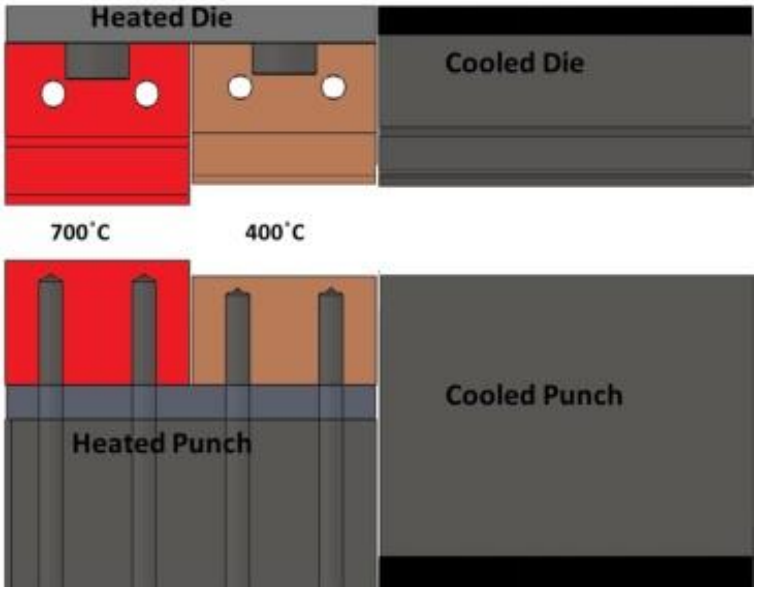

Figure 3.6: Representation of the side profile of the tooling once it is heated, showing the misalignment between the heated zones and the cooled punch aligning to the 400 °C zone

Similar to the three zone tooling, the soft flange tooling (Figure 3.7) consisted of three major components, namely the die, binder (and blank holder), and punch. Instead of dividing each major component into different heating zones to obtain lengthwise tailored hat sections, the heaters were arranged such that only the binder and blank holder were heated to 600°C and held constant with PID controllers. Chilled water was pumped through the die cavity and the punch to maintain a steady state temperature of 25°C. As seen in the schematic, an air gap of 2 mm was incorporated into the tooling to insulate the chilled region of the die from the heated

flange region. Heating was supplied with 16 (8 on each side) 700W cartridge heaters at 600V in both the blank holder and the binder. The heaters in the blank holder were 76.2 mm long while the ones in the binder were 101.6 mm long. The heating circuit was setup such that there were 4 control zones in the top and bottom halves of the tooling. Similar to the three zone die tooling, 12.7 mm thick panels of ZIRCAL-95 were used to insulate the heated parts of the soft flange tooling.

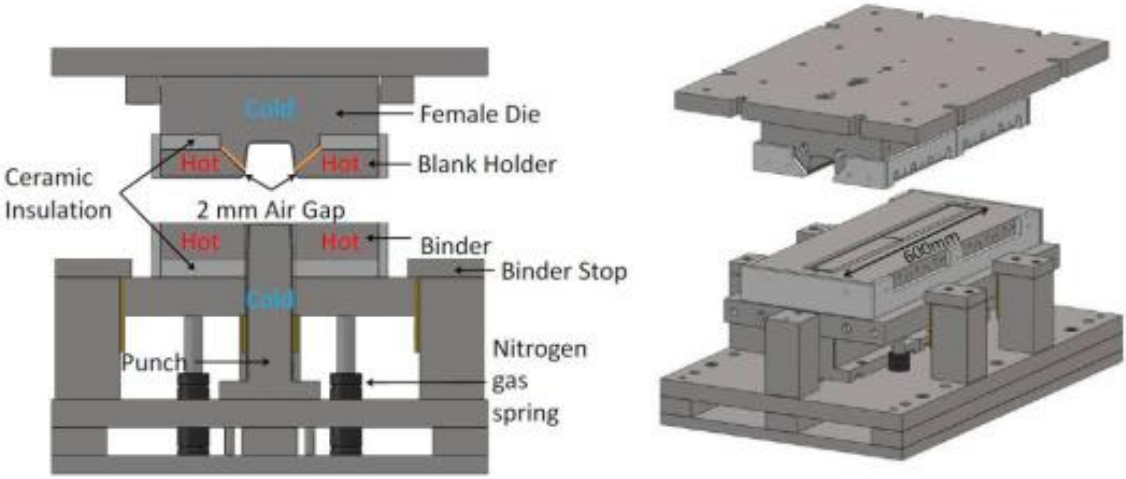

Figure 3.7: Schematic of the tooling used to form soft flange hat sections, where the entire punch and die are water cooled, while binder and blank holder are heated

3.3 THS Process Parameters for Forming Hat Sections

The hat sections used in this work were formed from blanks of Usibor® 1500 AS measuring 220 mm x 590 mm (Figure 3.8). The blanks were water jet cut, and two tabs were incorporated on either end for alignment during the forming process. The longer tab contained an oval slot, while the other shorter tab contained a triangular slot, both of which fit onto designated pins incorporated in the forming tooling. In addition, the tabs act as a gripping point when the transfer mechanism moves the blank from the furnace to the tooling, while also making it much

easier to remove the formed hat section from the female die at the completion of the forming process.

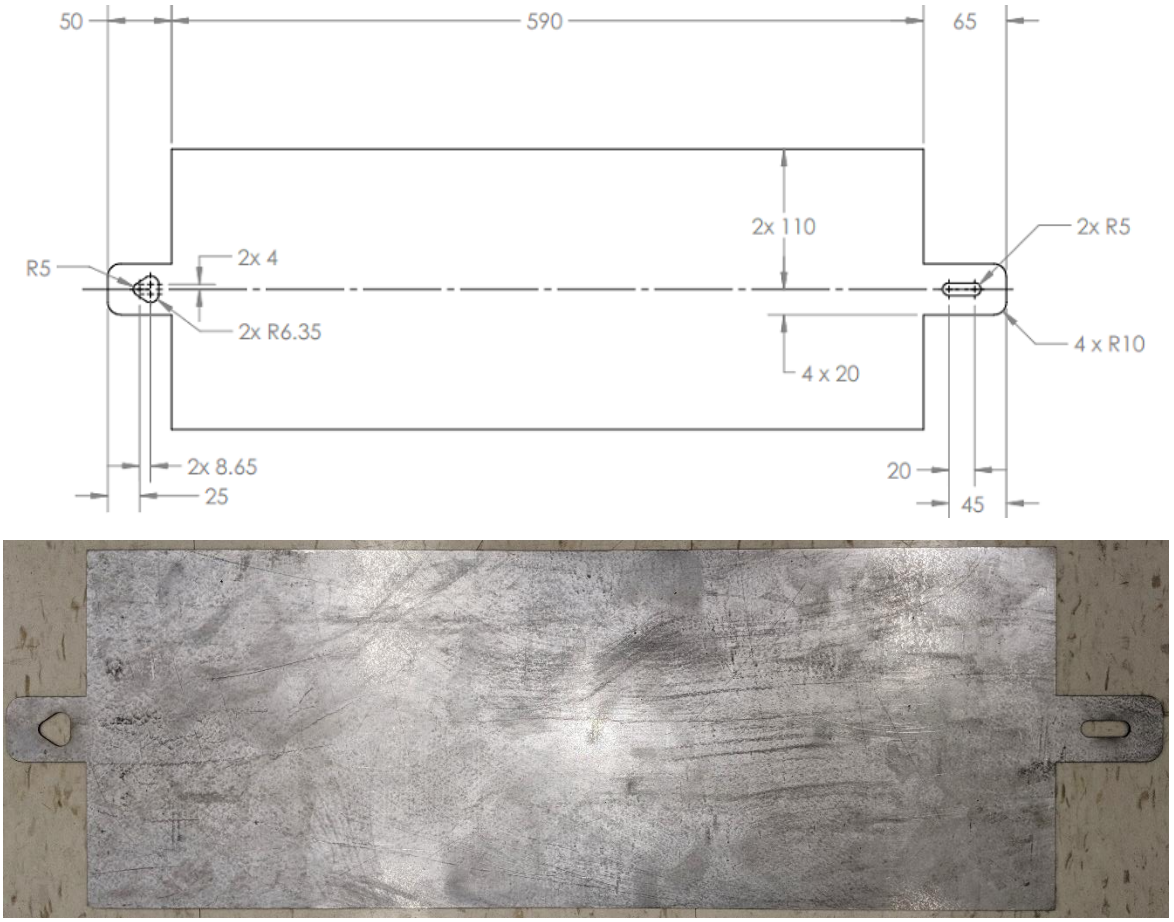

Figure 3.8: Dimensions and photograph of the blank used for all experiments

The THS process used to create the hat sections was performed on a hydraulic forming press manufactured by Macrodyne Technologies Inc. (Figure 3.9). The press contained a 900-ton main cylindrical actuator, as well as four other small cylinders, called kickers, which were capable of generating 60 tons of force at a higher speed. Only the kickers were required to apply the forming tonnage for all forming cycles.

The THS process was divided into five stages: austenization, transfer, forming, quenching, and cooling. The blanks were first autstenized using a furnace, manufactured by Deltech Inc, located

adjacent to the press. To ensure the blanks were evenly heated throughout, the oven contained three control zones, one at the front, one in the middle, and one at the back. Located in front of the press was an automated pneumatic transfer mechanism that transferred the heated blanks from the furnace to the forming tooling, where It was formed and quenched. Grips were mounted on the transfer rail to clamp the heated blanks. To minimize heat loss of the blank to the grips during the transfer process, an insulator was used on the grip surface and the grips contacted the blanks at the very edge of the tab.

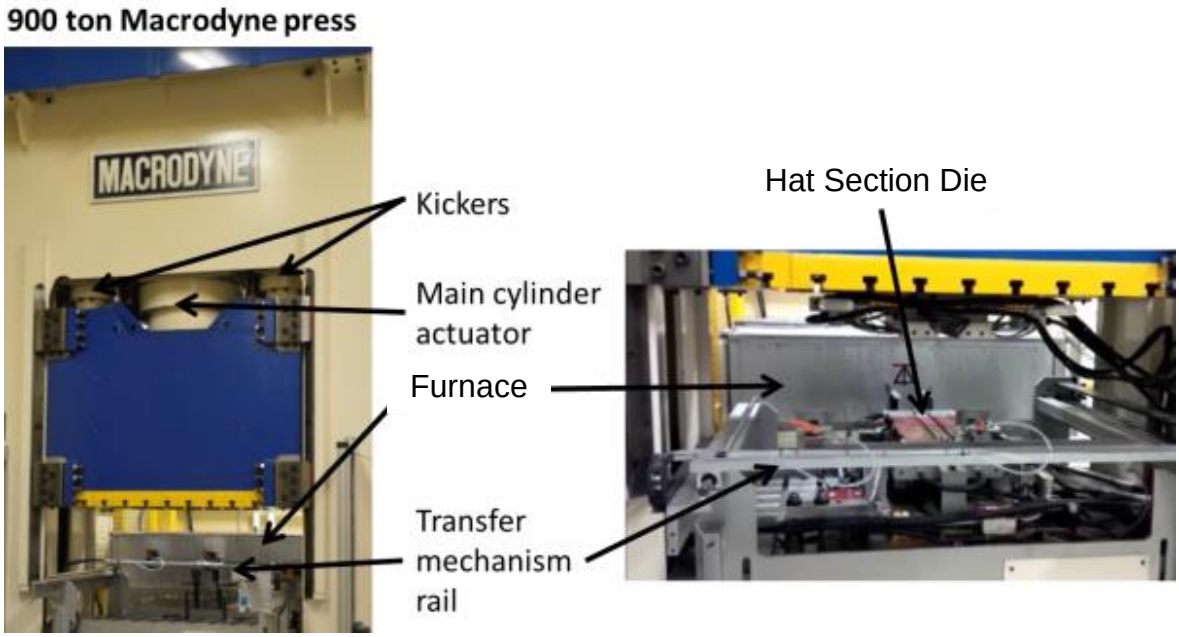

Figure 3.9: Forming setup, including components of the press, the furnance, and the transfer mechanism

The transfer mechanism positioned the blank over the punch, where the tab cut-outs were aligned with pins on the binder, after which the forming process was initiated. During forming, the male punch remained stationary while the female die descends onto the blank, forming the hat section geometry. The binder was positioned initially around the stationary punch and was

mounted on twelve nitrogen gas spring cylinders that each exerted a constant pressure of 6.895 MPa (1000 psi). With a cylinder diameter of 23mm, the resulting total force the binder exerted against the die was 34.4 kN. Once the forming cycle ended and the press was returned to the home position, the hat sections were manually removed from the press and placed on racks to be air cooled.

In summary, the specific stages of the THS process were as follows:

1) The blank was austenized in a furnace at 930°C for six minutes.
2) The blank was then transferred into the die set using the pneumatic transfer mechanism (taking approximately 10.5 s), where the tab cut-outs were aligned with the pins on the tooling.
3) The blank was then formed.
4) The formed part was quenched in the tooling for 4 s at 60 tons of force.
5) The formed hat section was removed from the female die and allowed to air cool.

3.4 Micro-Hardness Measurements on As-Formed Parts

Micro-hardness measurements were performed on as-formed hat sections. The measurements were performed on smaller sections along the length of the hat section (Figure 3.10) and were taken on the flange, side wall, and the top surface for each of the three tailoring configurations. Five sections were taken from each three zone hat sections, while only three sections were taken from each of the martensitic and soft flange hat sections, since the three zone hat sections had more distinct hardness zones along the length. Two hat sections each were

selected at random for measurement from the martensitic and soft flange conditions, while three were selected from the three zone hat sections, due to the higher complexity of the three-zone tailoring configuration. All sections were initially cut to 60 mm in length with an abrasive saw. Figure 3.11 shows an example of a three zone hat section prior to and after cutting with an adhesive saw.

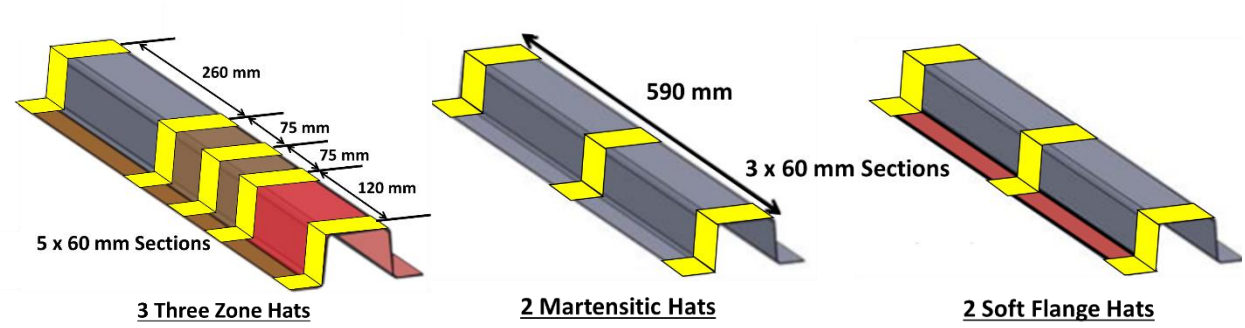

Figure 3.10: Outline of the bulk sections cut for hardness testing

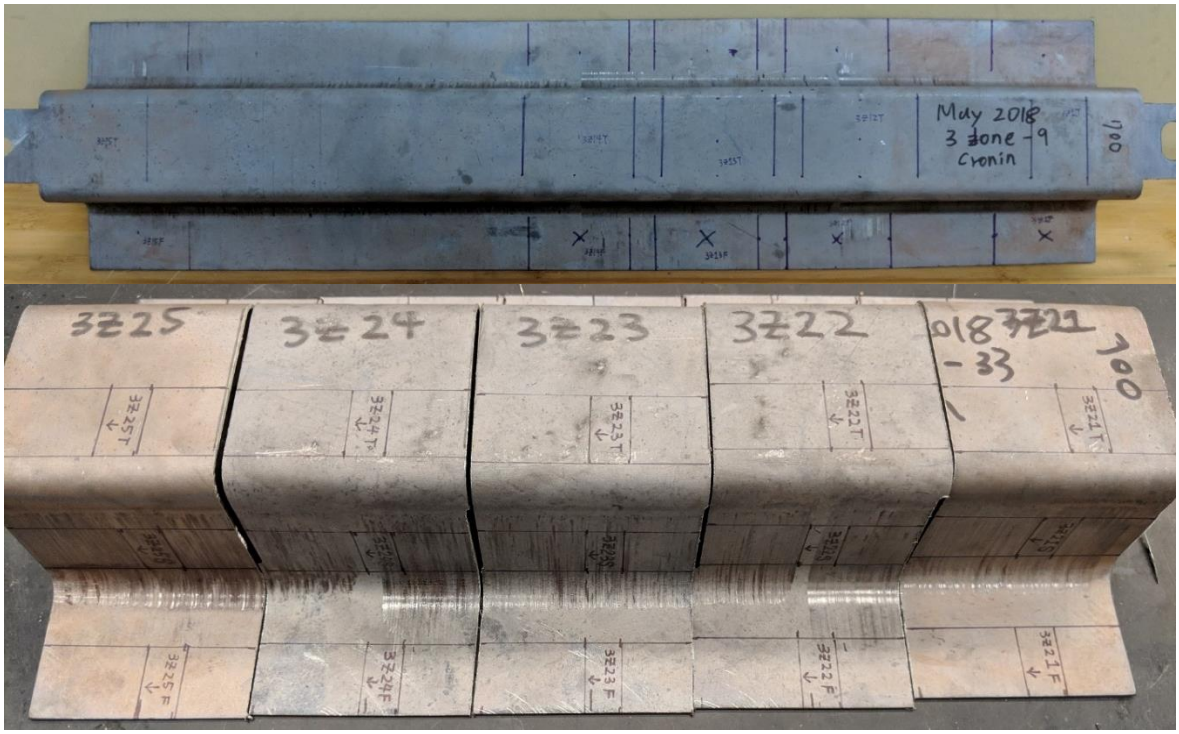

Figure 3.11: An example of three zone hat section before cutting, and the sections after cutting

A wet saw was then used to cut the bulk sections into small strips measuring 10 mm x 20 mm to be mounted in epoxy. The final strips were taken from the centre of each section, which meant that there was a buffer spacing of 30 mm between each side of the surface where hardness measurements were taken and where the abrasive saw cut was made. This spacing ensured that the area heated by the saw blade did not reach too far into the centre, and that the measured hardness was representative of the as-formed hat sections. A coolant was used with the wet saw to minimize the local temperature increase on the surface where hardness measurements will be taken. Three strips, which corresponded to one region of a hat section, were cast in a single mount, which were polished with silicon carbide (SiC) paper in the order of 320, 500, 800, 1200, 2400, and 4000 grit.

A Wilson Hardness VICKERS 402 MVD tester, was used to make the hardness measurements. A load of 1000g was used to make pyramid indents into the polished metallic surface, then a built-in microscope and measurement system was used to measure the diagonals to calculate the Vickers hardness. The Vickers hardness measurements served as a method to verify that the physical formed hat sections had the correct hardness distribution according to their tailoring configurations. The hardness data could also be used to compare the hat sections formed in this work to the hat sections formed by Omer (2014) (Figure 3.12) for axial crush testing and Prajogo (2015) for three-point bend testing. For the fully martensitic and three zone hat sections, Omer's (2014) original data on the measured Vickers hardness and the predicted hardness, based on the forming model, were obtained and plotted for a more in-depth comparison. Note that the current samples had fewer data points since the hardness measurements were only taken at key sections along the length of the hat sections, as opposed

to taken at set intervals along the entire length. Therefore, the data was presented as a linear curve fit, such that a straight line was plotted between the measured data points. Since Prajogo's (2015) original measured Vickers hardness data of the soft flange hat sections and the predicted hardness were unavailable, the standard deviation of the current soft flange data was plotted as the upper and lower bounds to indicate the spread of the measurements. The measured *vs.* predicted Vickers hardness for the soft flange hat sections as presented in Prajogo's (2015) study is shown in Figure 3.13.

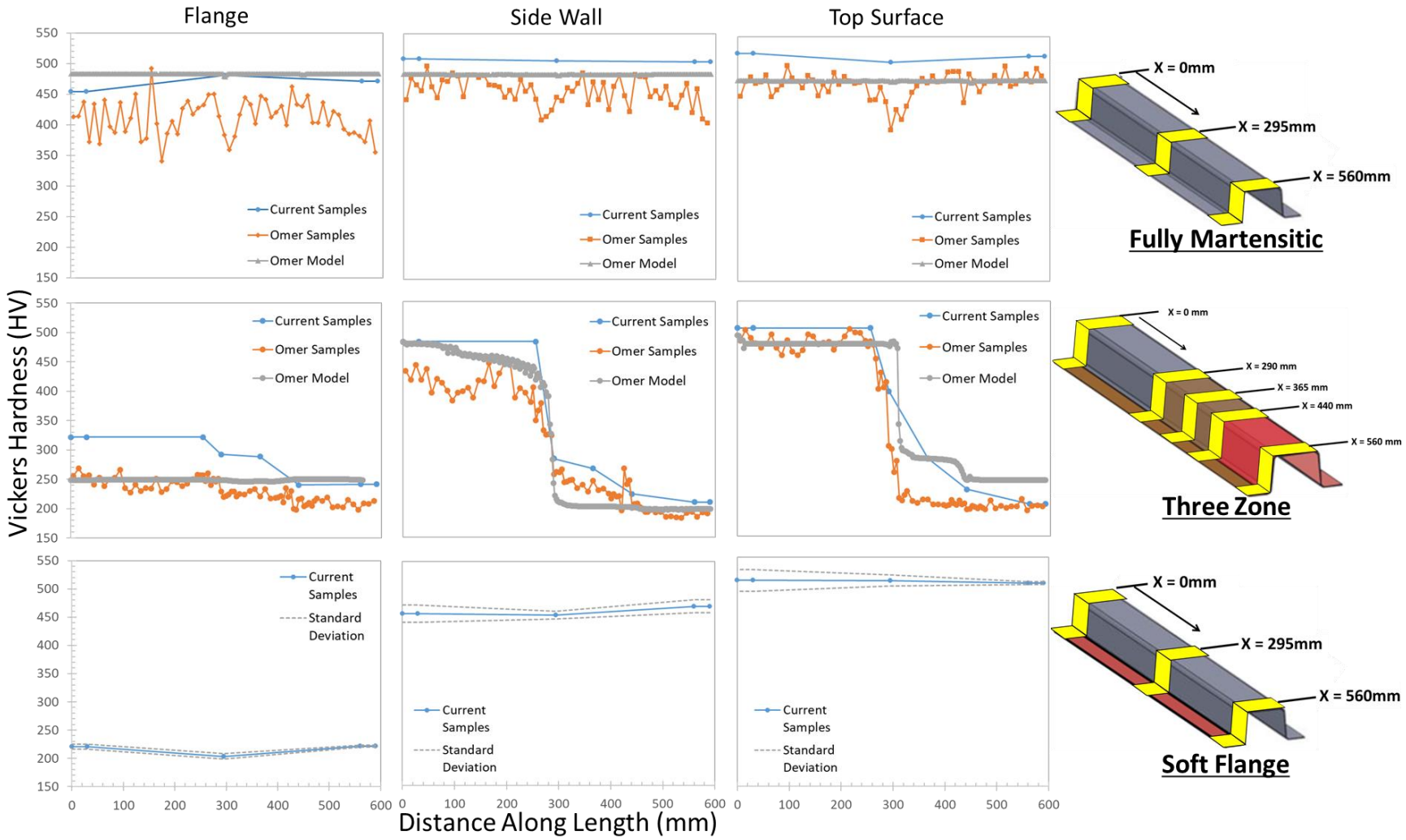

Figure 3.12: Vickers hardness measured in the current work for the flange, side wall, and top surface, plotted along the length of the hat section for all three tailoring configurations

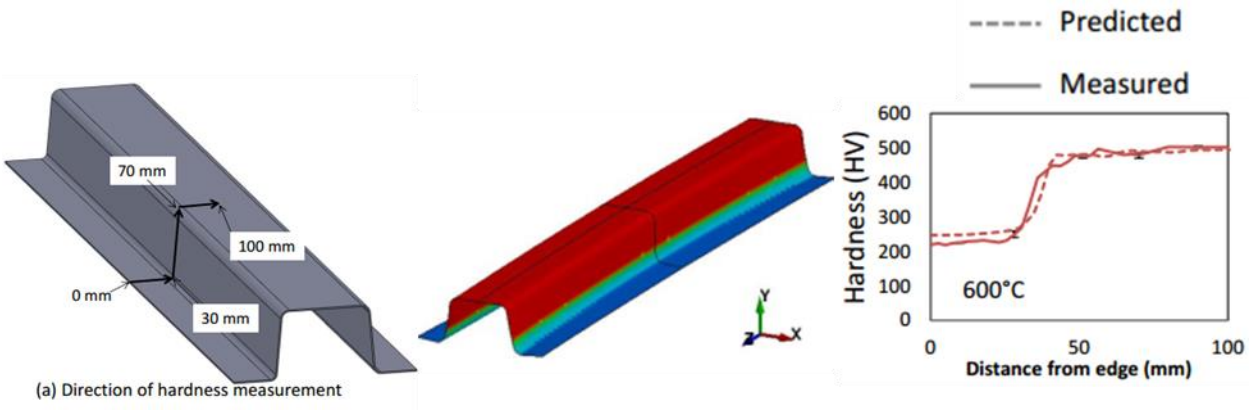

Figure 3.13: Vickers hardness measured by Prajogo (2015) for soft flange hat sections

3.5 Preparation and Bonding Procedure of Formed Parts

3.5.1 Preparation of Final Hat Section Geometry Prior to Bonding

After the hat sections were formed, samples to be tested in axial crush and Caiman had their tabs cut off, and additional machining was required to prepare the samples for testing. As-formed three-point bend samples did not require any further preparations to finalize geometry.

To control the initiation of folding in the axial crush specimens, a fold initiator (dimple) was formed 65 mm (Figure 3.14) from the top end of the hat section (the 700 °C end for three zone hat sections) at a depth of 4 mm (Omer, 2014). The dimple serves as a fold initiator to promote progressive folding during the axial crush experiments. A punch measuring 25 mm x 10 mm with a fillet radius of 5 mm on all its edges was used to form the dimple on a hydraulic hand press.

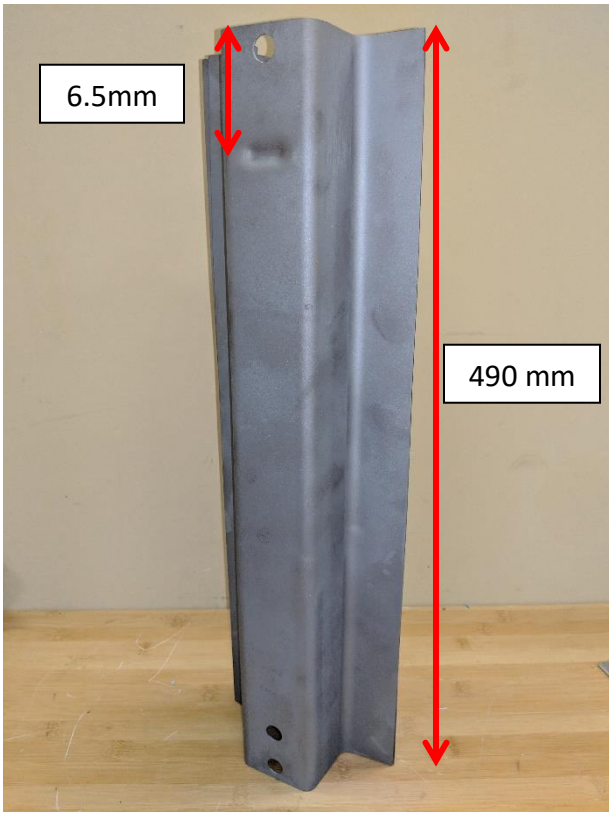

Figure 3.14: The fold initiator (dimple) on an axial crush hat section

To further minimize the likelihood of global buckling in any of the axial crush experiments, all axial crush hat sections were cut down to a length of 490 mm (Omer, 2014). The last step of preparation for axial crush hat sections prior to bonding was to drill 12.7 mm diameter holes at either end using a carbide drill bit. The holes were used to locate the tube in the axial crush fixture.

The hat sections to be tested in Caiman experiments were prepared according to O'Keeffe's (2018) drawings (Figure 2.25, Section 2.5.2).

3.5.2 Surface Preparation for Bonding

An important goal of this research was to achieve cohesive failure in the adhesive. Thus, careful preparation of the adherend surface was performed to maximize the joint strength between the adhesive and the adherend. An investigation by Liao *et al.* (2016) into surface treatment methods to maximize the strength of single lap shear experiments found that a combination of grit blasting of the adherend surface to increase roughness, followed by cleaning the surface with methyl ethyl ketone (MEK) immediately prior to application of adhesive achieved consistent cohesive failure with the highest joint strength and lowest variability. In addition to roughening the metal surface, another function of grit blasting was that it removed the Al-Si-Fe intermetallic coating that was present on the as-received Usibor® 1500-AS material, which has been shown to increase likelihood of interfacial failure (decrease joint strength and increase variability) (Liao *et al.*, 2016). It was also shown in the investigation that cleaning with acetone produced similar results to MEK, while being a safer and less expensive chemical to work with. Therefore, all hat sections were grit blasted with 60 grit aluminum oxide and then cleaned with acetone prior to bonding, with the exception of the tests that specifically used the as-formed condition to assess intermetallic coating strength (Table 3.1, Section 3.1) that were only cleaned with acetone prior to bonding.

3.5.3 Initial Bonding Procedure with Square Shims

An adhesive bond line thickness of 0.178 mm (0.007”) was used for all experimental specimens following the manufacturers recommendations, and brass shims were used to maintain the bond line thickness while the flanges were clamped down for curing. Initially, the first few tubes

that were bonded for quasi-static three-point bending were grit blasted, cleaned with MEK, and then strips of brass shims 25 mm wide were placed on each end and each side of the flanges while the adhesive was being applied (Figure 3.15). The adhesive was only applied and spread on one hat section for each tube, while the other hat section with a bare surface was placed over the first.

Figure 3.15: Bonding of an early sample, where the rectangular shims are at the ends of the flange

A preliminary fixture using five C-clamps, as determined to be optimal in ensuring uniform adhesive coverage based on a wettability study, and 0.5” thick steel bars were used to secure the flanges (Figure 3.16) while they cured in a convection oven at 80 °C for thirty minutes. The steel bars were used to evenly distribute the load applied by the C-clamps, while also closing the gaps that exist between the as-formed hat sections due to warpage after hot-stamping. Warpage was only noticeable in tailored components, in which the three zone samples form a gap between the flanges when the hat sections were placed in a double-hat configuration, measuring up to 5 mm (Figure 3.17). In addition, the side walls of the three zone samples curve inwards near the heated 700 °C end, creating a gap between the flanges when the hat sections

were placed next to one another, measuring up to 7 mm. This gap introduced considerable residual stresses (tension) in the adhesive joint and its effect will be discussed in Chapter 5. While the soft flange samples sit relatively flat against a flat surface (no bowing in flange), the side walls curve inward towards the center, then curve back out towards the other end of the hat section (Figure 3.18). This curvature produced a gap between the flanges when the hat sections were placed next to one another, measuring up to 10 mm.

Figure 3.16: C-clamps used to secure the flange prior to curing the assembly in the oven

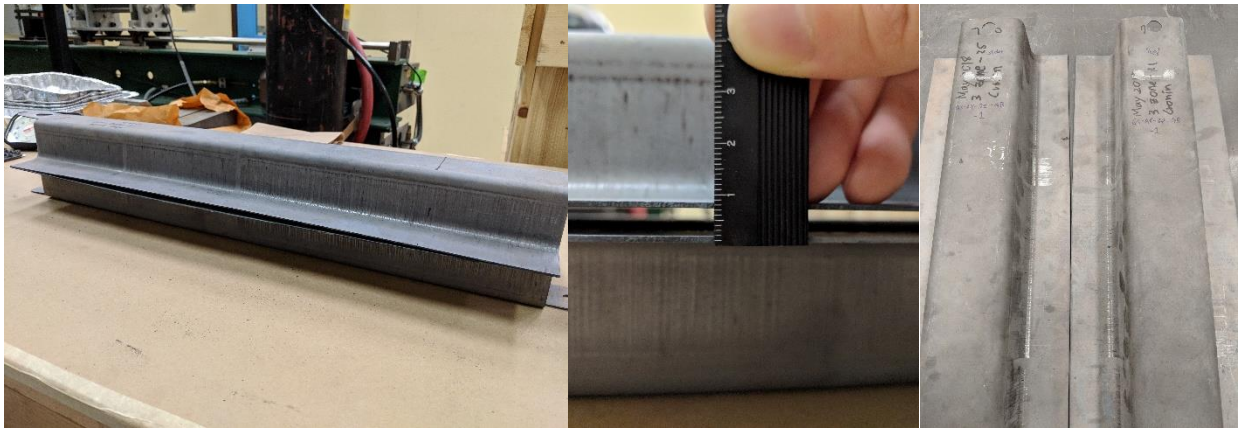

Figure 3.17: Gap between three zone flanges in a double-hat configuration (left and centre), and gap between three zone flanges when placed side by side (right)

Figure 3.18: Gap between flanges of soft flange samples when placed side by side

After the first few quasi-static experiments with tubes that were bonded with the procedure outlined above, it was observed in the failure surface that there were areas of minimal adhesive coverage along the flange. This was indicative of an excessive amount of adhesive being forced out of the bond line as the flanges were clamped down, and therefore an alternative shimming method was needed to better distribute the clamping force across the bond line. Figure 3.19 shows examples of early test results for quasi-static three-point bend and axial crush, where areas of minimal adhesive coverage were highlighted.

Figure 3.19: Failure surface of early quasi-static fully martensitic three-point bend (left) and axial crush (right), showing inconsistent adhesive coverage

3.5.4 Improved Bonding Procedure with Circular Shims

An alternative shimming method was devised using 7/16” circular shims distributed along the length of the flange, with the C-clamps aligned to the shims. This method was first tested in a numerical model comparing the loading responses of assemblies with strips of shims in each corner against those with circular shims distributed along the length. It was found that the discontinuity in the adhesive joint did not contribute to noticeable differences in the loading response. Therefore, the circular shimming method was used for all the remaining specimens, which showed a significant improvement in the quality of the adhesive joints. The revised bonding procedure began with grit blasting of hat sections, followed by adhering the circular shims to the flanges with a fast acting ethyl cyanoacrylate adhesive (Elmer’s Products Inc., 2015), and lastly cleaning the flange surfaces with acetone. Another minor change that was made to the bonding methodology was to apply adhesive to flanges of both hat sections

instead of only one. This change was made to ensure that a thin layer of adhesive was evenly distributed throughout the entire bonding surface (on both sets of flanges) prior to assembling, which added an additional layer of confidence than only relying on the clamps and steel bars to spread the adhesive. Figure 3.20 shows an example of a three-point bend specimen being bonded with the circular shim methodology.

Figure 3.20: Improved shimming technique, where circular shims are used to distribute clamping forces more evenly for uniform adhesive coverage

The exact layout of how the circular shims were distributed varied depending on the intended experimental configuration (Figure 3.21). Note that the specimen length for three-point bend and Caiman configurations were 590 mm, but only 490 mm for axial crush, as explained in Section 3.5. For three-point bending, the center of the tube lengthwise was where the majority of deformation was undergoing, and there it was thought to be best to avoid disrupting the

adhesive joint in this critical region. A region of 110 mm (5 mm wider than the diameter of the punch on each side) in the center of the adhesive joint was left undisrupted. Although the optimal number of clamps was determined to be five as previously stated, a decision was made to use six to have an even three clamps on either side of the undisrupted region, which were spaced 80 mm apart. For the axial crush specimens, a similar concept was applied in leaving the critical or more sensitive region undisrupted, which in this case would be the region around the fold initiator. The first and last (fifth) shims were located at 15 mm and 40 mm from the top (near the fold initiator end) and bottom respectively. This positioning was adopted so that the shims at the ends would be located within the clamped regions of the test specimens, as described Section 3.6. The second shim was placed 105 mm after the first (totalling 120 mm from the end of the tube closest to the fold initiator), giving the fold initiator about 50 mm of undisrupted adhesive joint on either side, then all subsequent shims were spaced 110 mm apart. Lastly, for the Caiman specimens, the adhesive joint only spanned about 334 mm (83.5 mm x 4) on the end of the tube that was not clamped into the fixture. This geometry was adopted to mimic the same lever arm length of roughly 255.8 mm used by O'Keeffe (2018). Within the 334 mm joint, three circular shims were used, spaced equally at 83.5 mm.

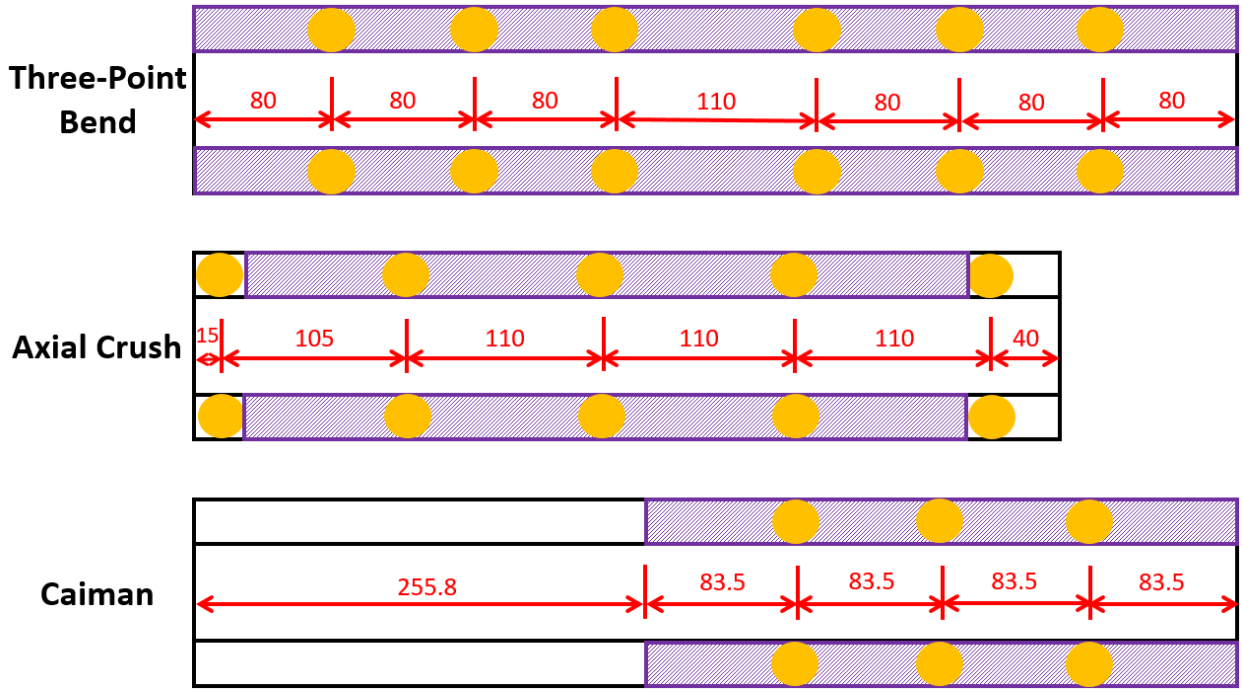

Figure 3.21: Diagram outlining the circular shim distribution for different types of experiments, all dimensions in millimeters

3.6 Experimental Setup for Quasi-Static Tests

3.6.1 Quasi-static Three-Point Bend Setup

The quasi-static three-point bend experiments were performed in a 496 kN hydraulic load frame operating under closed-loop displacement control. A crosshead velocity of 1.016 mm/s (0.04 in/s) was used for the three-point bend experiments, corresponding to a nominal strain rate of 0.01 s^{-1} for a tube height of 101.6 mm (measured from one top section to the other in double-hat cross section). A sampling rate of four points per second was used for the three-point bend experiments.

The setup for the three-point bend experiments (Figure 3.22) used an indentor of 100 mm diameter mounted to the hydraulic actuator and two cylindrical supports of 50 mm diameter

spaced 375 mm apart. Both the indentor and supports were lined with two sheets of Teflon film; in which the first sheet was taped to the metallic surface, and the second sheet rested freely on the first sheet with a thin layer of petroleum jelly-based lubricant (Vaseline) between them. The Teflon sheet and lubricant prevented contact between metallic surfaces and minimized friction during the test, which would allow relative motion between the top hat and the indentor so that the hat sections could deform freely. This setup was used for all quasi-static three-point bend experiments.

Figure 3.22: Quasi-static three point bend experimental setup

3.6.2 Quasi-static Axial Crush Setup

The first quasi-static axial crush experiments (fully martensitic grit blasted condition) were performed on the same 496 kN hydraulic load frame as all the quasi-static three-point bend experiments. The hydraulic load frame was operating under close-looped displacement control, with a sampling rate of four points per second. The crosshead velocity for the axial crush experiments was 0.508 mm/s (0.02 in/s), which corresponded to a nominal strain rate of 0.001 s^{-1} for a tube length of 490 mm.

The setup for the quasi-static axial crush experiments (Figure 3.23) included top bosses and clamps measuring 25.4 mm thick, while the bottom bosses and clamps were 50.8 mm thick, which corresponded to an effective tube length of 413.8 mm while secured in the fixture. The bottom clamps and bosses were mounted to a base plate that was clamped down and secured to the table. Shown in detail in Figure 3.24, both the top and bottom fixtures include an outer boss and sliding inner clamp for one hat section, and an inner boss and sliding outer clamp for the other hat section. For safety reasons, the entire setup was enclosed by three plexiglass panels and a steel half pipe.

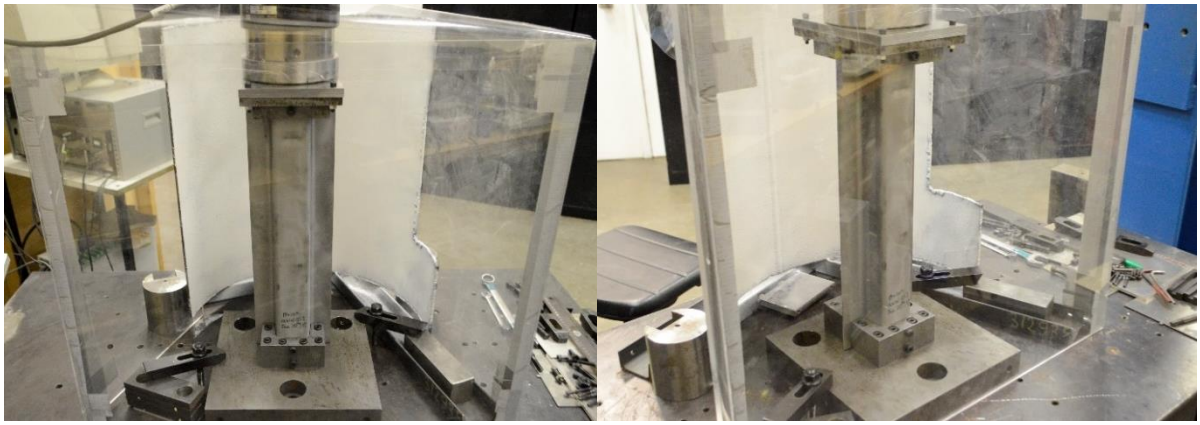

Figure 3.23: Quasi-static fully martensitic grit-blasted axial crush setup on the 496 kN hydraulic load frame

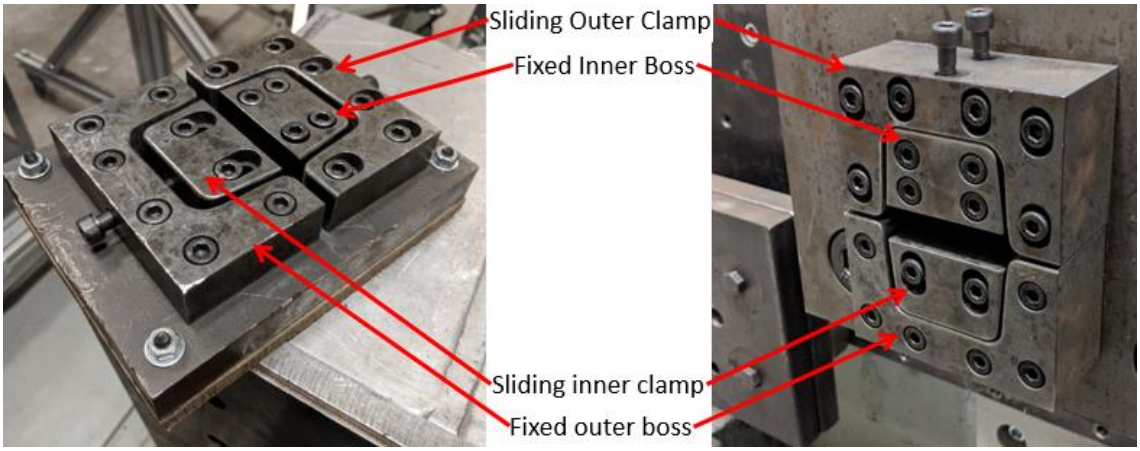

Figure 3.24: Clamps and bosses used to secure the specimens during the axial crush experiments

The sliding inner clamp was secured to the base plate with two screws, and the fixed inner boss was secured with four screws. Both the sliding outer clamp and fixed outer boss were secured to the based plate with six screws. The top outer clamp and boss each have a through-hole to allow one screw to secure the outer pieces with the inner clamp and boss, while the bottom fixtures have two through-holes on each side. All screws used for fixturing were M10 in size.

It was observed during the first axial crush experiments with grit blasted fully martensitic tubes that the hydraulic piston on the 496 kN load frame exhibited a considerable degree of lateral loading and rotation due to the deformation of the specimen. To avoid potential equipment damage and to ensure a more repeatable boundary condition at the point of load application, the balance of the axial crush experiments, namely grit blasted three zone and as formed three zone tubes, were conducted on a 623 kN, four-post hydraulic press (Figure 3.25). This press incorporated improved lateral support via four guiding posts in the corners. Note that the same mounting fixtures were used in all of the axial crush experiments to keep the boundary conditions as similar as possible.

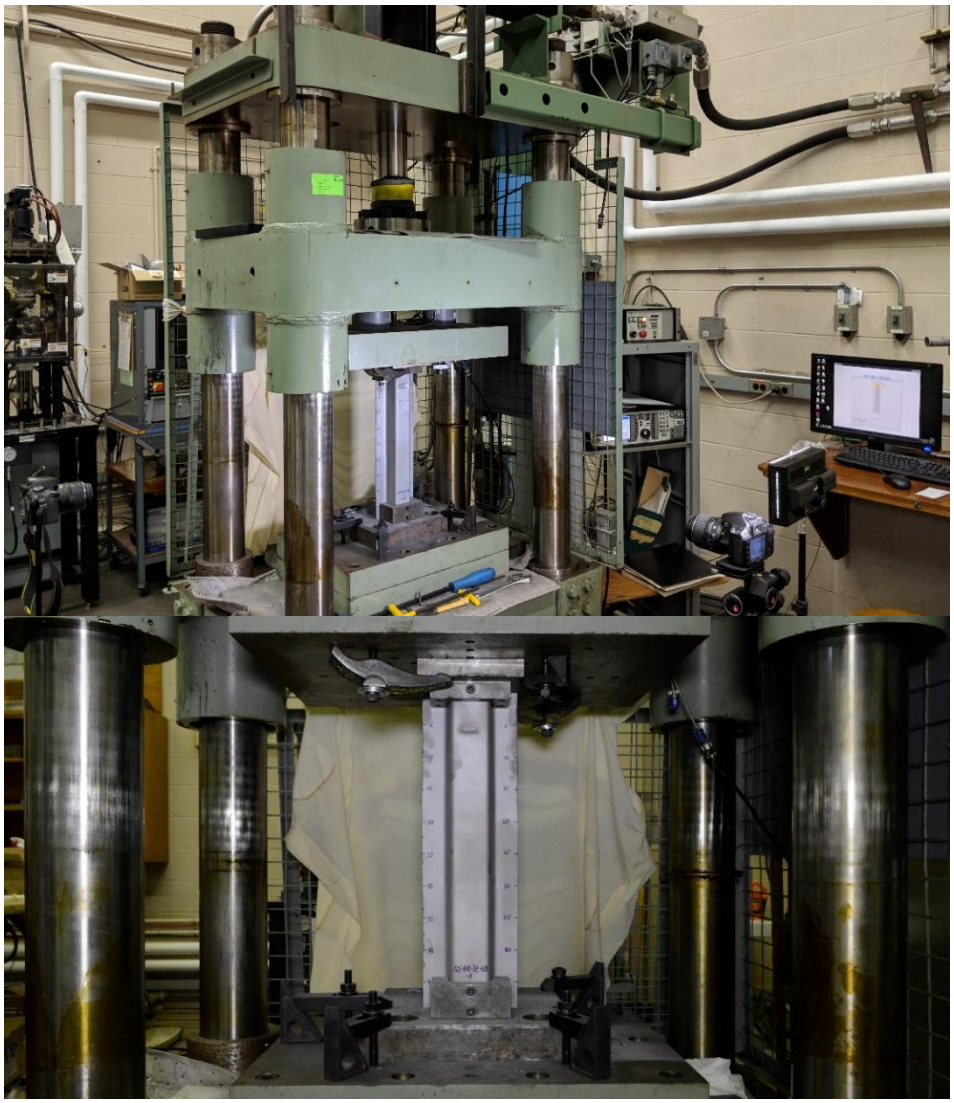

Figure 3.25: Quasi-static axial crush experiment setup on the 623 kN four-post hydraulic load frame

3.6.3 Quasi-static Caiman Setup

The setup for the quasi-static Caiman experiments is shown in Figure 3.26. The specimens were tested using in an MTS Criterion Model 45 tensile frame, with a 100 kN load cell. The adhesive Caiman specimens were mounted into the test frame to be pulled apart, inducing a progressive splitting of the joint due to Mode I failure of the adhesive. Following the investigation by

O’Keeffe (2018), Figure 3.27 shows the fixtures and boundary conditions in detail. The tooling consisted of inner and outer bosses that clamped each half of the tube with two screws, while the clevises displaced the inner bosses via the dashed 19.05 mm diameter pins. The top crosshead clevis was threaded into the load cell while the bottom fixed clevis was clamped by the knurled grips on the MTS frame. Two cameras, one on each side, were used to continuously capture images of the deformation, which were synchronized to the force and displacement data via VIC SNAP 2009.

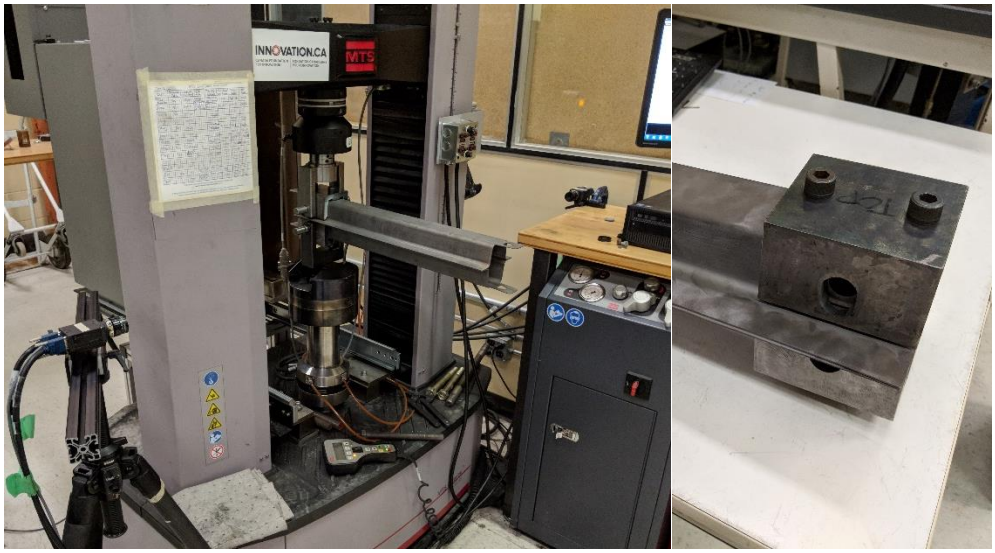

Figure 3.26: Quasi-static Caiman setup on the MTS frame (left) and the fixtures (right)

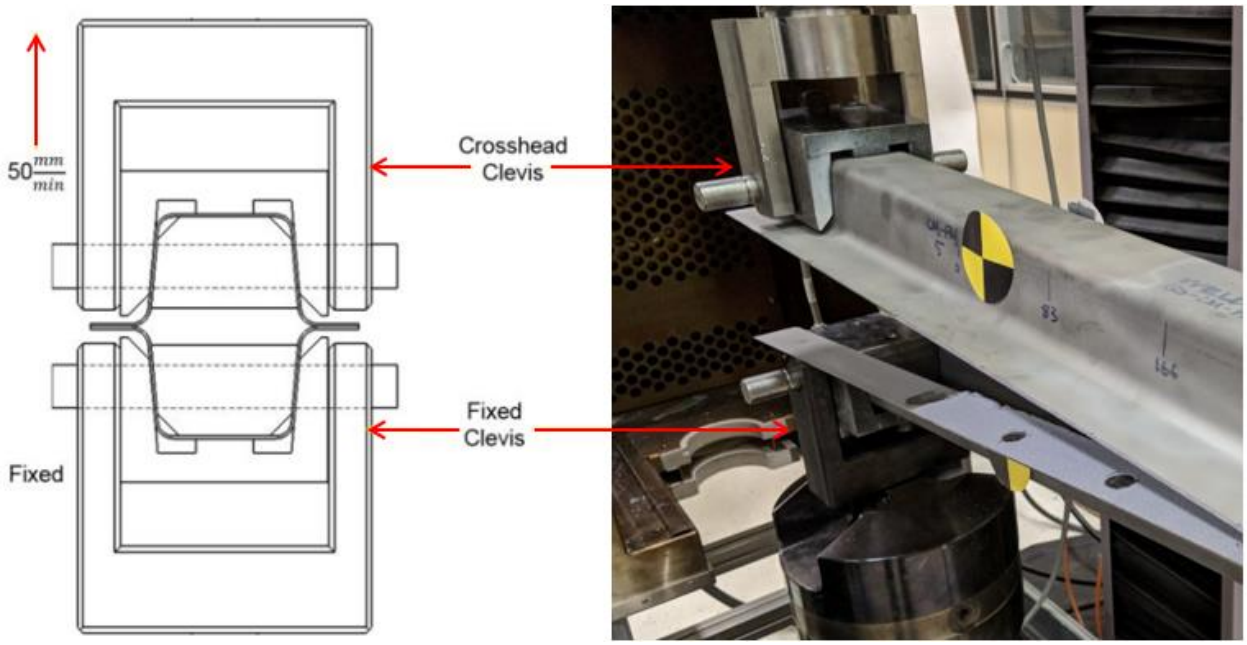

Figure 3.27: Detailed cross section of a specimen secured in the fixture (O'keefe, 2018) (left) and an adhesive Caiman test in progress (right)

An upward displacement rate of 50 mm/min was used for all quasi-static Caiman tests, resulting in Mode I loading on the adhesive joint (Figure 3.28). It was observed during the experiments that there was initially a rapid propagation of adhesive failure along the length of the specimen, which slowed significantly as the failure front propagated towards the end of the bond line. The experiments ran for approximately 105 s for a total crosshead displacement of 87.5 mm, which was sufficient to capture most of the bond line failure.

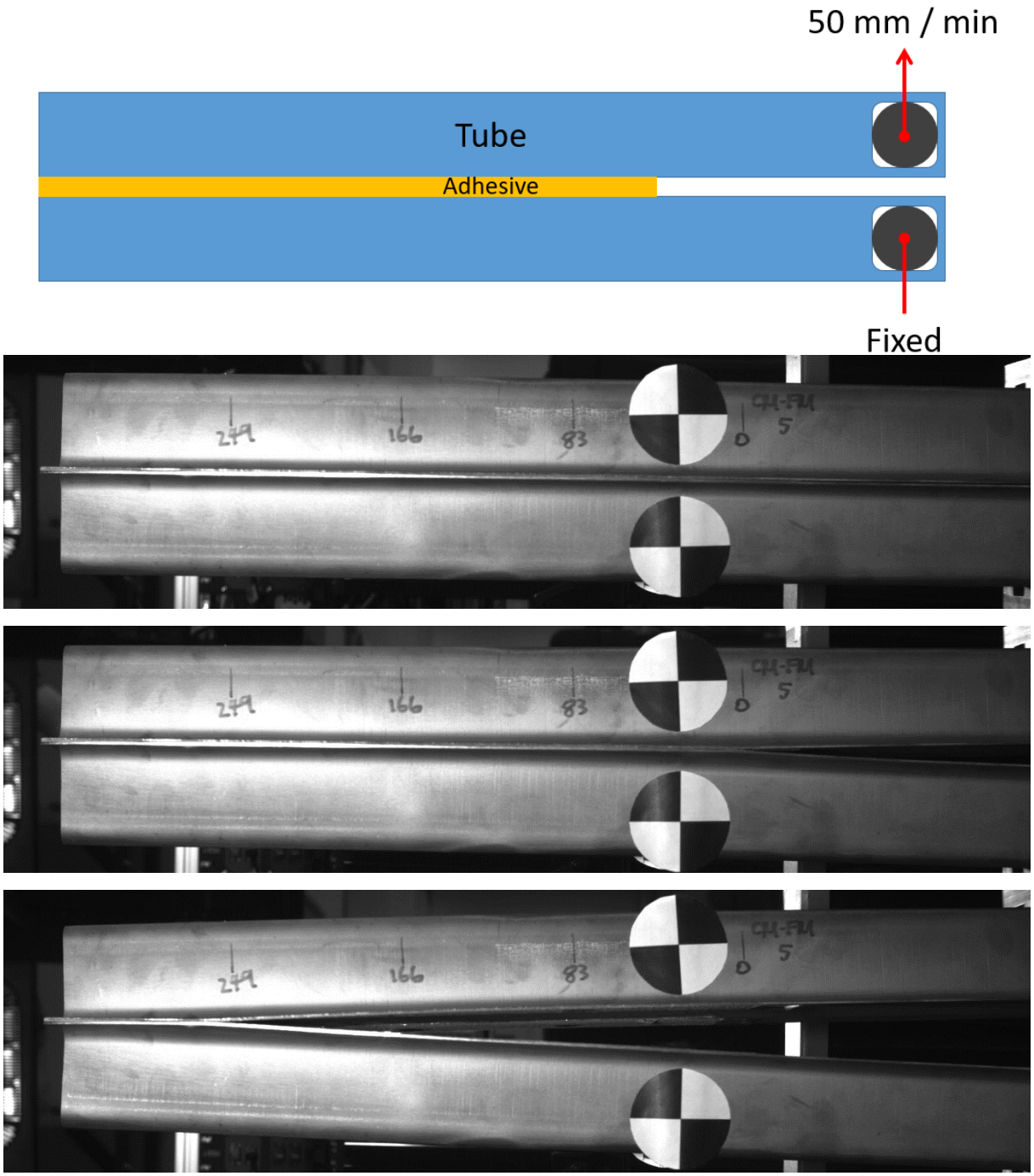

Figure 3.28: Start of Caiman test (top), onset of crack propagation (middle), crack propagation slowing and stabilizing (bottom)

3.7 Experimental Setup for Dynamic Impact Tests

3.7.1 Dynamic Three-Point Bend Setup

The dynamic three-point bend experiments were conducted using an impact sled manufactured by Seattle Safety. The same fixtures used in the quasi-static experiments were used for dynamic experiments as well. The two supports were mounted vertically on the crash wall and the indentor was mounted to the load cells attached to the impact sled (Figure 3.29). An adaptor plate was used to mount the indentor to a load cell pack comprising two 120 kN Kistler Quartz Force Link (model#9371B) load cells. A 19.05 mm thick wooden plate was added between the indentor and the adaptor plate to act as a damper, reducing noise in the loading data. The total mass of the sled was 870 kg (855 kg base sled and 15 kg total from indentor and load cells) and an impact velocity of 7.5 m/s (27 km/h) was used for all three-point bend dynamic experiments.

Two Plascore 5052 honeycomb packs with a crush strength of 3.69 MPa (535 psi) measuring 150 mm by 150 mm with a length of 200 mm each were mounted side by side beneath the three-point bend test specimen to rapidly decelerate and stop the sled after a specified free crush length. The free crush (Figure 3.30), as defined by the distance starting when the indentor first makes contact with the part to when the sled contacts the honeycomb to be quickly stopped, was roughly 55 mm.

Load cells and accelerometers were used to measure force during the dynamic experiments. Two 120 kN capacity piezoelectric load cells were mounted on the sled behind the indentor to measure the force exerted onto the specimen, whereby the total force applied was equal to the sum of forces measured by each individual cell. The load cell data was acquired with a sampling

rate of 10,000 points per second. Two accelerometers, with a sampling rate of 10,000 points per second, were mounted on the back of the impact sled, one on each side. The deceleration experienced by the sled during impact was measured and displacement was calculated by double-integrating the deceleration data obtained from the accelerometers. No software filtering was applied to the final data.

Figure 3.29: Dynamic three-point bend experimental setup, showing the mounted specimen, honeycomb packs, and cameras

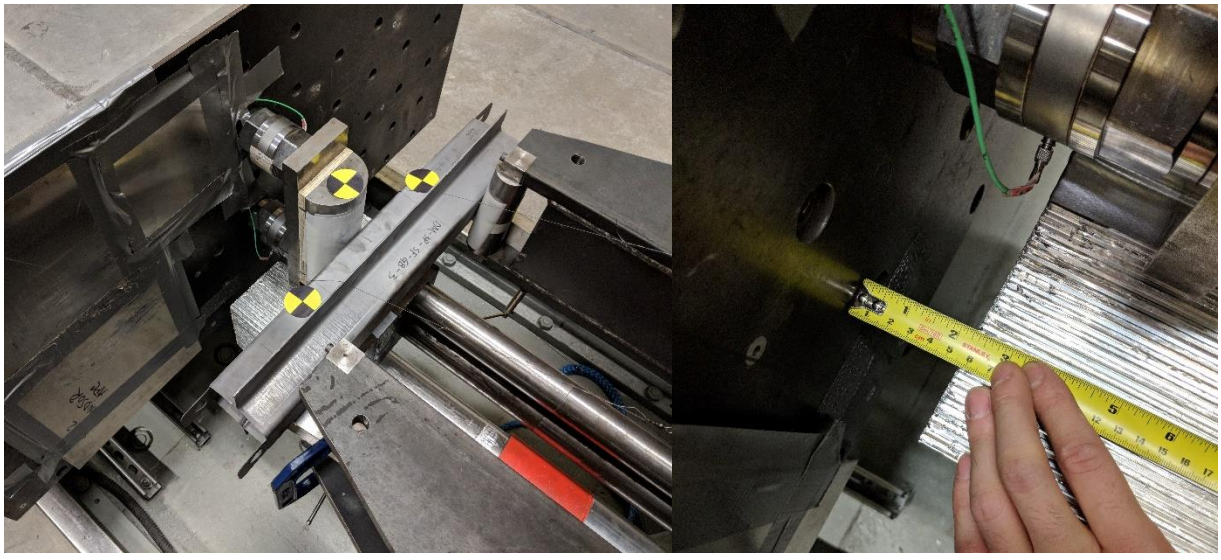

Figure 3.30: Sled and impactor brought in contact with the specimen to demonstrate distance of free crush zone

Two high-speed Photron SA4/5 digital cameras were used to record the impact experiments with a frame rate of 5000 frames per second. One camera was mounted above the specimen while the other was mounted on the side. The piezoelectric load cells and accelerometer data acquisition systems were in sync with the high-speed cameras and were activated by a laser trigger located on the rails of the sled (Figure 3.31). As the sled traveled past the trigger during a dynamic impact test, the cameras and data acquisition systems were turned on for two seconds, which was sufficient to capture the impact event.

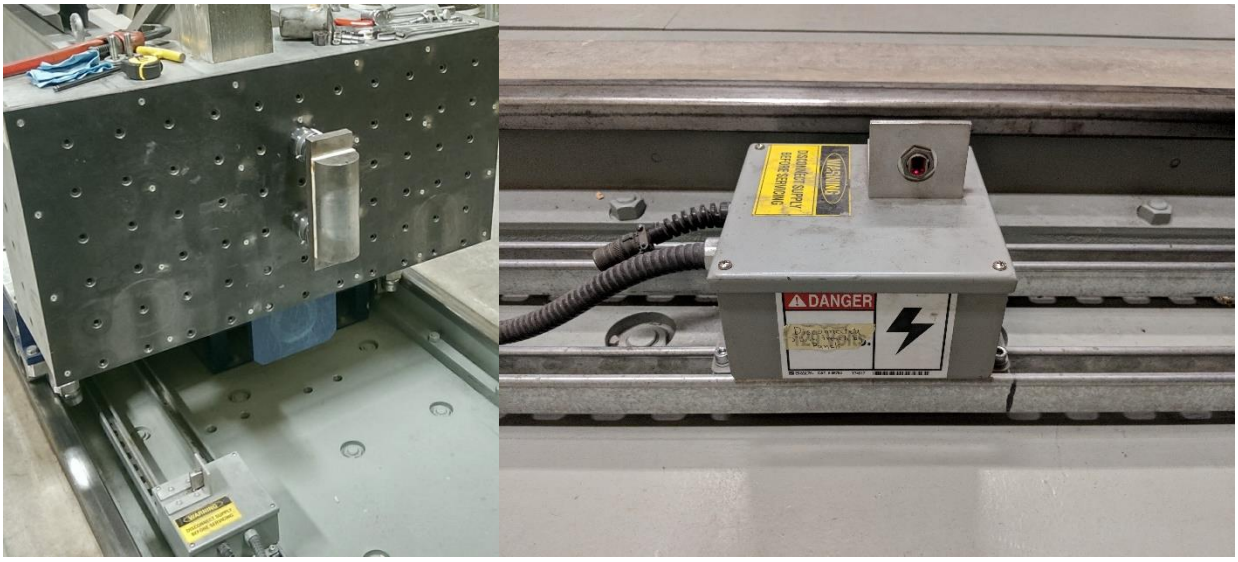

Figure 3.31: Impact sled with impactor mounted on two load cells (left) and laser trigger along the rail (right)

For the dynamic three-point bend of fully martensitic tubes, two 12.5 mm wooden inserts were placed within the tube, aligned with the location of the two support fixtures. The goal of the inserts was primarily to prevent an asymmetric deformation mode from occurring. However, it was observed that one of the fully martensitic tests still exhibited asymmetric deformation, and

therefore the inserts were not used for any other three-point bend tests, quasi-static or dynamic. While this made it difficult to compare the loading response of the fully martensitic specimens to the soft flange ones, the wooden inserts were included in the fully martensitic dynamic three-point bend model to accurately represent the boundary conditions so that the model validation case was on comparable terms.

3.7.2 Dynamic Axial Crush Setup

The dynamic axial crush experiments were conducted on the same impact sled as the dynamic three-point bend (Figure 3.32). The same fixtures used in the quasi-static axial crush experiments are used for the dynamic experiments as well, where the 63.5 mm thick base plate was mounted onto three Kistler Quartz Force Link (model #9371B) 120 kN capacity piezoelectric load cells that are mounted to the wall in a triangular pattern. The load cells measured the force, at a sampling rate of 10,000 points per second, exerted by the sled onto the specimen whereby the total force is the sum of the individual forces measured by each load cell. No software filtering was applied to the final data.

A 19.05 mm thick wooden plate is mounted to the top fixture (the end further away from the wall) to act as a damper when the sled contacts the specimen, reducing noise in the acquired force and acceleration data. This wooden plate was confined within the cutout of another 19.05 mm thick wooden board that was mounted at the center of the sled when the sled came into contact with the specimen. This was done to minimize lateral movement of the specimen

during the dynamic impact experiment. The total mass of the sled was 900 kg (855 kg of base sled plus 45 kg of standoff plates) and an initial velocity of 10 m/s was used.

Plascore 5052 honeycomb packs were used for the dynamic axial crush experiments, in which two packs of honeycomb were mounted on the wall; one on each side of the specimen. Each stack contained two blocks of honeycomb, measuring 140 mm x 140 mm and 160 mm x 160 mm with a length of 200 mm, configured in a pyramid pattern where the larger block is near the wall and the smaller block is stacked against it. The size difference ensures that the blocks engage with (dig in to) one another during impact, as opposed to buckling against each other.

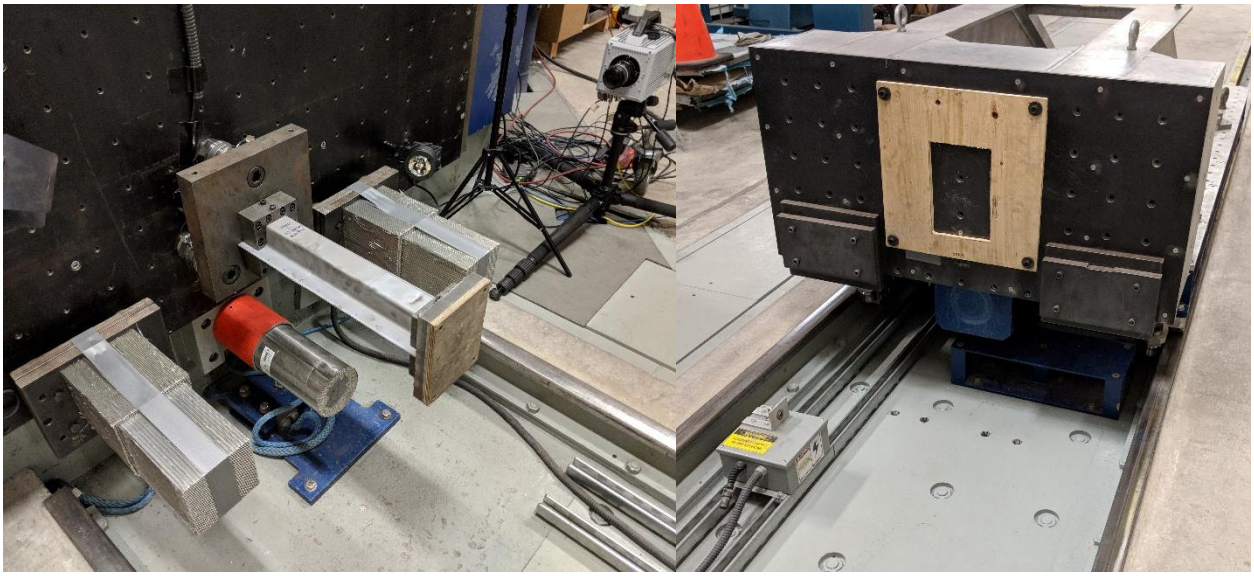

Figure 3.32: Dynamic axial crush experiment setup, showing the mounted specimen, honeycomb stack, the wooden plate and standoff steel plates on the sled

One end of each honeycomb pack was mounted against a standoff from the wall while a stack of two steel spacer plates was mounted on each side of the sled to contact the other end of the honeycomb packs (Figure 3.33). The standoffs and spacers were used to achieve a free crush

distance of about 145 mm, which was the distance starting when the sled first contacted the specimen to when the sled contacted the honeycomb packs.

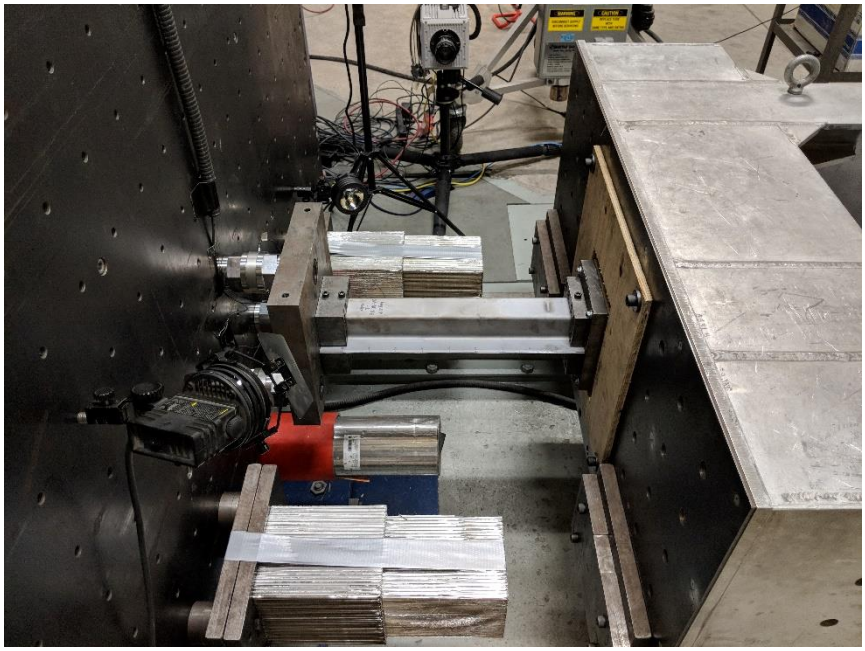

Figure 3.33: The sled brought into contact with the mounted specimen, to demonstrate distance of free crush zone

The dynamic axial crush experiments used the same camera setup (two high-speed cameras at 5000 frames per second, one on top the other on the side) and the same data acquisition systems (load cells and accelerometers onboard the sled) as the dynamic three-point bend experiments.

Chapter 4 Numerical Modelling of Impact Experiments

4.1 Double-Hat Section Tube Models

The hat section finite element models used in this work were extended from the hat section models developed by Omer *et al.* (2017), Prajogo (2015), and O'Keeffe (2018). As mentioned in Section 3.1, the blanks used to form the hat sections in this thesis were similar to previous studies, but were 20 mm wider in order to produce parts with wider flanges to increase the adhesive bond area. To address this change, the flanges of the previous hat section finite element models were extended by approximately 10 mm on each side (4 rows of elements). This extension significantly simplified the process to make the models readily usable, and was considered acceptable since the elements along the length-wise edges of the flanges for all three hat section models were in the same material bin.

For all simulations, the tubes were modeled with fully integrated shell elements (Type 16 in LS-DYNA) of 2.5 mm element size, and seven points of integration through thickness. A piecewise linear plasticity material model in LS-DYNA (*MAT_024) with a von Mises yield criterion was used for each bin of Usibor® 1500-AS, with flow stress curves at various strain rates obtained from Omer *et al.* (2017) and Prajogo (2015).

For the martensitic axial crush models, both quasi-static and dynamic, a Generalized Incremental Stress-Strain Model (GISSMO) was applied to predict the considerable amounts of steel failure observed during the experiments. This fracture model defines damage as a function of equivalent plastic strain, plastic strain at failure as defined by a fracture locus, and a user defined exponent. The fracture locus (Figure 4.1) used in this thesis was obtained from

experiments conducted by Ten Kortenaar (2016) and modified with V-Bend test data from Abedini (Tummers *et al.*, 2018). No fracture model was assigned to any other tube models since those specimens did not exhibit significant cracking in their experiments.

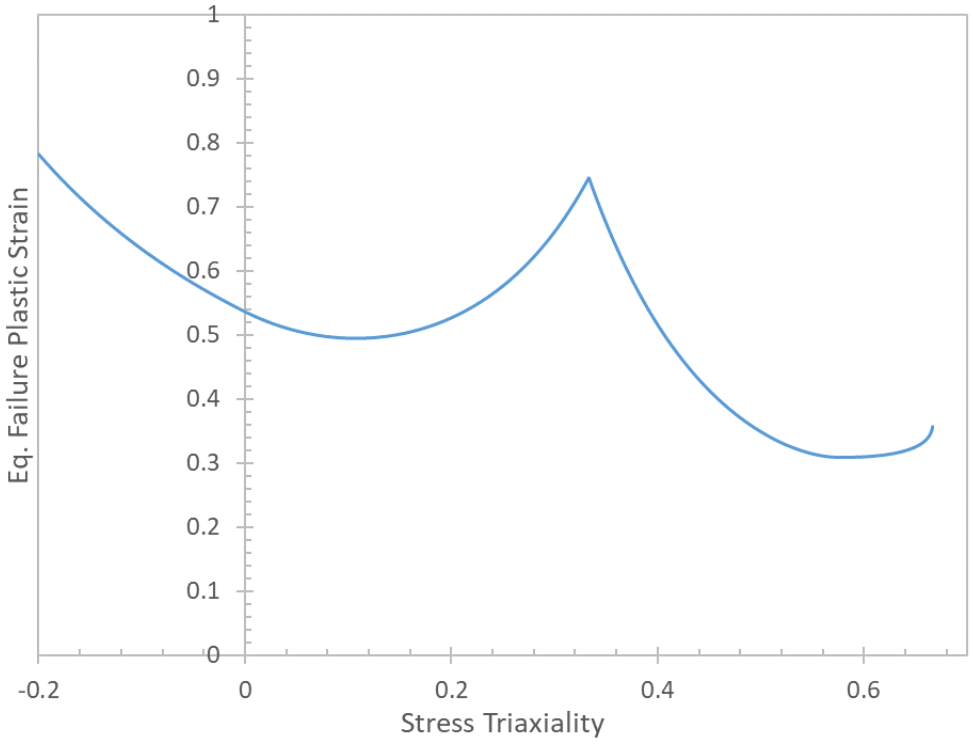

Figure 4.1: Stress triaxiality curve for the fully martensitic microstructure (Ten Kortenaar, 2016; Abedini, 2018)

4.2 Tube Model Creation, Hardness Distribution, and Geometrical Dimensions

As mentioned in Section 3.5.3, the physical hat sections exhibited warpage, particularly the tailored hat sections. The final outputs of the hat section models from the numerical THS process predicted warpage from spring back of the part while it was air cooled. For the purpose of this thesis, a separate intermediate simulation had to be run to flatten out the flanges of the hat section models due to the fact that a flat flange surface was important for defining a

constant bond line thickness. Once the flanges of the hat sections were flattened, the final bonded tube models were assembled in the HyperMesh commercial software (Altair), in which the outputs of the intermediate simulations were mirrored to create two hat sections. Note that the residual stress-strain histories of the steel were not carried over from the output of THS model to the intermediate simulation in which the flanges were flattened, nor from the intermediate simulation to the final tube models. This simplification to neglect the warpage and the resulting residual stresses induced in the bonded structure was a limitation of this study.

Additionally, for the axial crush simulations, a fold initiator was incorporated by displacing specific nodes in the tube to represent the physical deformed geometry. A limitation of this method was that the fold initiator did not include the forming history.

The fold initiator was introduced by moving nodes 4 mm deep at 65 mm from the top end of the hat section model (Figure 4.2). This approach greatly simplified the model creation process, and although it fails to consider local work hardening and thinning, the dimple still provided the necessary geometric discontinuity needed to control folding initiation.

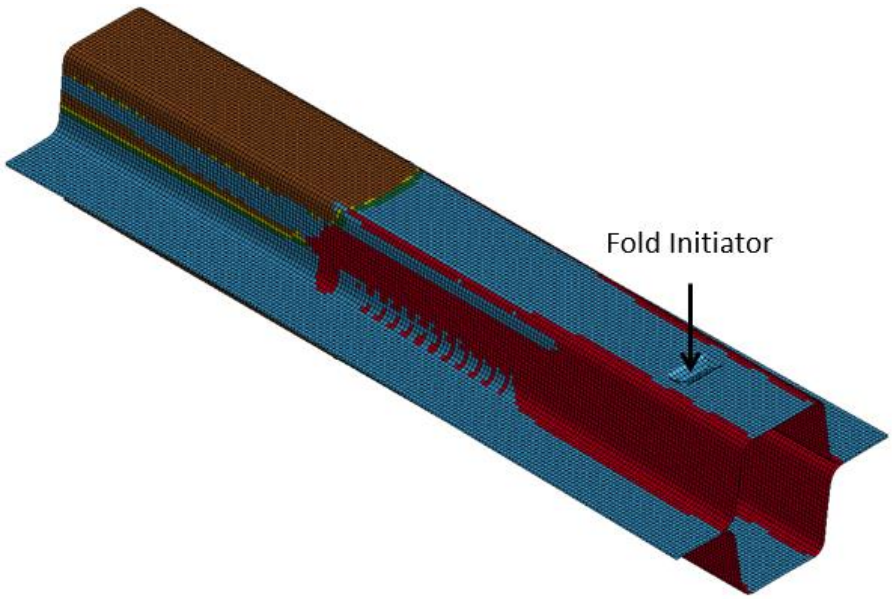

Figure 4.2: A three zone tube model showing the fold initiator, introduced by moving nodes

As shown in Figure 3.12 (Section 3.4), there were some noticeable differences between the physical hardness data of formed hat sections in this thesis and the hardness predicted by Omer *et al.* (2017). In particular, the difference at the top surface for the 700 °C heated end (where the fold initiator was located) was approximately 10%. Note that the Vickers hardness at the fold initiator (at a position mark of 525 mm shown in Figure 3.12) was obtained by linearly interpolating between hardness data points at 560 mm and 440 mm. This difference could affect the predicted loading response since the deformation pattern was established early on during the crush or impact event. By visual inspection, it could be identified that the fold initiator elements and the surrounding elements on the top face were of material bin 2 (weighted average Vickers hardness 270.1; Figure 4.1; Figure 2.23), while the physical hardness data collected for this thesis suggested that the elements in that area should be closer to material bin 1 (weighted average Vickers hardness 209.0). Therefore, a modified three zone

model (Figure 4.3) was created by manually mapping the distribution of bins corresponding to the physical hardness as close as possible without changing the material properties of the bins. According to the physical hardness data, elements roughly in the first 150 mm from the heated end of the hat section should all be in material bin 1 (red). However, this led to an abrupt change from a section of bin 1 elements to a section of bin 2 elements, with a considerable difference in hardness and flow stress properties, which could again interfere with the fold initiation. Hence, an intermediate material bin 1.5 was introduced, starting at 125 mm from the heated end and spanning 50 mm. The flow stress curves in this bin were linearly interpolated between material bins 1 and 2. The loading response and deformation pattern of the three zone model by Omer *et al.* (2017) and the modified three zone model based on physical hardness data will be compared in detail in Chapter 6.

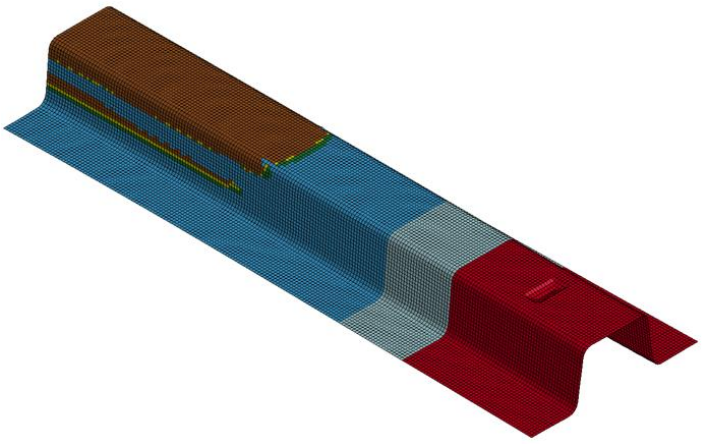

Bin Number	Vickers Hardness Range (Weighted Average)
1	187 – 248 (209.0)
1.5	(~240)
2	249 – 309 (270.1)
3	310 – 372 (331.1)
4	373 – 433 (392.4)
5	434 – 493 (473.5)

Figure 4.3: Modified three zone hat section finite element model, in which bins were mapped according to physical hardness data, and an intermediate material bin was introduced. Material properties in all other bins remained the same and were obtained from Omer *et al.* (2017)

Another critical factor in obtaining accurate numerical results was in the basic geometry of the parts. Considering the numerical models of the hat sections with extended flanges were not derived from the forming simulations (Omer, 2014), as well as unavoidable minute changes to the forming condition due to age of tooling, it was possible that there may be dimensional differences between the current model and the physical hat section. These differences may contribute to inaccuracies in the predicted response of the bonded tubes. Figure 4.4 and 4.5 detail the dimensions measured on the physical hat section and the corresponding values in the numerical models. Note that the measurements were taken at both ends of the hat section for all tailoring configurations, and that the physical top and bottom radii were measured with radius gauges in 0.5 mm increments

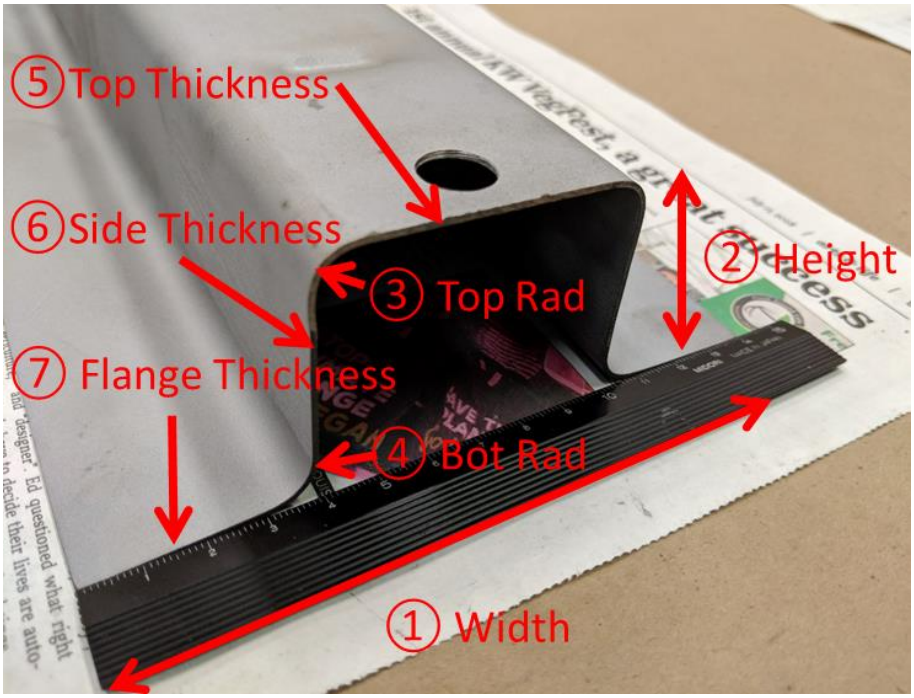

	Martensitic Hat Measurements						
	①	②	③	④	⑤	⑥	⑦
Specimen 1	146.0	50.0	7.5	8.5	1.20	1.17	1.21
	146.0	50.0	7.5	8.5	1.22	1.19	1.22
Specimen 2	146.0	50.0	7.5	8.5	1.22	1.20	1.22
	146.0	50.0	7.5	8.5	1.20	1.18	1.21
Specimen 3	145.0	50.0	7.5	8.5	1.19	1.17	1.20
	146.0	50.0	7.5	8.5	1.21	1.19	1.22
Specimen Avg.	145.8	50.0	7.5	8.5	1.21	1.18	1.21
Model	147.7	48.9	7.9	8.4	1.19	1.16	1.21
% Difference	-1.3	2.2	-5.1	1.2	1.7	2.5	0.4

	600°C Soft Flange Hat Measurements						
	①	②	③	④	⑤	⑥	⑦
Specimen 1	151.0	49.0	7.5	8.5	1.20	1.15	1.20
	151.0	50.0	7.5	8.5	1.22	1.17	1.22
Specimen 2	151.0	49.0	7.5	8.5	1.21	1.15	1.21
	152.0	49.0	7.5	8.5	1.22	1.18	1.22
Specimen 3	151.0	49.0	7.5	8.5	1.21	1.16	1.21
	152.0	50.0	7.5	8.5	1.22	1.19	1.22
Specimen Avg.	151.3	49.3	7.5	8.5	1.21	1.17	1.21
Model	152.9	47.4	7.8	8.4	1.19	1.17	1.22
% Difference	-1.0	4.1	-4.3	1.2	1.6	-0.1	-0.7

Figure 4.4: Detailed dimensions of the fully martensitic and soft flange hat sections

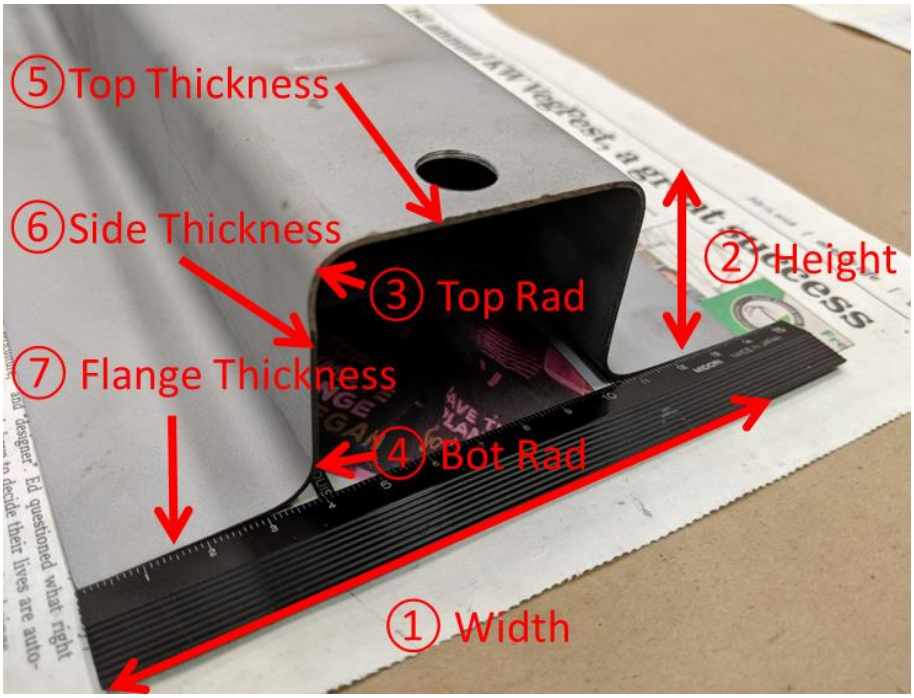

	Three Zone Top (Heated, Softened End) Dimensions						
	①	②	③	④	⑤	⑥	⑦
Specimen 1	142.0	50.0	8.0	8.5	1.19	1.20	1.21
Specimen 2	142.0	50.0	7.5	8.5	1.18	1.18	1.17
Specimen 3	142.0	50.0	7.5	8.5	1.17	1.17	1.16
Specimen Avg.	142.0	50.0	7.7	8.5	1.18	1.18	1.18
Model	152.4	48.0	7.9	8.3	1.21	1.15	1.21
% Difference	-6.8	4.2	-3.0	2.4	-2.6	3.3	-2.8

	Three Zone Bottom (Cooled, Hardened End) Dimensions						
	①	②	③	④	⑤	⑥	⑦
Specimen 1	146.0	51.0	7.5	8.5	1.19	1.17	1.20
Specimen 2	146.0	51.0	7.5	8.5	1.22	1.19	1.21
Specimen 3	147.0	51.0	7.5	8.5	1.22	1.18	1.22
Specimen Avg.	146.3	51.0	7.5	8.5	1.21	1.18	1.21
Model	145.1	49.0	7.6	8.0	1.19	1.19	1.21
% Difference	0.8	4.1	-1.3	6.3	1.5	-0.4	-0.3

Figure 4.5: Detailed dimensions of the three zone hat sections

For the fully martensitic hat sections, all seven numerically predicted dimensions (Omer, 2014) were within 5% deviation from the physical samples. Similarly, for the 600°C soft flange hat

sections, the numerically predicted dimensions were in good agreement with the physical dimensions, with the highest being the top radius at 4.3%. On the other hand, higher deviation was observed for the three zone hat sections, as was expected due to the complexity of the tooling and the lack of complete contact between the part to the tooling as outlined in Section 3.2. For the heated 700°C end, which was also designated as the top end of the hat section, the largest deviation was the physical width (dimension 1) at 6.8% lower than the numerical value. This was likely caused by the protrusion of the heated tooling, causing more of the blank to be drawn in and having a more complete contact, resulting in reduced width in the physical formed part. For the cooled end, designated as the bottom end of the hat section, the largest deviation was in the bottom radius (dimension 4) at 6.3%. Once again, due to the protrusion of the heated tooling, the cooled end was not in complete contact with the tooling, and was likely tilted upward toward the heated end. This, coupled with the measurement inaccuracies associated with the radius gauges, were the likely cause of the large deviation.

Preliminary simulations using Omer's (2014) hat section models with the flanges extended (all dimensions unchanged except the width) revealed two general trends regarding different test modes: the axial crush simulations often over predicted the stiffness of the initial loading response as well as the peak force; and the displacement-to-failure in fully martensitic three-point bend simulations were often over predicted. While the lower measured stiffness of the axial crush experiments was mainly a result of test equipment compliance (detailed in Section 6.2.1), the higher width of the hat section model provided more cross sectional surface area and thus leading to higher peak force. At 1.3% difference, amending the width of the fully martensitic hat section likely would not have contributed to much improvement, and was

therefore left unchanged. At 6.8%, it was much more impactful to amend the width of the three zone hat sections. However, the dimensional measurements were only taken at the ends of the hat sections, and thus the precise width profile along the length of the hat section was unknown, making it difficult to amend the width of the three zone hat sections due to its complex width profile. Therefore, to simplify the hat section model creation process, this dimension was left unchanged and was a limitation of the current study. On the other hand, the height (dimension 2) of the fully martensitic hat section model was identified to be easy to amend since there was less variation in the height profile. An increased side wall height could potentially reduce the predicted displacement-to-failure, since the increased second moment of area adds more overall rigidity to the structure, allowing the adhesive to bear more of the load. Therefore, the height of fully martensitic tube models was raised by 1 mm by extending the side walls in HyperMorph commercial software (Altair).

4.3 CZM Modelling of an Adhesive Joint

The adhesive joint was represented by a single layer of solid cohesive elements with a thickness of 0.178 mm (0.007”), corresponding to the physical thickness of the adhesive joint. A gap of 0.6 mm existed between the adhesive solid cohesive elements and flange shell elements to account for the assigned thickness of the shell elements (Figure 4.6).

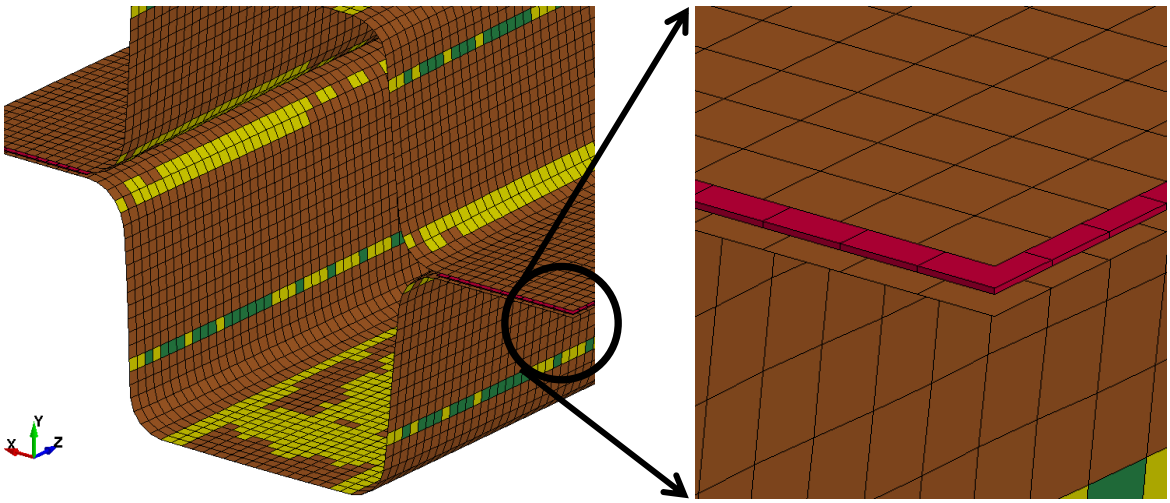

Figure 4.6: Bonded tube model, showing the single layer of solid cohesive elements representing the adhesive layer

Once assembled, the bonded tube model was imported into LS-DYNA, where the single layer of solid cohesive elements was assigned a four-point cohesive element formulation (ELFORM 19). A CZM material model (*MAT_240) was used to define the properties of the adhesive (Table 4.1), as measured from coupon-level RDCB and bonded shear samples (Watson *et al.*, 2018). Since the layer of solid cohesive elements had a thickness corresponding to that of the physical bond line, there was a gap between the adhesive elements and the flange elements due to shell thickness and nodes being at the mid-plane. An offset tied contact (*TIED_SHELL_EDGE_TO_SURFACE_CONSTRAINED_OFFSET) was used in LS-DYNA to define the connection between the adhesive and the flanges to account for shell thickness.

Table 4.1: Material properties and cohesive zone parameters used in the adhesive model (Watson *et al.*, 2018)

Adhesive Model Parameters	Value	Units
Density – RO	1.200e-09	ton/mm^3
Young's Modulus – EMOD	1560	MPa
Shear Modulus – GMOD	615.9	MPa
Mode I Critical Energy Release Rate – $G_{IC,0}$	3.055	kJ/m^2
Mode II Critical Energy Release Rate – $G_{IIC,0}$	12.00	kJ/m^2
Mode I Yield Stress – T0	39.97	MPa
Mode II Yield Stress – S0	25.57	MPa
Mode I Ratio of Plastic to Total Area – FG1	0.1312	
Mode II Ratio of Plastic to Total Area – FG2	0.9000	

4.4 Boundary Conditions and Contact – Quasi-static Test Simulations

To model the reduced physical length of the tube for axial crush tests, approximately 100 mm of elements were deleted from the model (40 rows of elements), both for the fully martensitic and three zone models. For the three zone axial crush models, the elements were deleted from the martensitic end of the tube, corresponding to the material removed from the tubes for the physical experiments. To simulate the fixtures (Figure 4.7) clamping the ends of the tube, the tube nodes within the fixtures were constrained to the fixture (*CONSTRAINED_EXTRA_NODES_SET in LS-DYNA). The constraint may result in a slightly stiffer response as it eliminates compliance in the fixtures, but should suffice as an accurate representation of the boundary conditions since the portion of the tube within the fixture exhibited no deformation during the experiments. The fixtures were modelled according to their physical dimensions.

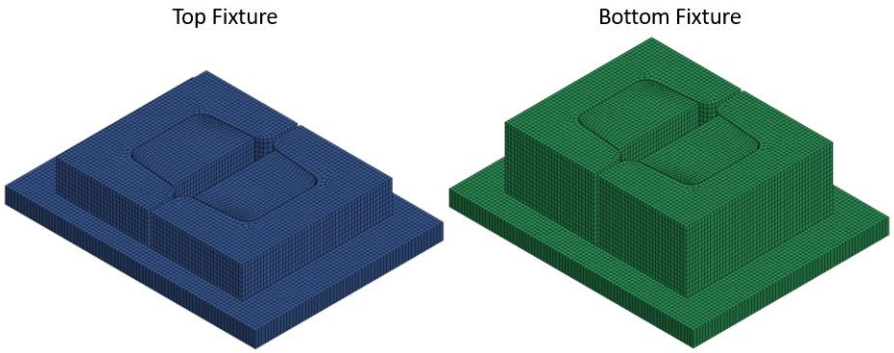

Figure 4.7: Top and bottom fixture used in axial crush models

The bottom fixture was constrained in all degrees of motion, while the top fixture was only allowed translation in the z-axis at a prescribed velocity of 0.5 mm/s (Figure 4.8), following the crosshead velocity used in the experiment. The bosses and clamps used in the axial crush simulations were modeled using 2.5 mm hexahedral elements and treated as rigid. The top fixture was only allowed translation in the z-axis, while the bottom fixture was fixed in all degrees of freedom. Elastic properties of steel were assigned to the fixtures. General contact was established between all parts (fixtures and tube model), with a coefficient of friction of 0.4 (*AUTOMATIC_SINGLE_SURFACE in LS-DYNA).

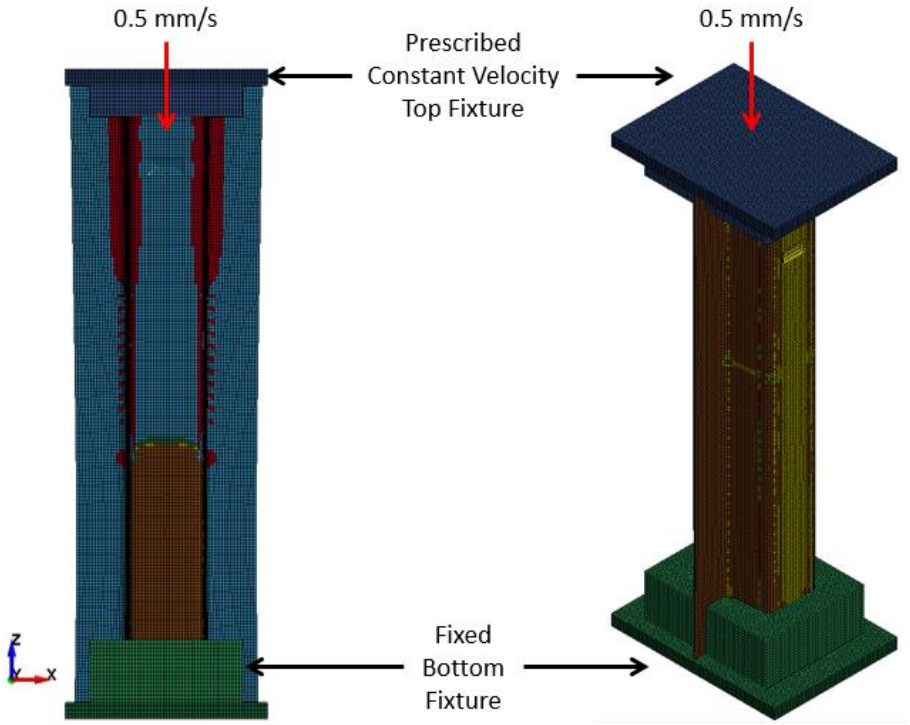

Figure 4.8: Quasi-static axial crush model setup, with prescribed constant velocity on the top fixture

For the three-point bend models, the rigid supports were fixed in all degrees of freedom and were placed 375 mm apart center-to-center. The indentor was only allowed translation in the y-axis at a prescribed velocity of 1 mm/s (Figure 4.9), following the crosshead speed used in the experiment (0.04 in/s). The indentor and supports used in the three-point bend simulations were modeled as rigid materials using 2.5 mm Belytschko-Tsay shell elements with seven integration points through the thickness. The indentor was only allowed translation in the y-axis and the supports, also modeled as rigid, were fixed in all degrees of freedom. General contact was defined between all parts using *AUTOMATIC_SINGLE_SURFACE in LS-DYNA, with a coefficient of friction of 0.4.

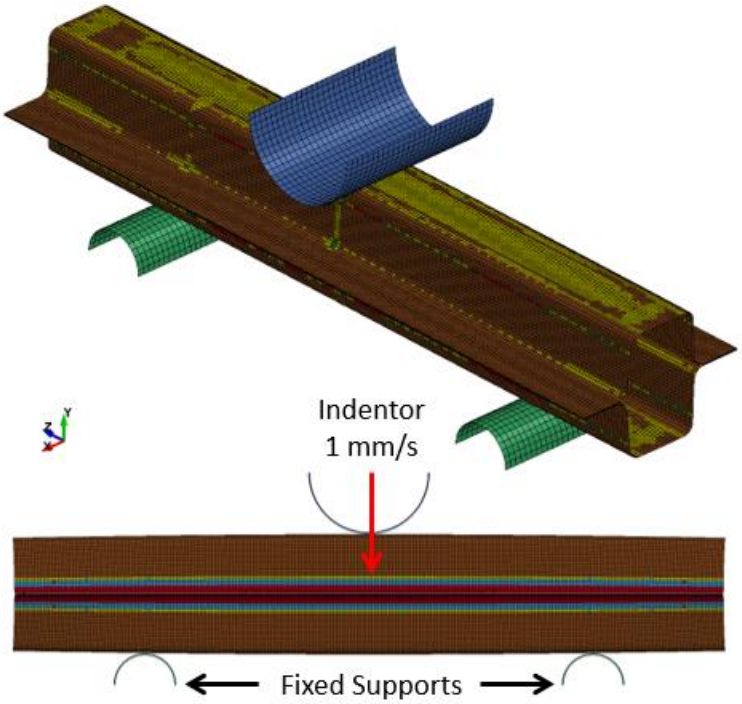

Figure 4.9: Quasi-static three-point bend model setup, with prescribed velocity on the indentor

For the Caiman models, only the inner boss and pins were modeled and the outer clamp was omitted (Figure 4.10). Both the inner boss and pins were modeled as rigid bodies with properties of steel. To model the boundary condition of the front portion of the tube being rigidly constrained in the fixture assembly, the nodes of the tube within the confinement of the fixtures were constrained to the inner boss (*CONSTRAINED_EXTRA_NODES_SET in LS-DYNA). Note that no holes were modeled in the tube, and contact was only defined between the pin and the boss, and between the boss and the tube to avoid contact interactions between the pin and the tube. In the experiments, the portion of the tube near the hole was secured in the fixtures, and the geometric discontinuity had little to no impact on the loading response of the specimen. Therefore, the simplification of omitting the holes in the model should suffice as an

accurate representation of the boundary conditions. Both inner bosses were free in all degrees of motion, while the bottom pin is constrained in all directions, and the top pin was only allowed translation in the vertical (y-axis) direction at a prescribed velocity of 0.833 mm/s. General contact was defined between all parts using *AUTOMATIC_SINGLE_SURFACE in LS-DYNA, with a coefficient of friction of 0.4.

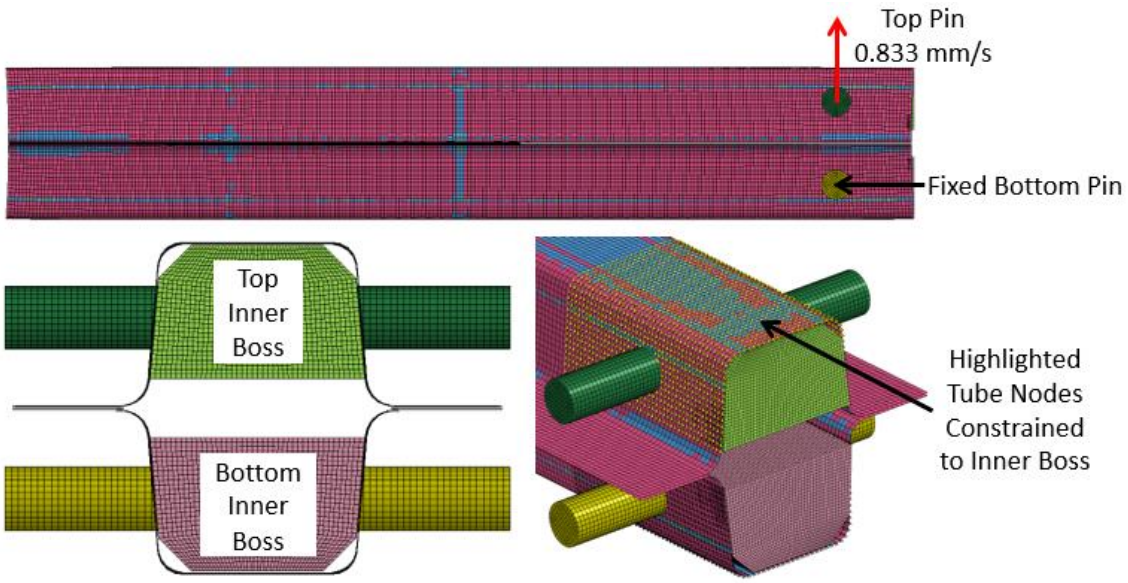

Figure 4.10: Quasi-static Caiman model setup, with prescribed velocity on the top pin.

Note that the prescribed velocities for all quasi-static simulations matched the crosshead velocity used in the respective experiments, and therefore no velocity (time) scaling was used. Instead, in order to maintain a reasonable runtime, all quasi-static simulations used selective mass scaling (DT2MS in LS-DYNA) that added mass to elements with small time steps to achieve a specified time step of $1x10^{-5}$ s. This time step was determined by increasing the minimum time step by an order of magnitude starting from $1x10^{-7}$ s (roughly the time step with no mass scaling) until the total runtime of the simulation was reduced to about 40 hours. There should

be little to no inertial effects affecting the outcome of the simulations, since the prescribed velocities were very low. The validity of this assumption was verified by comparing quasi-static axial crush simulations with and without mass scaling and minimal differences were observed.

4.5 Boundary Conditions – Dynamic Impact Test Simulations

The dynamic boundary conditions for the axial crush and three-point bend models were similar to the quasi-static models (Figure 4.11). However, the crash sled mass was modeled by incorporating a rigid impacting plate (Figure 4.11) made of shell elements with a translational mass of 900 kg. The initial velocity of the plate was 10.5 m/s, as per experimental conditions. For the three-point bend models, the indentor was modeled with shell elements with a translational mass of 870 kg and an initial velocity of 7.5 m/s. It should be noted that the honeycomb crush arrestors used to decelerate the sled in the physical experiments were not modeled in either test simulation. Therefore, only the impact response up to the free crush displacement (145 mm for axial crush, 55 mm for three-point bend) will be compared against the experiment.

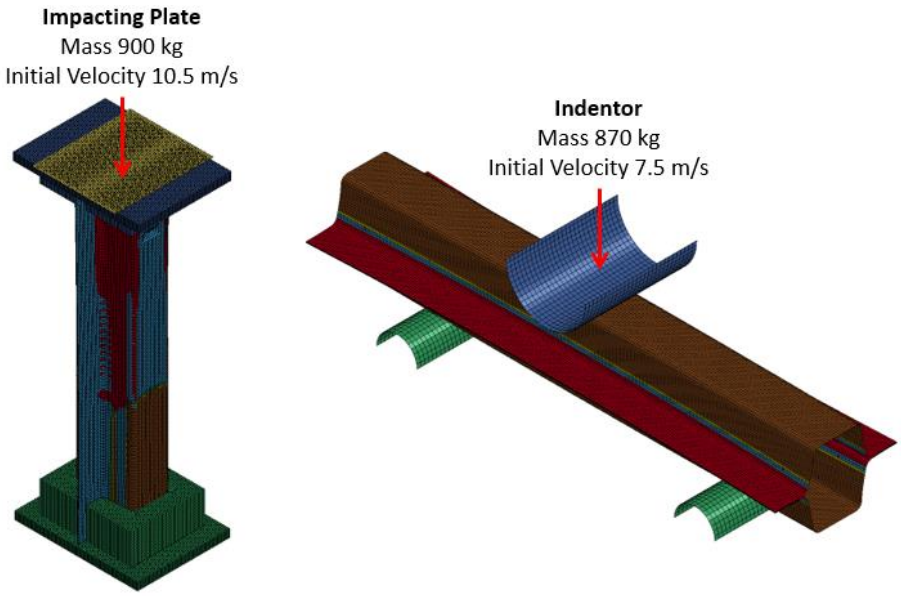

Figure 4.11: Dynamic axial crush model setup (left) and dynamic three-point bend model setup (right)

As mentioned in the experimental setup of dynamic three-point bend experiments in Section 3.7.1, the fully martensitic model also included the two 12.5 mm thick wooden inserts to accurately reflect the physical boundary conditions (Figure 4.12). The wooden insert was made of solid elements and assigned an elastic material model with generic properties of cedar soft plywood as an approximation (Green, Winandy, and Kretschmann, 1999) (Table 4.2).

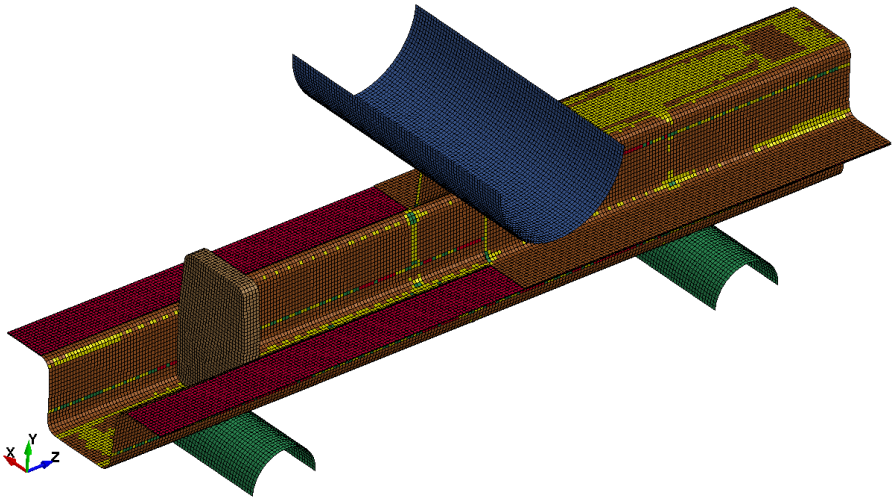

Figure 4.12: Fully martensitic dynamic three-point bend model, with half of the top hat section hidden to show one of the inserts

Table 4.2: Approximation of mechanical properties of wooden insert (Green, Winandy, and Kretschmann, 1999)

Wood Insert Material Properties	Value	Units
Density – RO	4.000e-10	ton/mm^3
Young's Modulus – EMOD	10000	MPa
Poisson's Ratio – PR	0.4000	

Chapter 5 Experimental Results and Discussion

This chapter presents the results of the three sets of experiments comprising the three-point bend, axial crush and Caiman tests. Both static and dynamic results are presented for each. Note that the model predictions and comparison with experiment are presented in Chapter 6.

5.1 Three-Point Bend Experiments

5.1.1 Quasi-Static Three-Point Bend Experiments

Quasi-static three point tests were conducted under four test conditions: 1.8 mm thick QS-3P-FM-GB, 1.2 mm thick QS-3P-FM-GB, 1.2 mm thick QS-3P-FM-AF, and 1.2 mm thick QS-3P-SF-GB. These correspond to fully martensitic (FM) or soft flange (SF) tailored conditions, bonded in an as-formed (AF) or grit blasted (GB) condition. Note that some tests on 1.8 mm thick material were undertaken at the start of the experimental program due to material availability, and that all subsequent test specimens had a thickness of 1.2 mm.

The 1.8 mm thick QS-3P-FM-GB specimens reached an average peak force of 78.8 kN at an average displacement-to-failure of 28.2 mm (Figure 5.1). The 1.2 mm thick QS-3P-FM-GB specimens reached an average peak force of 34.0 kN, but had a large variability in displacement-to-failure (Figure 5.2). The 1.2 mm thick QS-3P-FM-GB-01 test had a similar displacement-to-failure as all the 1.8 mm tests, and displayed a similar symmetric deformation mode where the side walls were crushed equally without any out-of-plane movement. In contrast, the 1.2mm thick QS-3P-FM-GB-02 and QS-3P-FM-GB-03 tests displayed an asymmetric deformation mode, in which one of the side walls was crushed preferentially over the other,

and the top hat section would rotate out of plane (Figure 5.3). This deformation mode significantly delayed the failure of the adhesive joint and the separation of the flange, and therefore increased the total displacement at failure. The 1.2 mm thick QS-3P-FM-GB specimens were the first tests undertaken and used an early method of joining with rectangular shims at the ends of the tube to achieve the bond line thickness, which resulted in inconsistent adhesive coverage across the bond line as mentioned in Section 2.5. Despite this, the failure surface was primarily cohesive.

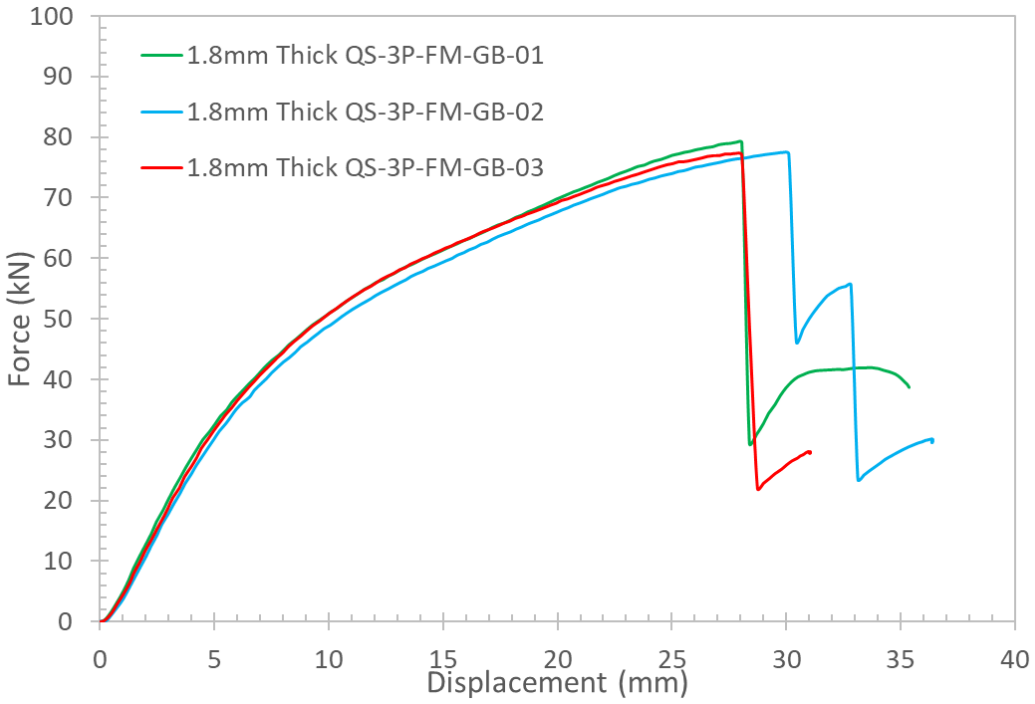

Figure 5.1: Force displacement response of 1.8 mm thick QS-3P-FM-GB tests, in which all the tests exhibited symmetric deformation

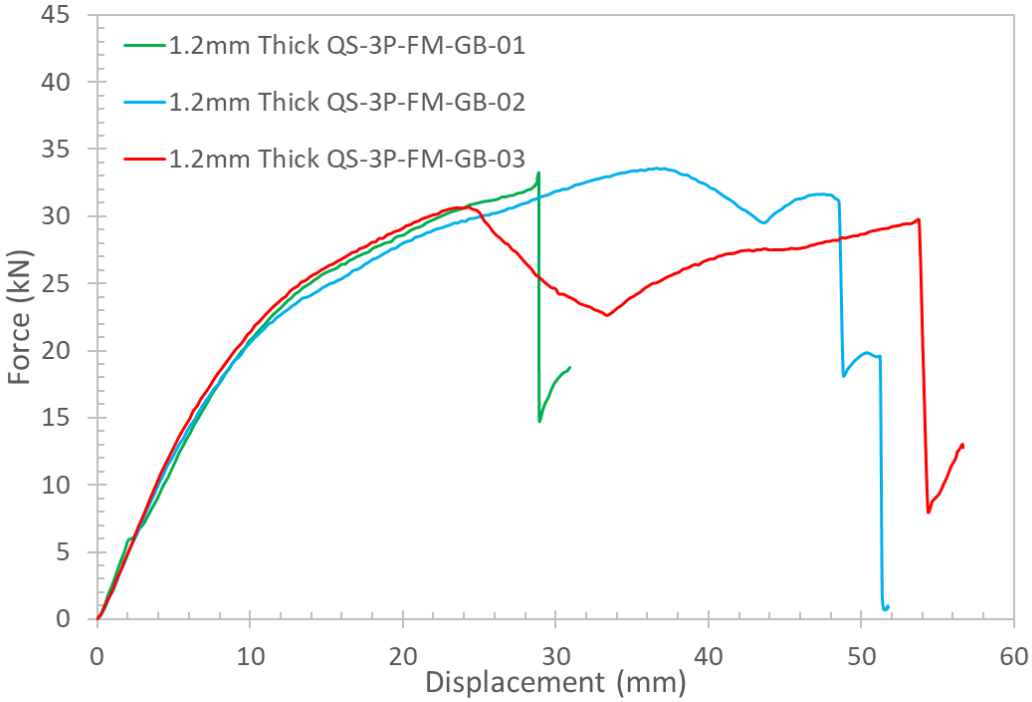

Figure 5.2: Force-displacement response of 1.2 mm thick QS-3P-FM-GB tests, where QS-3P-FM-GB-01 demonstrated symmetric deformation while QS-3P-FM-GB-02 and QS-3P-FM-GB-03 demonstrated asymmetric deformation

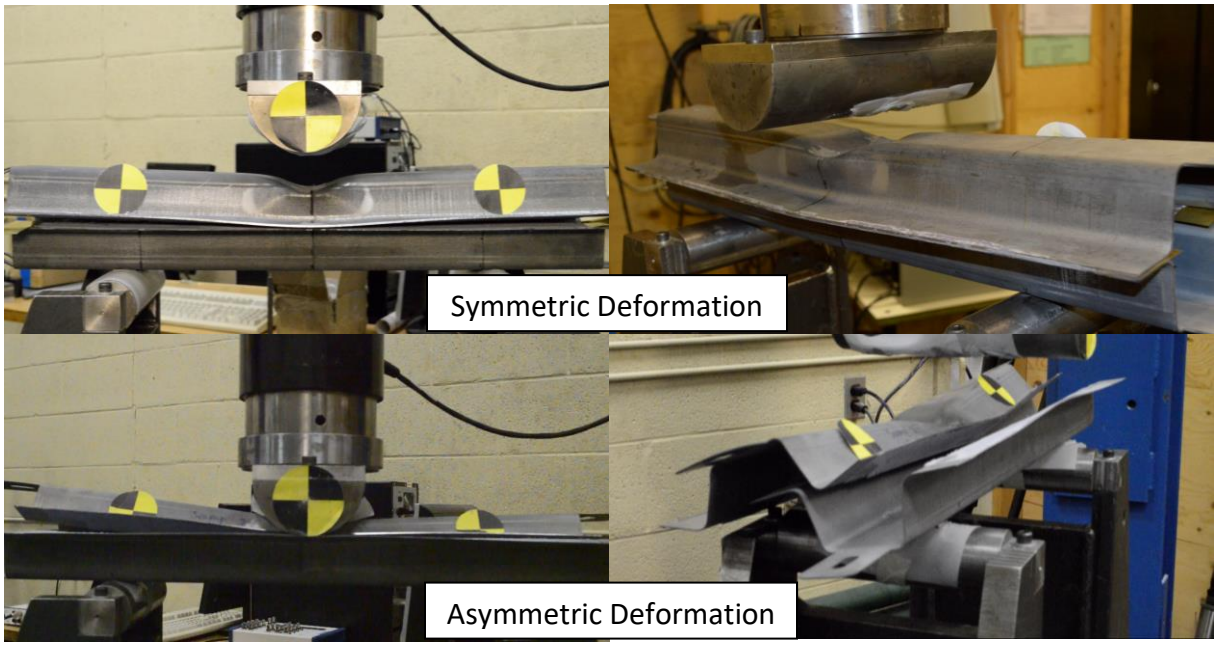

Figure 5.3: Front and side view of a symmetric deformation in quasi-static three-point bend (top), and that of an asymmetric deformation (bottom)

Three test repeats were conducted for the 1.2 mm thick QS-3P-FM-AF condition. The average peak force attained by these specimens was 25.3 kN (Figure 5.4). QS-3P-FM-AF-01 and QS-3P-FM-AF-02 deformed symmetrically, while QS-3P-FM-AF-03 deformed asymmetrically, leading to a lower peak force and higher displacement to failure. The QS-3P-FM-AF specimens were one of the first tests to be bonded with the circular shim method, which distributed the clamping force much more uniformly, resulting in consistent coverage of adhesive across the entire bond line. Although much of the flange separation was a result of interfacial failure (Figure 5.5), it can be seen that when the patches of adhesive on opposing flanges were "pieced" together, full adhesive coverage was achieved on the joint.

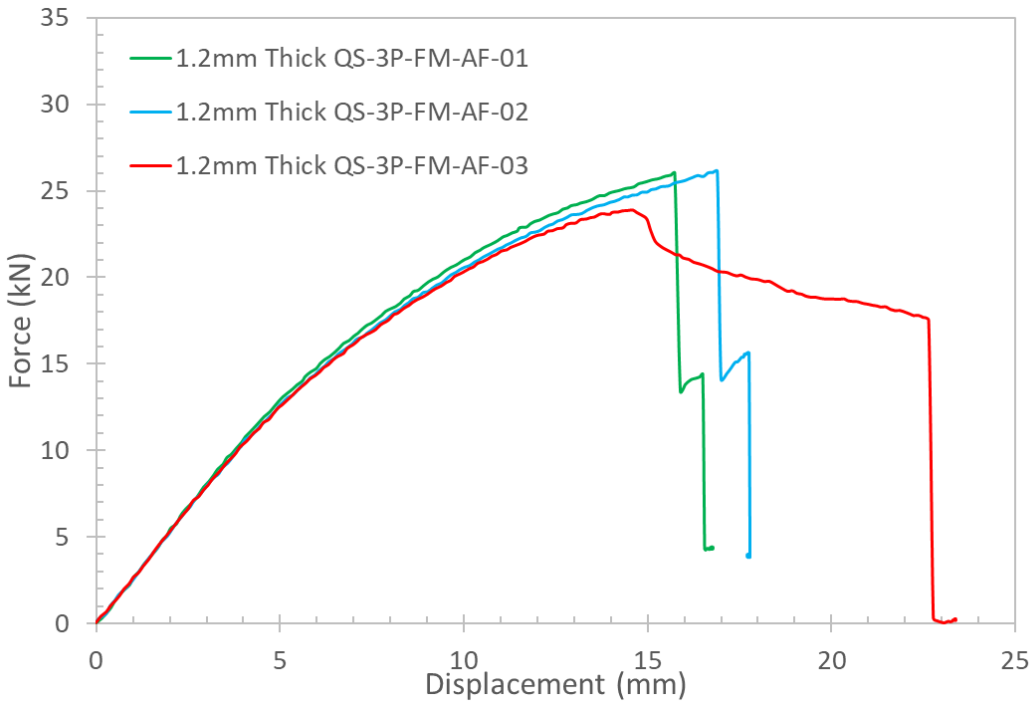

Figure 5.4: Force-displacement response of 1.2 mm thick QS-3P-FM-AF tests, in which QS-3P-FM-AF-01 and QS-3P-FM-AF-02 demonstrated symmetric deformation while QS-3P-FM-AF-03 demonstrated asymmetric deformation

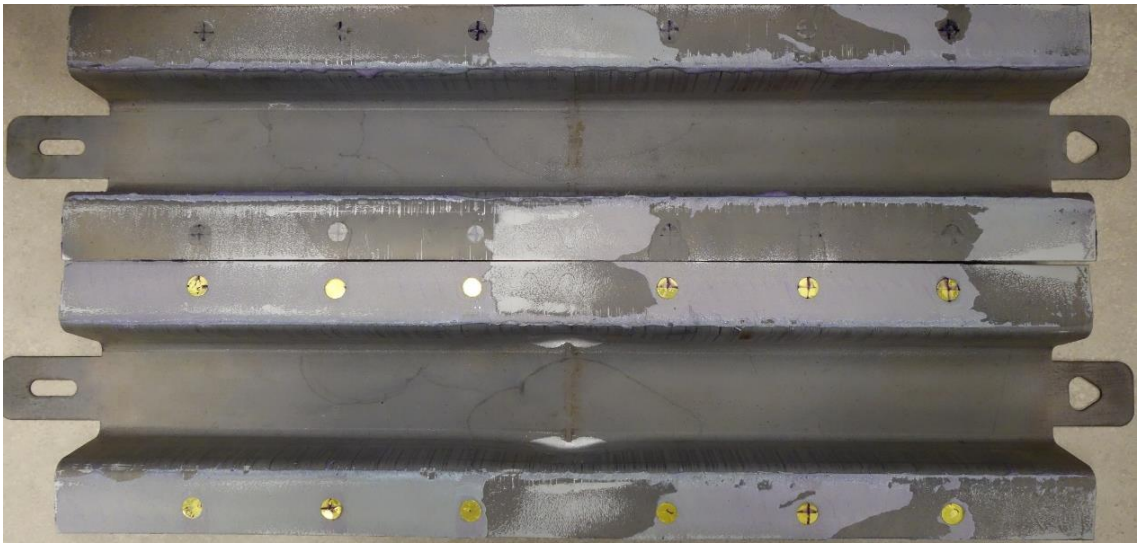

Figure 5.5: Failure surface of 1.2 mm thick QS-3P-FM-AF test, showing interfacial failure, but also the uniform adhesive coverage due to the improved circular shimming technique

Three test repeats were conducted for the 1.2 mm thick QS-3P-SF-GB condition. An average peak force of 23.1 kN was attained by these samples (Figure 5.6). An interesting behavior unique to the soft flange specimens was that the flanges did not abruptly separate compared to the martensitic specimens due to minimal adhesive failure at maximum piston displacement. Only a small amount of cohesive failure was observed at the inside edge of the flange, at the ends of the tubes. Note that for all previous quasi-static three-point bend tests, the test was terminated when one or both of the adhesive joints at the flanges separated. Since no flange separation occurred for the soft flange tests (Figure 5.7), the test was terminated at a stroke length of roughly 177.8mm (7 inches) to prevent the top hat section from contacting the piston. The observable failure surface appeared to be cohesive failure and had good adhesive coverage.

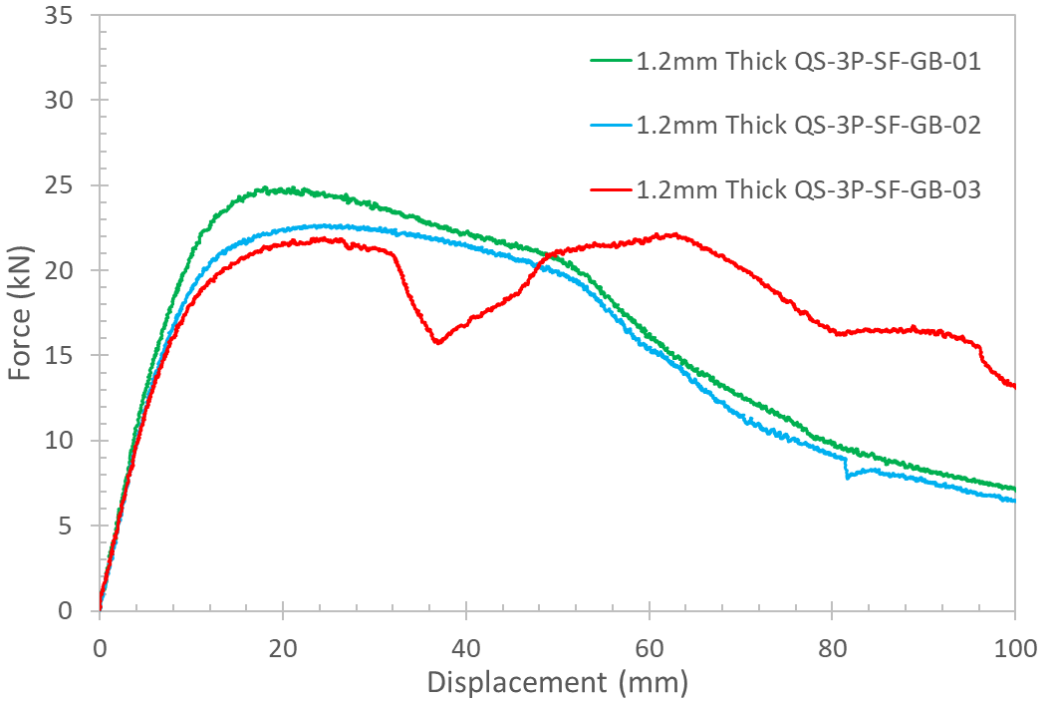

Figure 5.6: Force-displacement response of 1.2 mm thick QS-3P-SF-GB tests, in which QS-3P-SF-GB-01 and QS-3P-SF-GB-02 experienced symmetric deformation while QS-3P-SF-GB-03 demonstrated asymmetric deformation

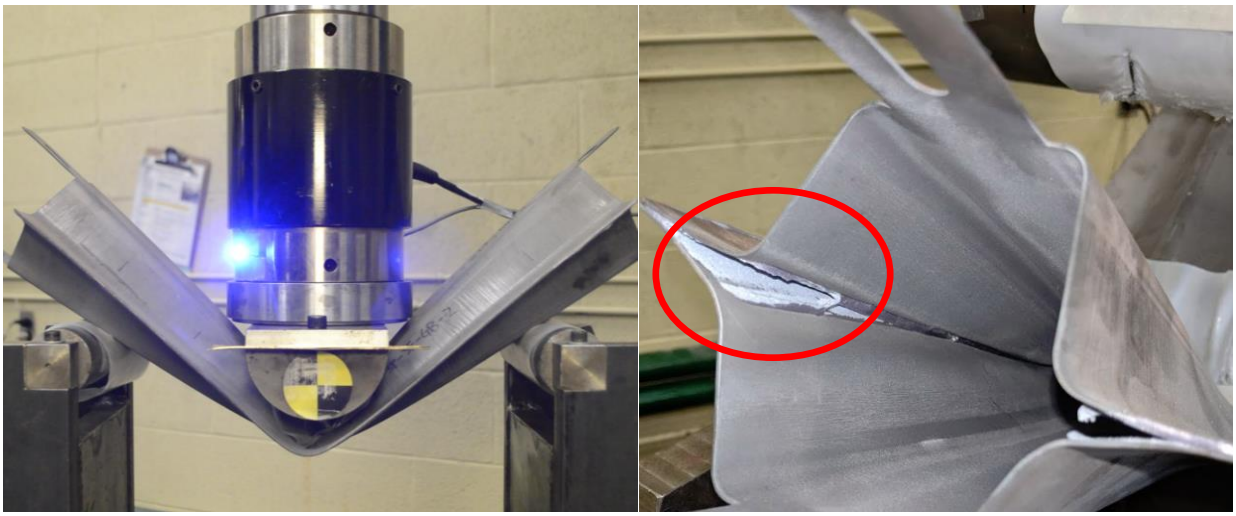

Figure 5.7: End of indentor stroke during a 1.2 mm QS-3P-SF-GB test, showing that adhesive failure is minimal and only at the inner edges of the flange at the ends of the tube

Comparing the loading response of 1.8 mm thick QS-3Z-FM-GB, 1.2 mm thick QS-3Z-FM-GB, 1.2 mm thick QS-3Z-FM-AF, and 1.2 mm thick QS-3Z-SF-GB tests (Figure 5.8), it could be seen that

all the 1.8 mm thick specimens failed under symmetric deformation and had more consistent response compared to the 1.2 mm thick specimens. While it could be difficult to establish the root cause with only a few test repeats, the asymmetric deformation mode was likely a result of the thinner material being inherently less geometrically stable, since none of the 1.8 mm tests exhibited this deformation mode, while four of the nine 1.2 mm tests deformed asymmetrically. Comparing the as-formed and grit blasted surfaces for the fully martensitic specimens revealed roughly a 34% increase in joint strength when the flanges were grit blasted. The soft flange specimens exhibited minimal adhesive failure and lower peak force than the fully martensitic specimens with similar surface preparation, since the work done by the piston largely contributed to plastic deformation of the steel tube.

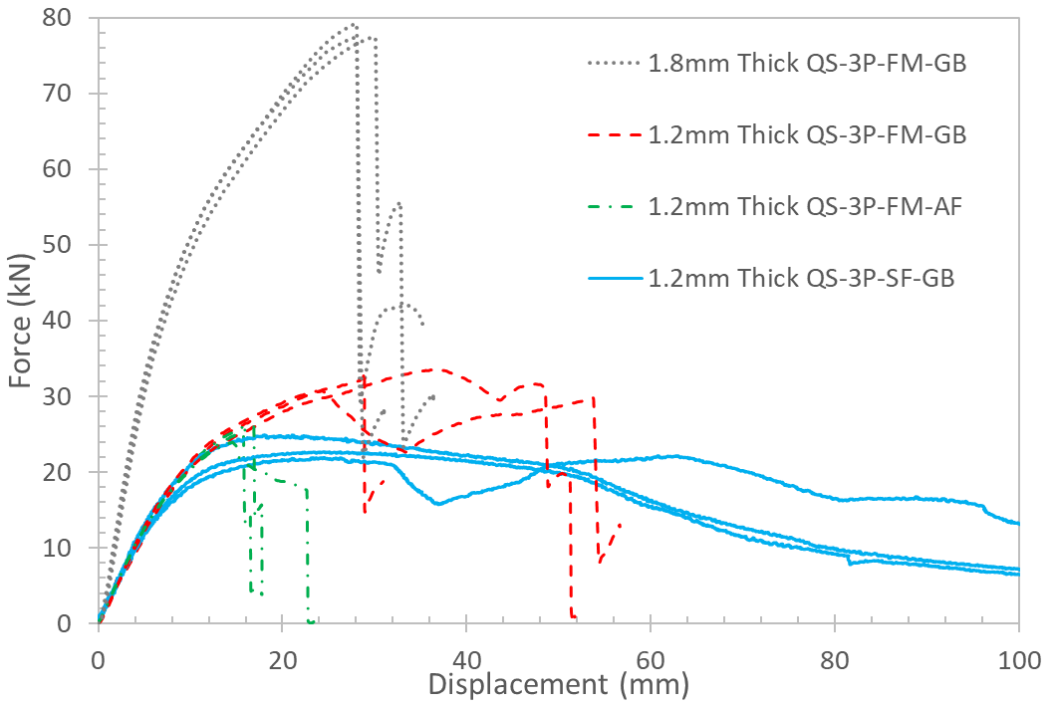

Figure 5.8: Comparison of loading responses of 1.8 mm thick QS-3P-FM-GB, 1.2 mm thick QS-3P-FM-GB, 1.2 mm thick QS-3P-FM-AF tests, and 1.2 mm thick QS-3P-SF-GB

5.1.2 Dynamic Three-Point Bend Experiments

Three test repeats were conducted for the 1.2 mm DM-3P-FM-GB condition. Note again that no software filtering was applied to the load cell and accelerometer data acquisition system. Figure 5.9 shows the individual and average unfiltered forces measured by the two sled-mounted load cells and the corresponding energy absorbed by the tube. Although the overall force- and energy-displacement crush responses were consistent across all three tests, the physical deformation mode of the third test differed from the first two. A symmetric crushing mode was observed for the first two tests (Figure 5.10), whereas the third test demonstrated an asymmetric crush response (Figures 5.11). In both crush modes, however, separation of the flange(s) occurred at the same time as the sled came into contact with the honeycomb, which occurred at the end of the specimen free crush distance. This explained that the peak force of all three tests being coincident with the honeycomb contact as shown in the force displacement plots, since the honeycomb provided a much larger deceleration to the sled compared to the tubes. The failure surfaces were primarily cohesive failure and had good coverage. Note again that wooden inserts were placed inside the tube for the DM-3P-FM-GB experiments only. The inserts did not prevent an asymmetric crush mode as initially intended, which was evident in DM-3P-FM-GB-03, and were therefore removed for all subsequent dynamic three-point testing.

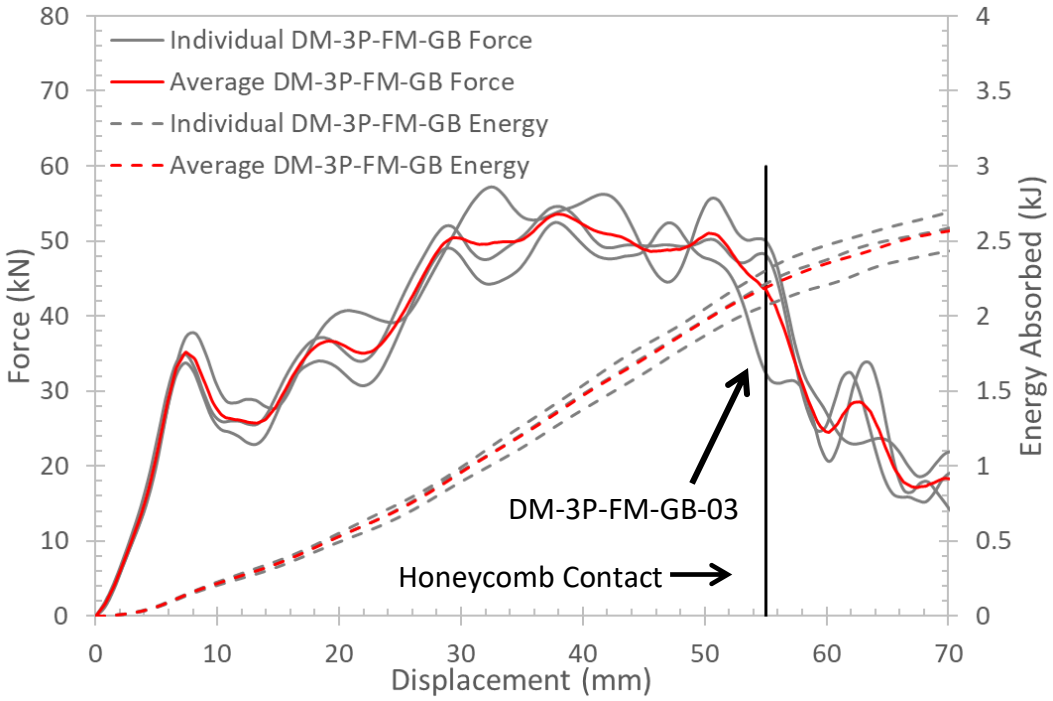

Figure 5.9: Loading response and energy absorbed by DM-3P-FM-GB specimens

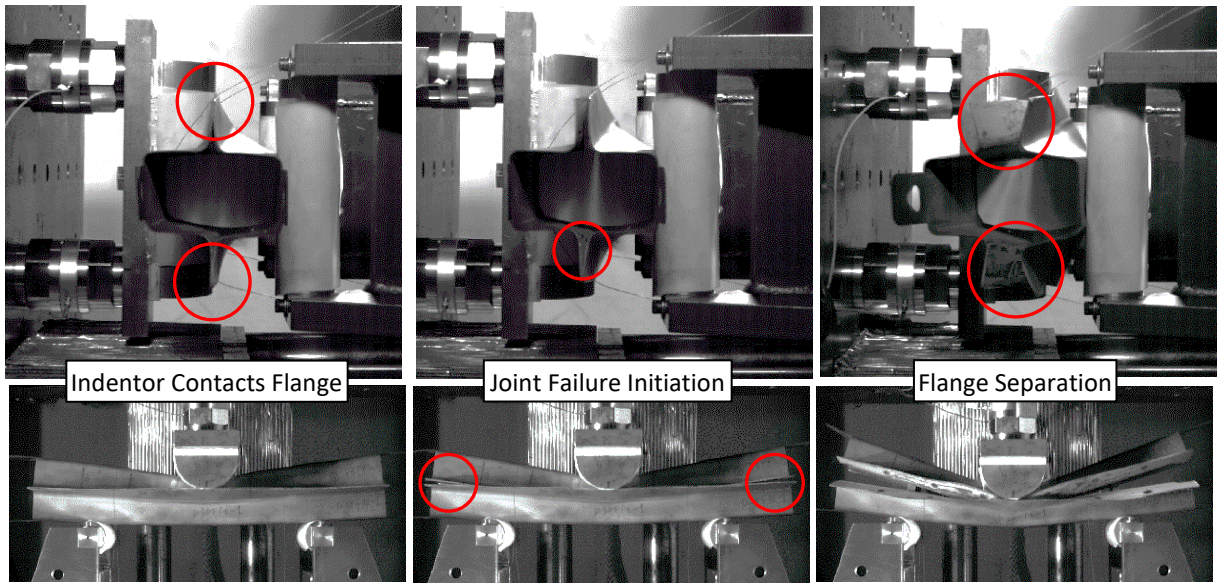

Figure 5.10: Symmetric deformation mode in DM-3P-FM-GB-01 and DM-3P-FM-GB-02, showing flange separating just after indentor contacts the flange, coinciding with sled contacting honeycomb

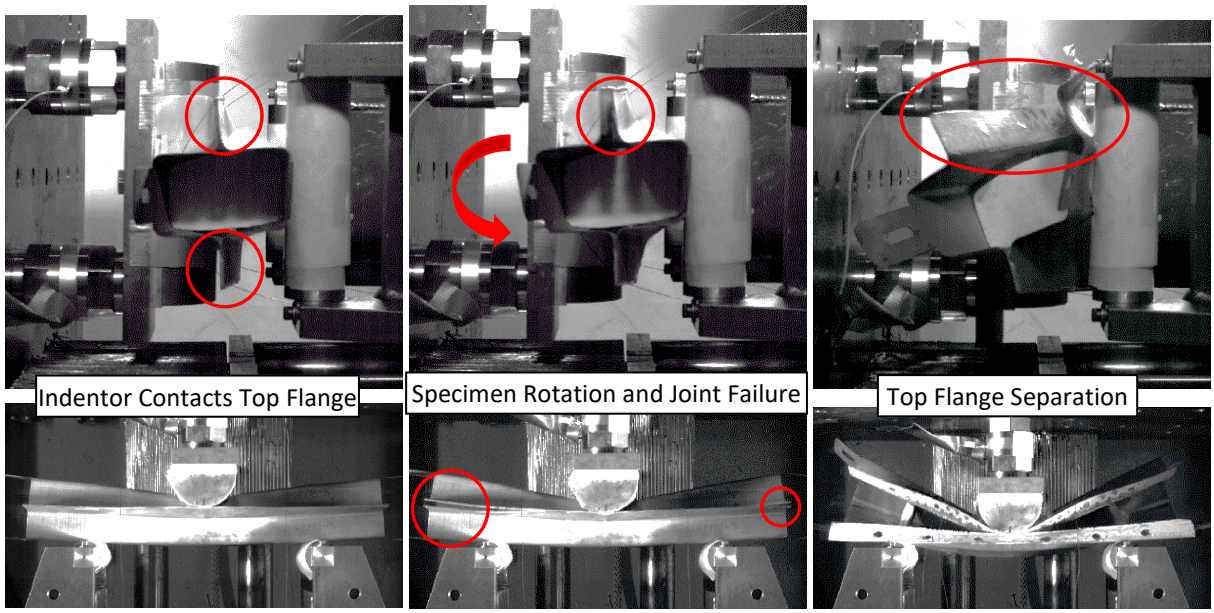

Figure 5.11: Asymmetric deformation mode in DM-3P-FM-GB-03

Three test repeats were conducted for the DM-3P-SF-GB condition. Note that due to a load cell malfunction, no usable data was collected during the DM-3P-SF-GB-01 test, and only one of the two load cells collected data in the DM-3P-SF-GB-02 and DM-3P-SF-GB-03 tests. For these tests, the load measured by the functioning load cell was doubled assuming that the functioning load cell measured roughly half the total force. The average SF curves shown in Figure 5.12 was averaged between the second and third tests. Although each of the two load cells may not necessarily measure precisely half the total force, the assumption was verified against accelerometer data and was generally in good agreement. The unfiltered force-displacement loading response (Figure 5.12) for both tests were similar, as well as the physical deformation mode. Immediately upon impact, the tube as whole began to globally deform at the side wall radii such that the height of the entire tube decreased while the width increased (Figure 5.13). This is in contrast with the fully martensitic tests, where the deformation was primarily local

beneath the indentor. As the test progressed and the indentor approached the flange; however, the deformation shifted from global collapsing of the tube to localized bending of the specimen, inducing plastic deformation of the steel towards the center of tube, while the outer ends were relieved of the elastic deformation (Figure 5.13). The adhesive joint did not fail up to the maximum deformation occurring during the test. Minimal adhesive failure was observed in the inner edges of the flange at the ends of the tube, similar to the QS-3P-SF-GB experiments. The observable failure surface appeared to cohesive failure and had good adhesive coverage.

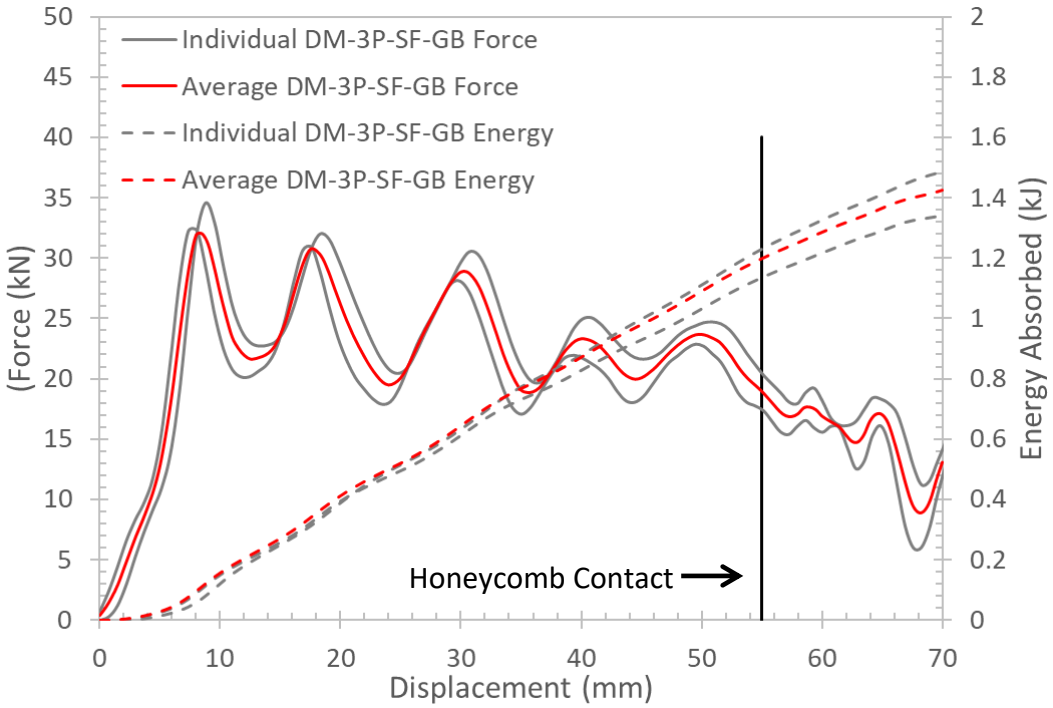

Figure 5.12: Loading response and energy absorbed by DM-3P-SF-GB specimens

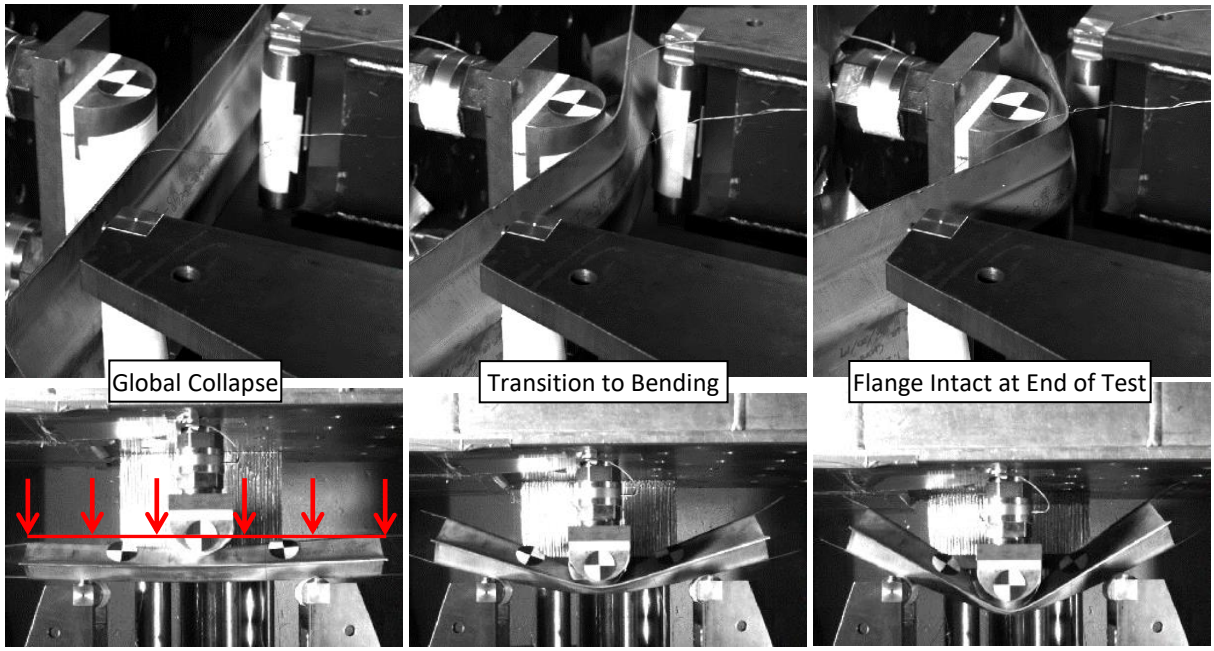

Figure 5.13: Deformation mode of DM-3P-SF-GB, starting with a global collpase of the tube (left), then bending once the indentor contacts the flange (center), but the flange still holds together at the end of the test (right)

Comparing the loading response of DM-3Z-FM-GB and DM-3P-SF-GB tests (Figure 5.14), it could be seen that the fully martensitic specimens attained a slightly higher force at the initial peak just before 10 mm of displacement. While the measured force during the soft flange tests decreased after this initial peak, the fully martensitic specimens experienced a second peak force around 30 mm of displacement that was considerably higher than the initial. Although the wooden inserts did not prevent an asymmetric deformation mode as originally intended, the added rigidity was likely the cause of the fully martensitic specimens to exhibit a second peak force. As a result of this second peak, the fully martensitic specimens absorbed significantly more energy than the soft flange specimens.

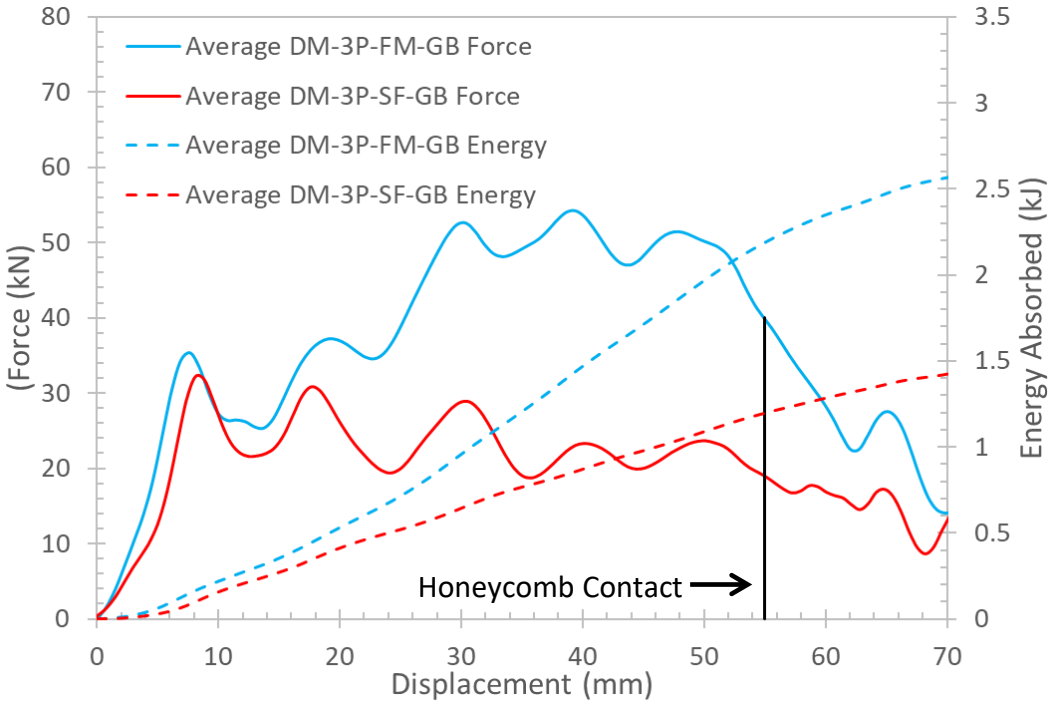

Figure 5.14: Comparison of average force and energy displacement response for DM-3P-FM-GB and DM-3P-SF-GB specimens

5.2 Axial Crush Experiments

5.2.1 Quasi-static Axial Crush Experiments

Three test repeats were conducted for the 1.2 mm QS-AX-FM-GB condition. The average peak force attained was 260.1 kN and the average energy absorbed was 8.5 kJ. Figure 5.15 below shows the force and energy displacement plots for each individual tests as well as the average. Of the three tests, only the QS-AX-FM-GB-01 test developed a folding (local) deformation mode at the fold initiator (Figure 5.16). The adhesive joint adjacent to the fold initiator failed as the fold developed, but the crack in the adhesive joint did not propagate much further down the tube until a second fold initiated. As the second fold developed, the adhesive joint crack propagated through to the rest of the tube. A local folding deformation mode meant that the

crack propagation of the adhesive joint was more controlled and did not extend much ahead of the actual crush zone. In contrast, the QS-AX-FM-GB-02 and the QS-AX-FM-GB-03 test both experienced adhesive failure near the middle of tube that quickly propagated throughout the adhesive bond line, resulting in a global buckling deformation mode (Figure 5.17). Despite different deformation modes, extensive tearing and fracture was observed for all tubes, as was expected for this strong, but brittle martensitic material condition. The QS-AX-FM-GB tests were also one of the earlier tests undertaken that were bonded with the earlier rectangular shim methodology. As such, the failure surface was primarily cohesive but coverage was not uniform.

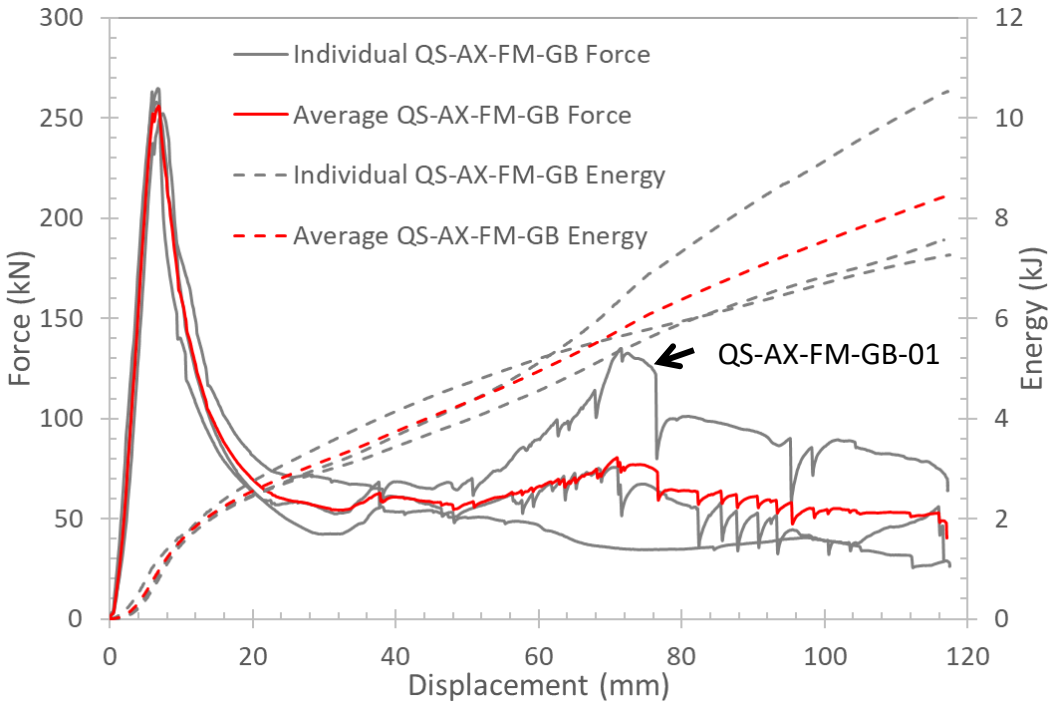

Figure 5.15: Loading response and energy absorbed by QS-AX-FM-GB specimens

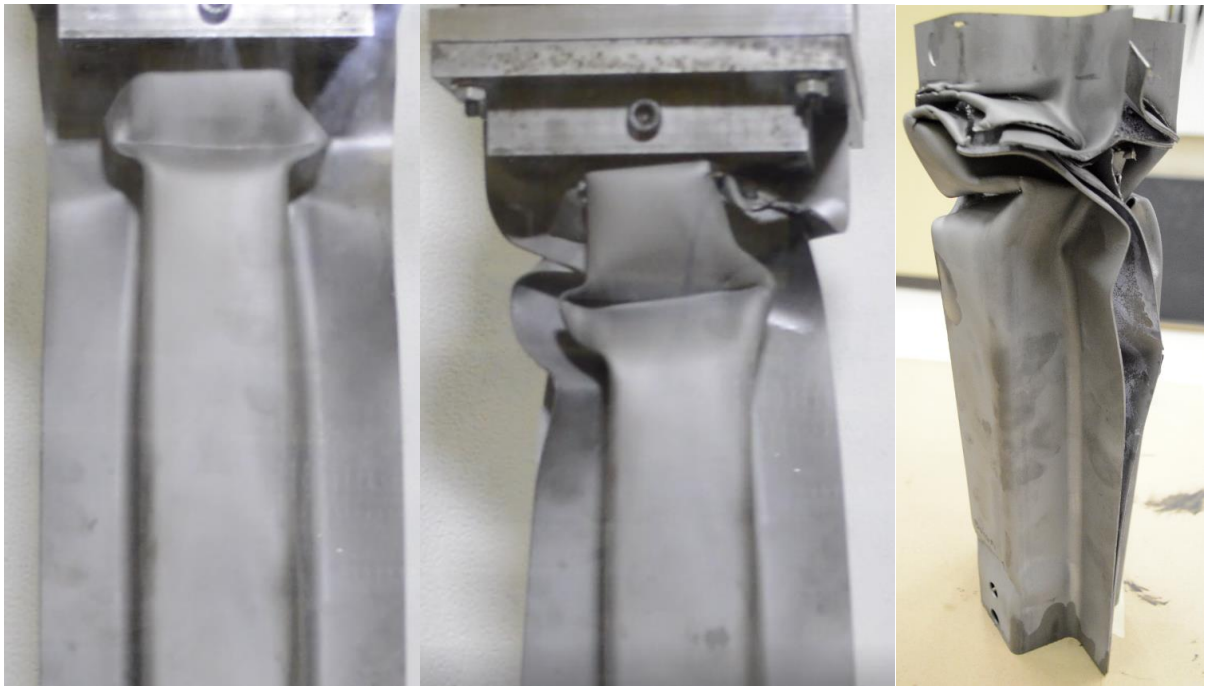

Figure 5.16: Folding (local) deformation mode as observed in QS-AX-FM-GB-01, where separation of flange is controlled

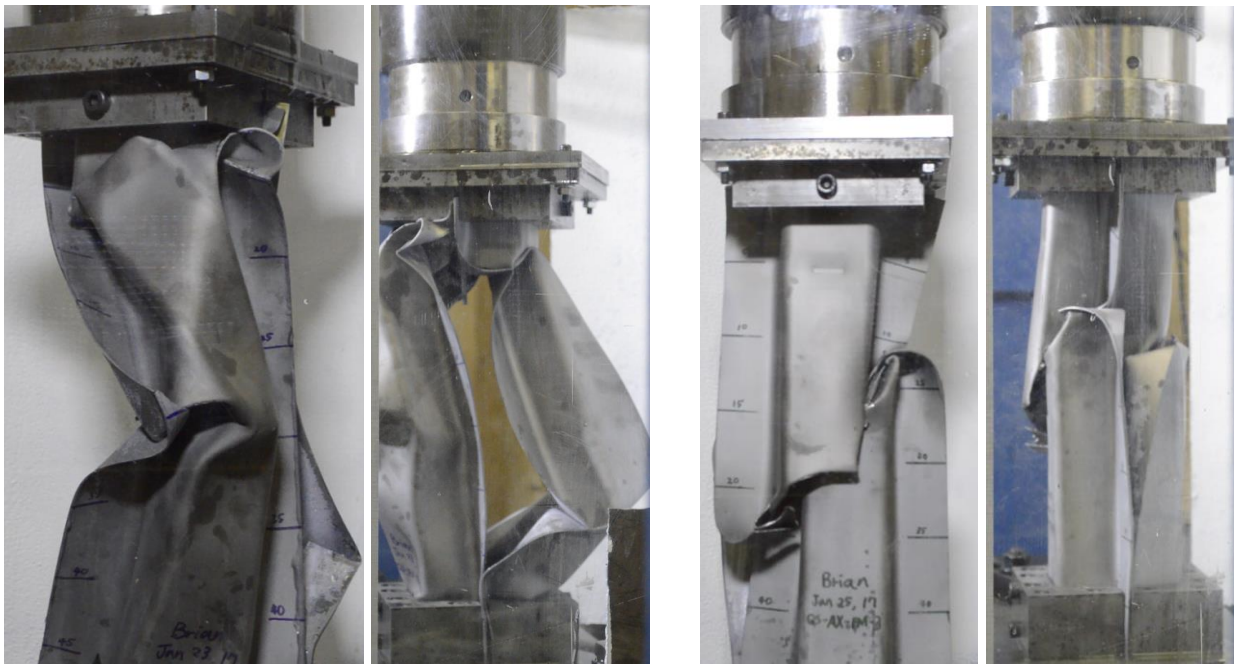

Figure 5.17: Buckling (global) deformation mode in QS-AX-FM-GB-02 and QS-AX-FM-GB-03, in which the specimens exhibited extensive adhesive failure leading to total flange separation

Three test repeats were conducted for the QS-AX-3Z-GB (three zone tailored) condition, for which the average peak force attained was 147.8 kN and average energy absorbed at 120 mm of displacement was 7.3 kJ (Figure 5.18). The fold initiator triggered a local folding deformation mode for all three tubes and continued through the end of the piston stroke of 250 mm (Figure 5.19). Also seen in Figure 5.19, the crack propagation of the adhesive joint was controlled, and most of the flange remained intact below the crush zone. Due to the softening of the in-die heated 400°C and 700°C zones, the upper half of the tube was much easier to deform plastically without fracture, and only a small degree of fracture was observed in the second sample due to an unusual folding pattern. The unusual folding pattern was caused by a slight slippage in the top fixture, such that the upper portion of the tube, where folds had already developed, was displaced off center axis relative to the bottom fixture. As the deformation progressed, the side of the tube opposite to where the upper half of the tube leaned towards was pushed out, as opposed to being folded in. Eventually, the bulge exhibited metal fracture towards the end of the test due to a tight fold. As a result of the flanges being largely held together throughout the length of the flange for all specimens (Figure 5.20), it was difficult to assess much of the failure surface, but cohesive failure was observed for the areas that could be seen. Joint failure was cohesive and adhesive coverage was good.

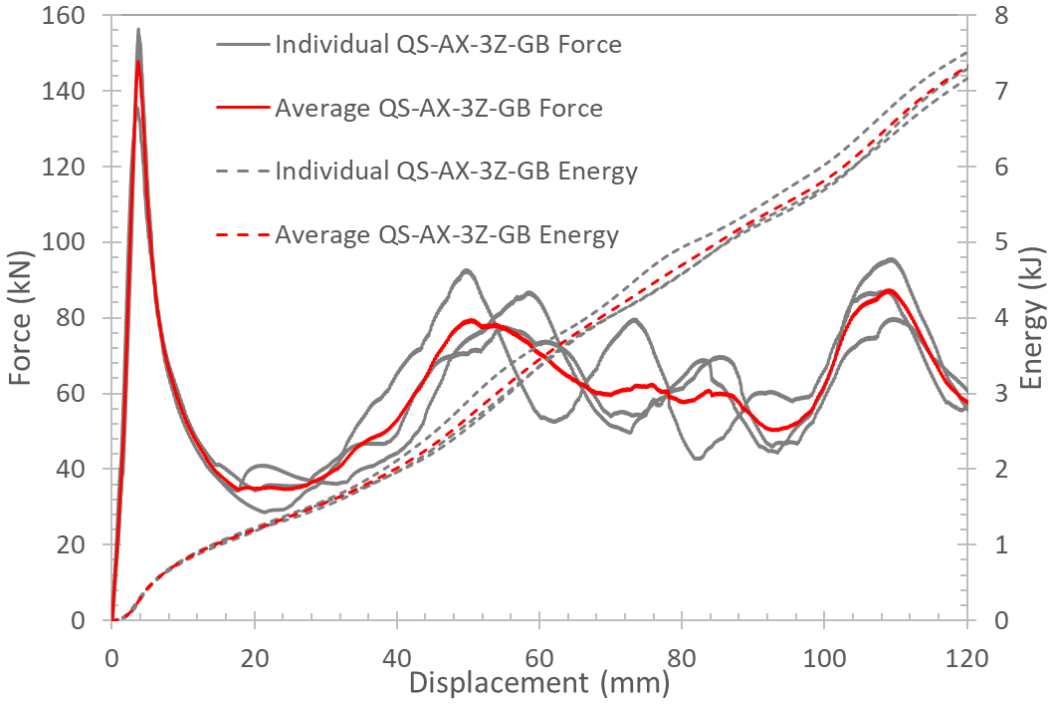

Figure 5.18: Loading response and energy absorbed by QS-AX-3Z-GB specimens

Figure 5.19: QS-AX-3Z-GB specimens demonstrating folding deformation during quasi-static axial crush experiment, with very minimal flange separation

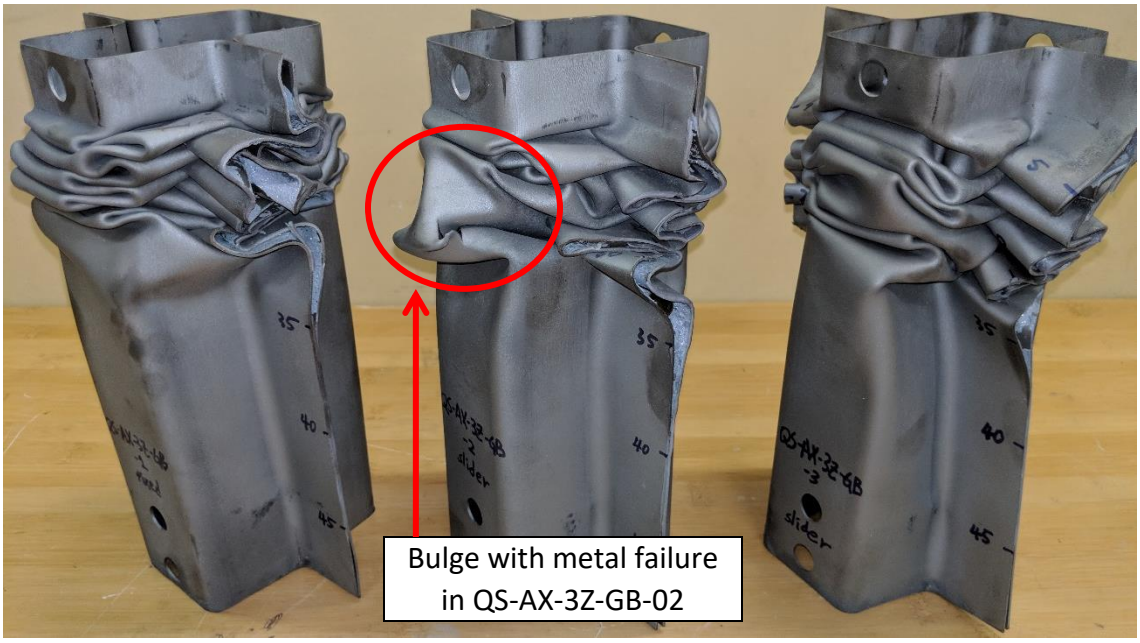

Figure 5.20: Final deformed state of QS-AX-3Z-GB specimens, note that the bulge with metal failure in QS-AX-3Z-GB-02 was caused by fixture slippage

Three test repeats were conducted for the QS-AX-3Z-AF condition, in which the average peak force attained was 142.3 kN and the average energy absorbed was 6.4 kJ (Figure 5.21). The reduction in the overall joint strength due to bonding the as-formed surfaces can be seen in Figure 5.22, in which although the fold initiator triggered a fold, the extent of adhesive failure was much larger than that observed in any of the QS-AX-3Z-GB specimens. The crack opening then grew rapidly throughout the length of the flange, and eventually the local folding deformation mode transitioned to a global buckling mode. The crack propagation was largely the result of interfacial failure of the adhesive joint, as was expected for this surface preparation condition (Figure 5.23). Failure surface was largely interfacial but the adhesive coverage was good.

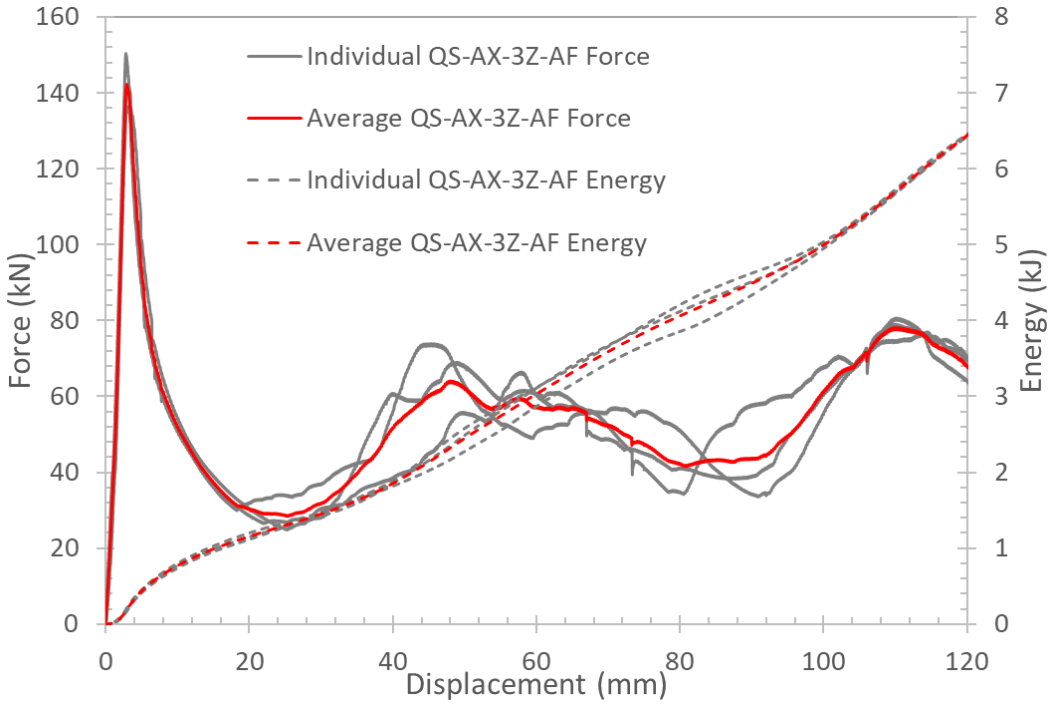

Figure 5.21: Loading response and energy absorbed by QS-AX-3Z-AF specimens

Figure 5.22: Deformation mode of QS-AX-3Z-AF specimens, initiating with folding then transitioning to global buckling due to extensive flange separation

Figure 5.23: Final deformed state of QS-AX-3Z-AF specimens, showing extensive flange separation and interfacial adhesive failure

Comparing the loading response of QS-AX-FM-GB, QS-AX-3Z-GB tests, and QS-AX-3Z-AF tests (Figure 5.24), it could be seen that the fully martensitic specimens attained the highest peak force and energy absorption. However, the three zone specimens exhibited little to no metal fracture, and the overall deformation pattern was more controlled with consistent development of folds. In particular, the grit blasted three zone specimens also exhibited the least amount of adhesive failure and flange separation. Comparing the as-formed to the grit blasted surface for the three zone specimens, it could be seen that having grit blasted flanges resulted in a 3.9% increase in peak force, and 14.1% increase in energy absorbed.

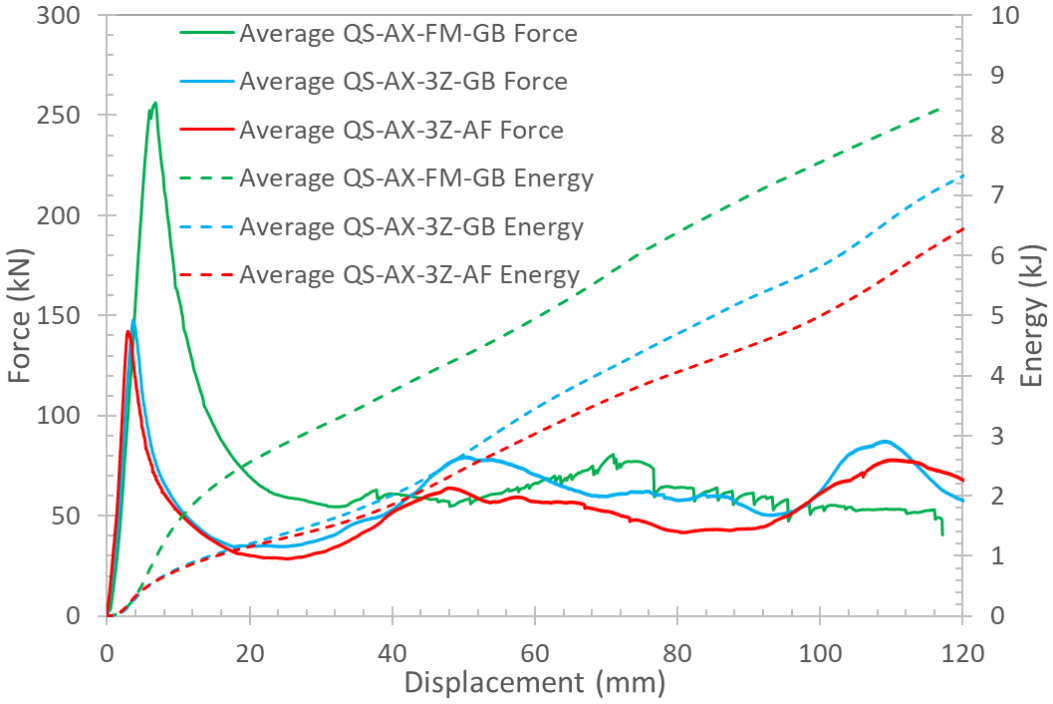

Figure 5.24: Comparison of average loading response and energy absorption of QS-AX-FM-GB, QS-AX-3Z-GB, and QS-AX-3Z-AF tests

5.2.2 Dynamic Axial Crush Experiments

Three test repeats were conducted for the 1.2 mm DM-AX-FM-GB condition. Note again that no software filtering was applied to the load cell and accelerometer data acquisition system. All three specimens experienced folding at the start of the impact, but only the third specimen was able to sustain the folding deformation mode continuously until the end of the experiment. The force displacement crush responses of the tubes are summarized in Figure 5.25. After the first one or two folds, the DM-AX-FM-GB-01 and DM-AX-FM-GB-02 tests experienced a high degree of adhesive failure, where the crack opening of the joint propagated well beyond the actual crush zone of the steel (Figure 5.26). This rapid unzipping of the adhesive joint resembled that of a mode I opening type test, where the initial crushed and folded section of the tube behaved

like a wedge pushing the separated top and bottom hat sections further apart, causing more adhesive failure and extensive fracture of the steel. As the bottom portion of the tube (the end mounted on the wall) buckled outwards, the initial crushed and folded portion was torn off from the rest of the tube, effectively splitting the tube in two lengthwise. On the other hand, even after the DM-AX-FM-GB-03 specimen developed three folds, the crack propagation of the adhesive joint was kept in control (Figure 5.27). The difference in energy absorbed by the test specimens could be explained by the difference in the observed crush response, where the DM-AX-FM-GB-03 specimen absorbed 10% more energy than DM-AX-FM-GB-01, and 27% more than DM-AX-FM-GB-02, at 200 mm of displacement. The failure surface was primarily cohesive and adhesive coverage was good.

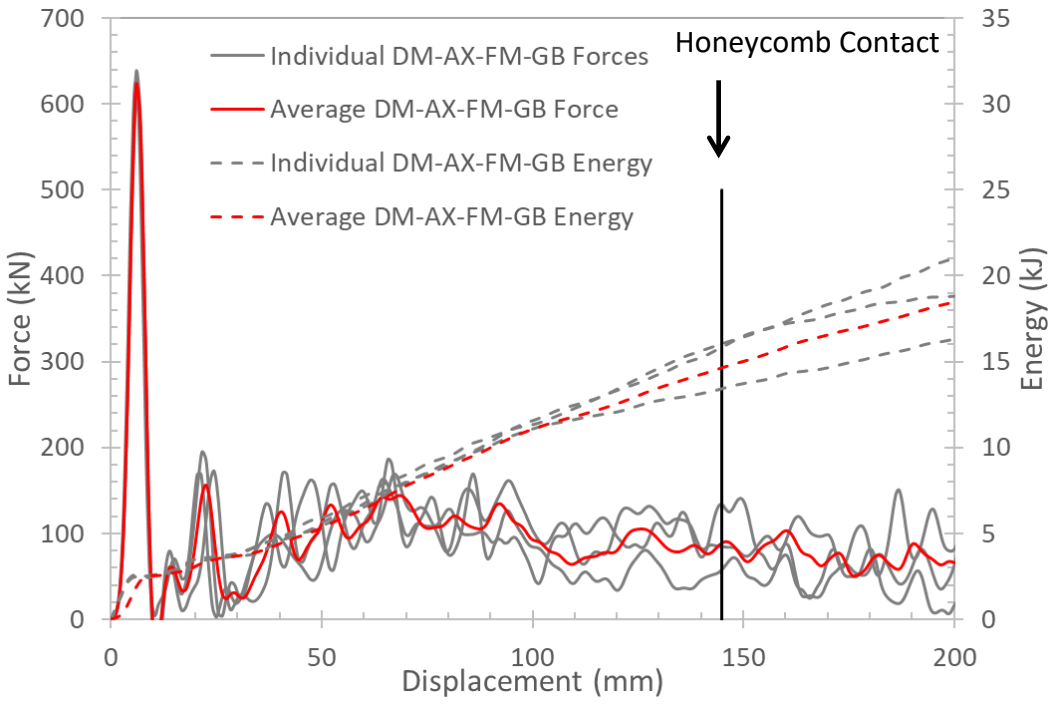

Figure 5.25: DM-AX loading response and energy absorbed by FM specimens

Figure 5.26: Global buckling deformation mode in DM-AX-FM-GB-01, showing fold initiation (left), and rapid crack propagation (center and right)

Figure 5.27: Local folding deformation mode in the DM-AX-FM-GB-03, showing initiation (left), and stable collapse with continual development of folds (center and right)

Three test repeats were conducted for the DM-AX-3Z-GB condition to investigate how a graded soft zone affected the loading response of an adhesively bonded ultra-high strength steel tube.

Figure 5.28 shows the individual and average force and energy against displacement plots for the dynamic three zone experiments. One area of considerable difference between the three zone and fully martensitic hat sections was the extent of warpage, specifically that the three zone hats had a larger gap a third of the way from the heated end of the hat section lengthwise when laid flat on a surface. This is illustrated in detail in Section 3.2. During the bonding process where flanges were clamped down, the larger gap inadvertently introduced a higher amount of residual stresses in the metal and higher pre-tension on the adhesive joint compared to the fully martensitic tubes. The main concern with the residual stresses and pre-tension was that the deformation mode would favor a global buckling response due to an earlier than expected adhesive joint failure. This was observed with the DM-AX-3Z-GB-01 test, (Figure 5.29). It can be seen that immediately upon impact (at 1 ms), the flange area, where the large gap was, experienced extensive adhesive failure that rapidly propagated along the entire length of the joint. Although a fold was initiated, the pre-mature joint failure initiated a global buckling deformation mode that drove the top and bottom hat sections away from the centre axis. In contrast, DM-AX-3Z-GB-02 and DM-AX-3Z-GB-03 tests managed to trigger a folding deformation pattern that was maintained throughout the test, due to the absence of extensive adhesive joint failure (Figure 5.30). The failure surface was primarily cohesive and adhesive coverage was good.

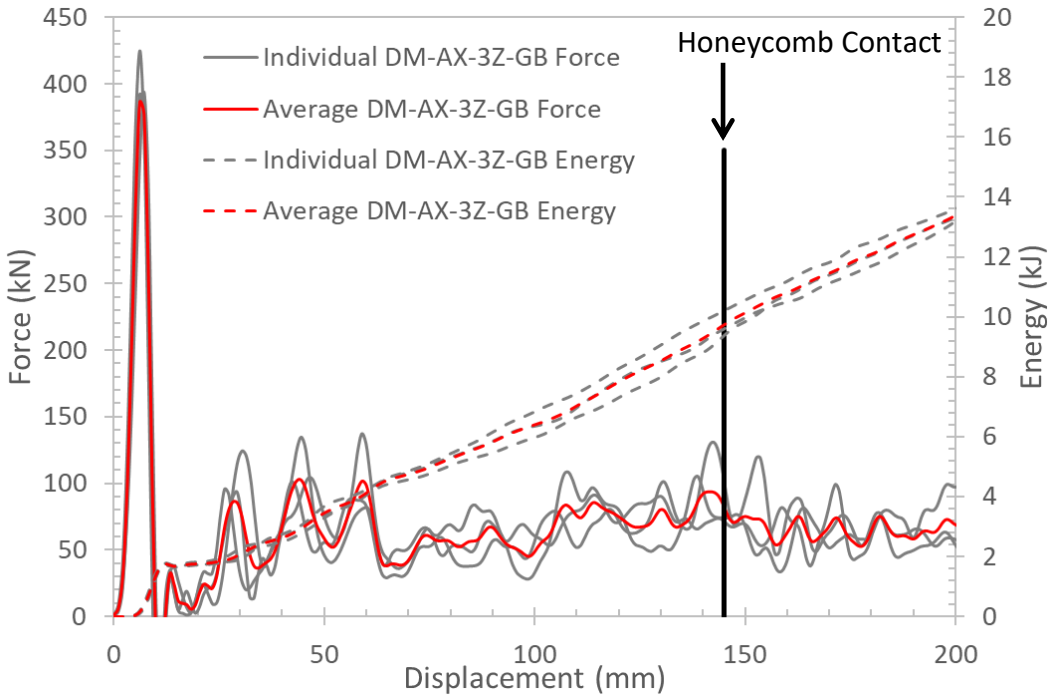

Figure 5.28: Loading response and energy absorbed by DM-AX-3Z-GB specimens

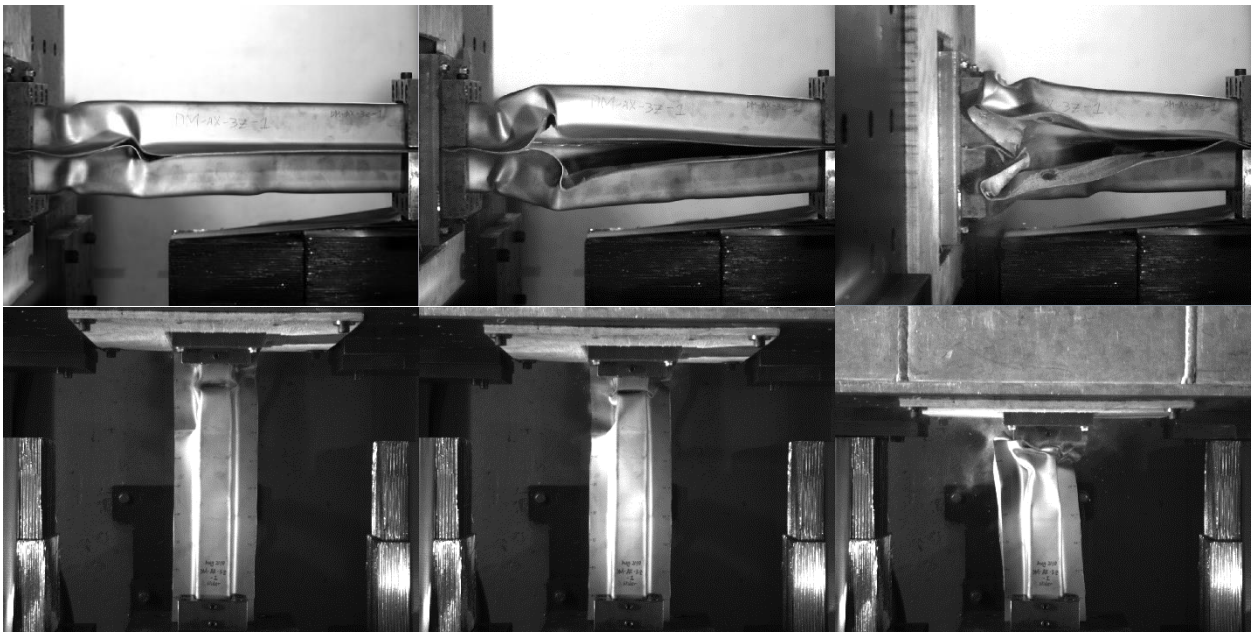

Figure 5.29: Global deformation in DM-AX-3Z-GB-01, showing initiation at the point of highest residual stress (left), and rapid crack propagation and flange separation (center and right)

Figure 5.30: Stable and controlled collapse in DM-AX-3Z-GB-03, showing fold initiation at the indent (left), and extensive fold development (center and right)

Comparing the loading response of DM-AX-FM-GB and DM-AX-3Z-GB tests (Figure 5.31), it could be seen that the fully martensitic specimens attained considerably higher peak force and energy absorption. However, the three zone specimens exhibited little to no metal fracture, and the overall deformation pattern was more controlled and consistent; however, extensive cohesive failure was seen in all of the dynamic axial crush specimens.

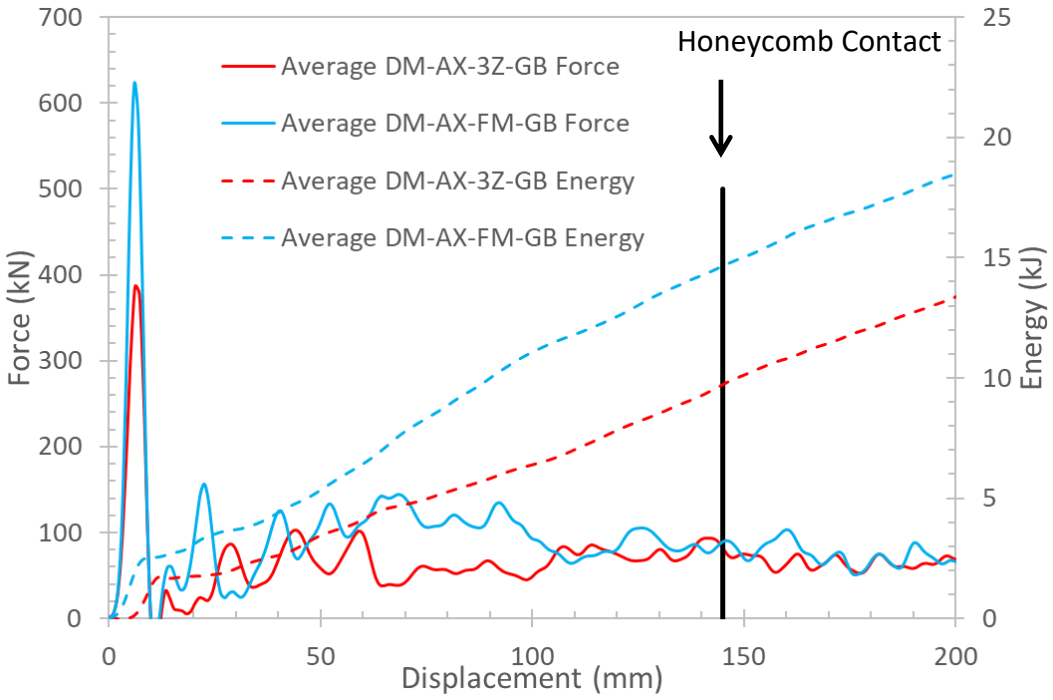

Figure 5.31: Comparison of average force and energy displacement response for DM-AX-FM-GB and DM-AX-3Z-GB experiments

5.3 Caiman Experiments

Three test repeats each were conducted for the 1.2mm QS-CM-FM-GB condition and QS-CM-SF-GB condition. Figure 5.32 below summarizes the individual and average forces for each of the two test conditions, and Figure 5.33 summarizes the individual and average energy absorbed.

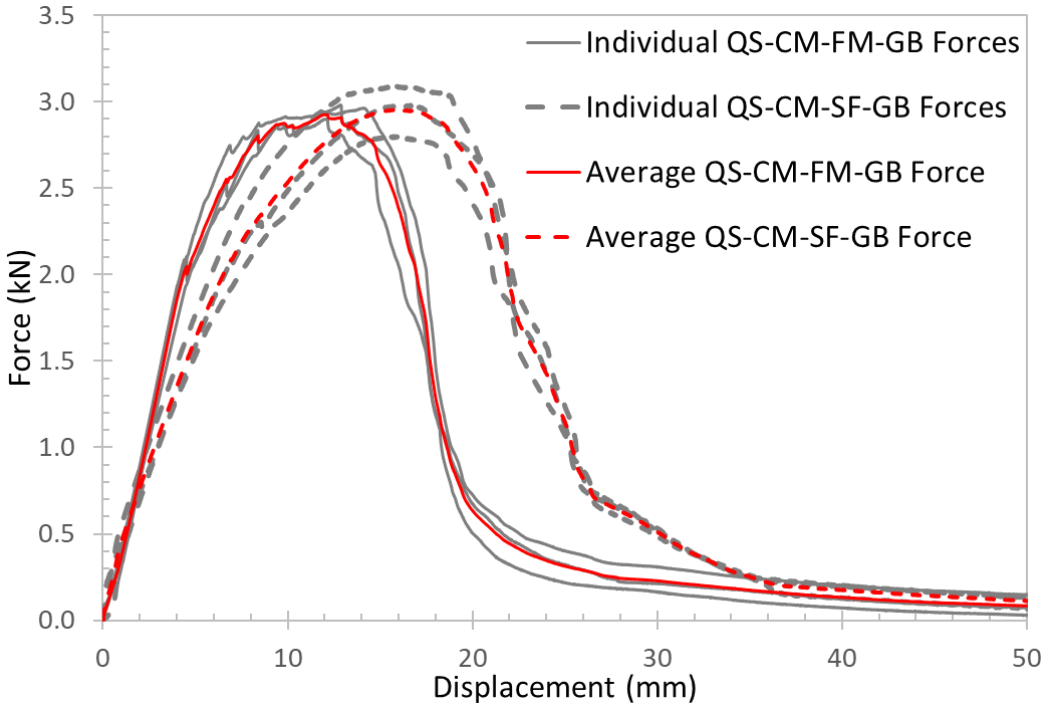

Figure 5.32: Comparison of loading responses of QS-CM-FM-GB and QS-CM-SF-GB specimens

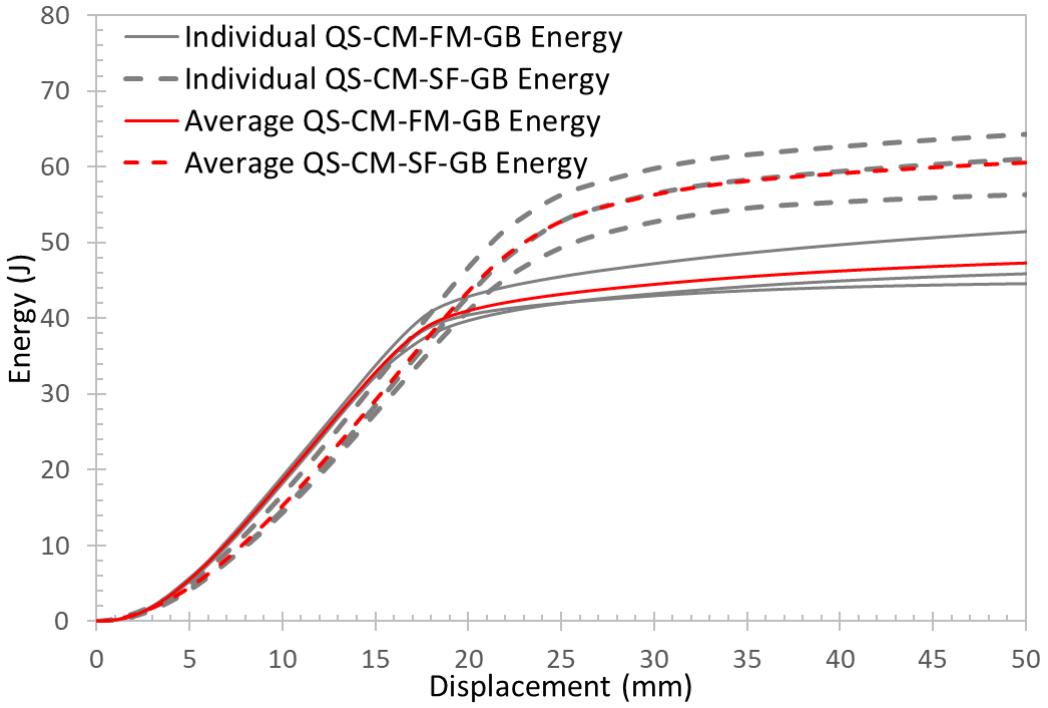

Figure 5.33: Comparison of energy absorbed by QS-CM-FM-GB and QS-CM-SF-GB specimens

Overall, there was no noticeable difference in the progressive adhesive joint failure (Figure 5.34), and the force vs. displacement loading response between fully martensitic and soft flange specimens varied mostly by displacement to peak force. Soft flange tubes reached an average peak force of 3.0 kN at a displacement of 31.7 mm, while the fully martensitic tubes reached an average peak force of 2.9 kN at an earlier displacement of 24.4 mm. For energy vs. displacement response, the soft flange tubes absorbed an energy of 60.5 J at 50 mm of displacement, while the fully martensitic tubes absorbed a lower energy of 47.3 J at the same displacement. Another distinction between the two test conditions was that the force and energy for the fully martensitic samples were somewhat more consistent than the soft flange samples. Upon inspecting the failure surface of the adhesive joints, the cause of the inconsistency in the soft flange samples was thought to be due to observed areas of unbonded adhesive. Due to the warpage of the soft flange hat sections, where the flange and side walls curve inwards toward the middle of the hat section lengthwise, the inside edge of the flange near the center of the hat section will be further away from the steel clamping bars and thus would not be clamped down as much as other areas along the flange. This resulted in some of the adhesive at the inside edge of the bottom flange not being in complete contact with adhesive on the inside edge of the top flange. Therefore, the adhesives simply cured in the oven, without fully mating the top and bottom flanges in those particular areas. These patches of unbonded adhesive can be seen in Figure 5.35 in varying sizes between the different specimens. Note that QS-CM-SF-GB-01 with the smallest unbonded patch corresponded to the highest peak force, while QS-CM-SF-GB-02 with the largest patch corresponded to the lowest peak force. In contrast, a uniform and full coverage of adhesive was observed for all the fully

martensitic samples with cohesive failure (Figure 5.36). The failure surface was cohesive and adhesive coverage was excellent.

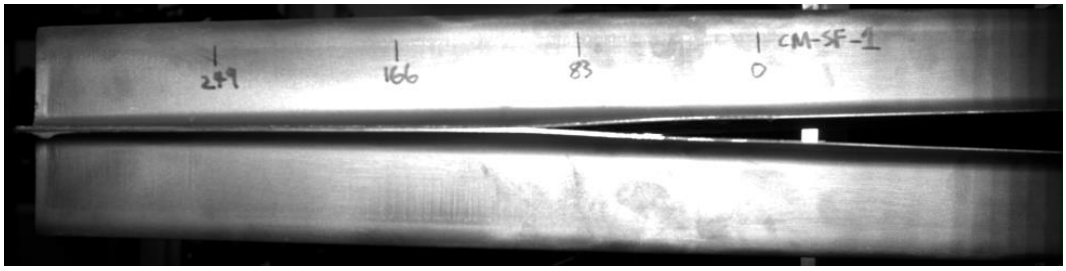

Figure 5.34: Crack propagation and flange separation in the Caiman experiment

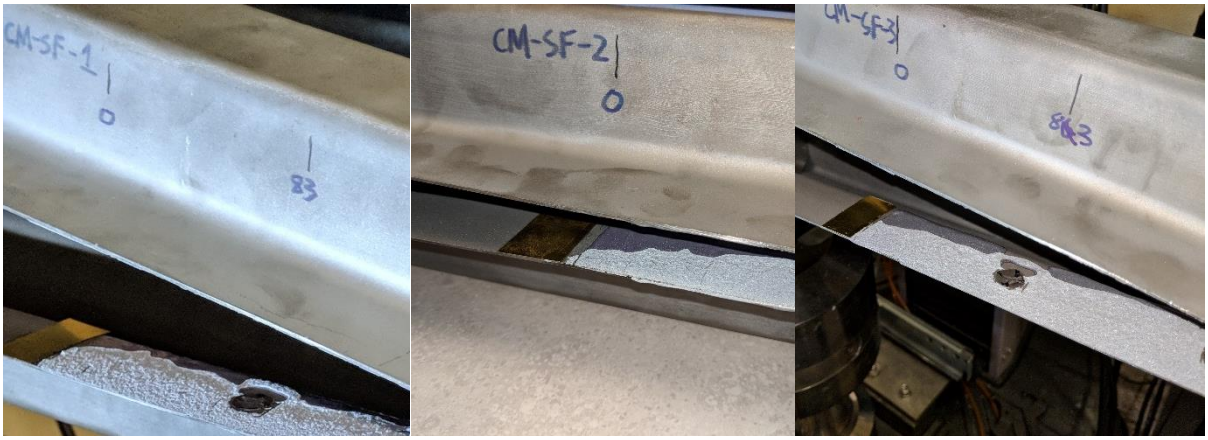

Figure 5.35: Areas of unbonded adhesive due to the curvature of soft flange hat sections, making it difficult to fully clamp down the center along the length of the tube

Figure 5.36: Failure surface of fully martensitic Caiman samples, showing consistent and uniform adhesive coverage

Chapter 6 Numerical Modelling Results and Discussion

6.1 Three Point Bend Numerical Models

6.1.1 Quasi-Static Three-Point Bend Models

The 1.8 mm thick QS-3P-FM-GB experiments all demonstrated a stable symmetric crush mode, where the flanges abruptly separated at the end, which was captured by the numerical model. The predicted response was in good agreement with the experimentally measured response during the initial load up phase (Figure 6.1). Although the model predicted a lower peak force (9.47%) and earlier displacement-to-failure (11.9%), the flanges separated abruptly similar to what was observed in the experiments.

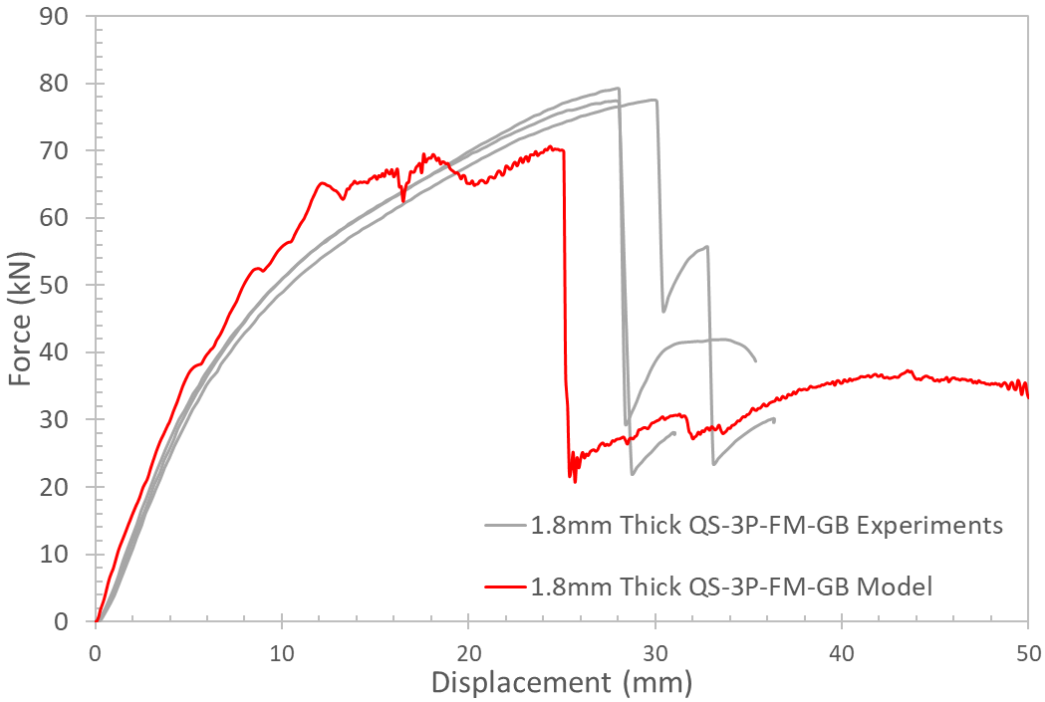

Figure 6.1: Comparison between force-displacement response of 1.8mm thick QS-3P-FM-GB experiments and simulation

The 1.2 mm thick QS-3P-FM-GB numerical model, on the other hand, was only able to capture the loading pattern up to the peak force, but not the abrupt flange separation until much later. Recall that only the QS-3P-FM-GB-01 test experienced a symmetric deformation mode, which was observed in the model was well. However, the adhesive joint in that particular test failed at roughly 30 mm of cross head displacement (Figure 6.2), whereas modeled joint did not fail until about 48 mm of displacement. Recall from Section 4.2 that Considering that none of the 1.8 mm thick tests experienced asymmetric failure and that the adhesive model predicted the joint failure reasonably well in the 1.8 mm thick model, the delayed failure in the 1.2 mm thick model may be attributed to the inherent reduced structural stability associated with the thinner metal adherend, which may have affected the stress distribution within the joint.

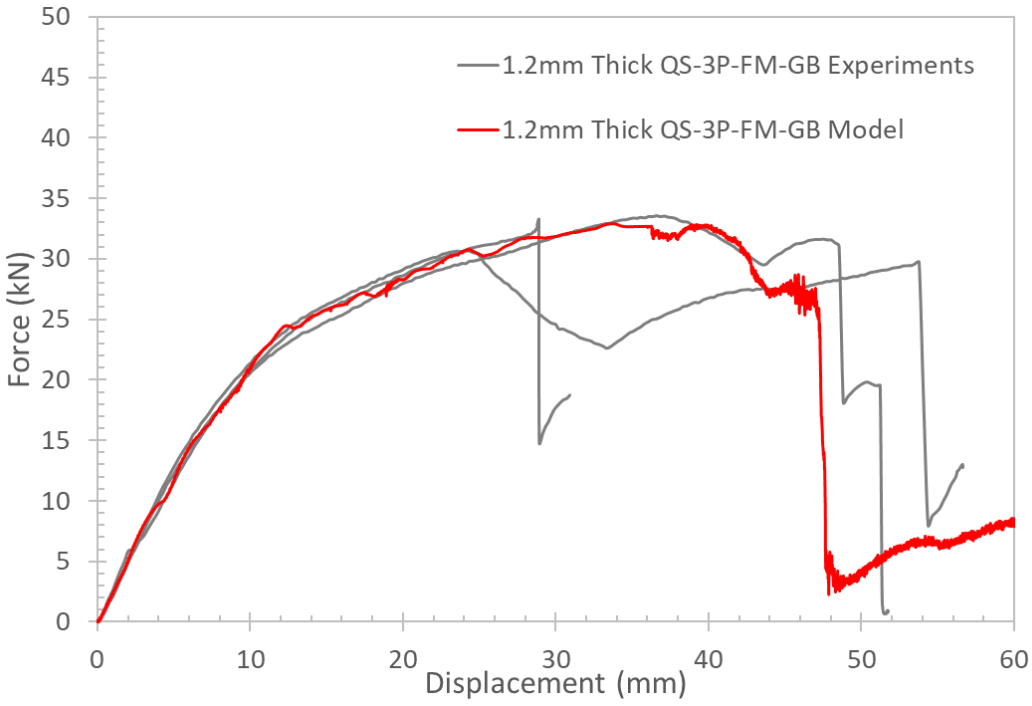

Figure 6.2: Comparison between force-displacement response of 1.2 mm thick QS-3P-FM-GB experiments and simulation

The adhesive joint of the 1.2 mm thick QS-3P-SF-GB experiments all stayed intact, with only minor adhesive failure near the inside edge of the flange on the ends of the tube. This minor adhesive failure was predicted by the numerical model (Figure 6.4), in which the adhesive joint, represented by the single layer black cohesive elements, had eroded near the inside edge of the flange. The predicted force-displacement response also correlated well with the experimental results in the load up, peak force, and post peak (Figure 6.3).

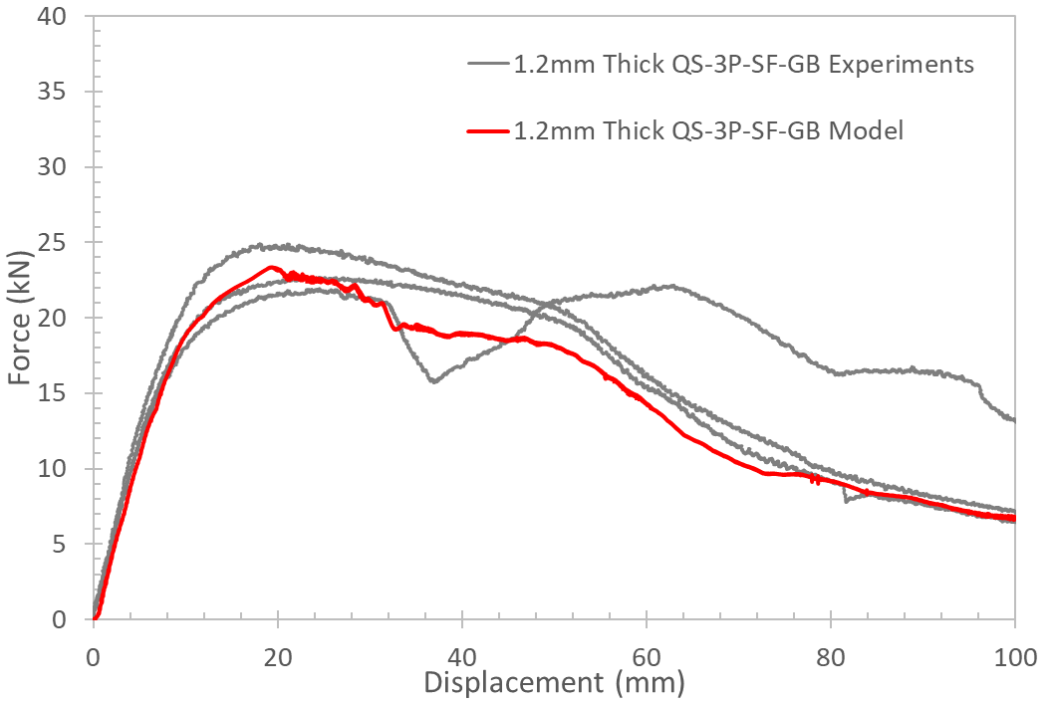

Figure 6.3: Comparison between force-displacement response of 1.2 mm thick QS-3P-SF-GB experiments and simulation

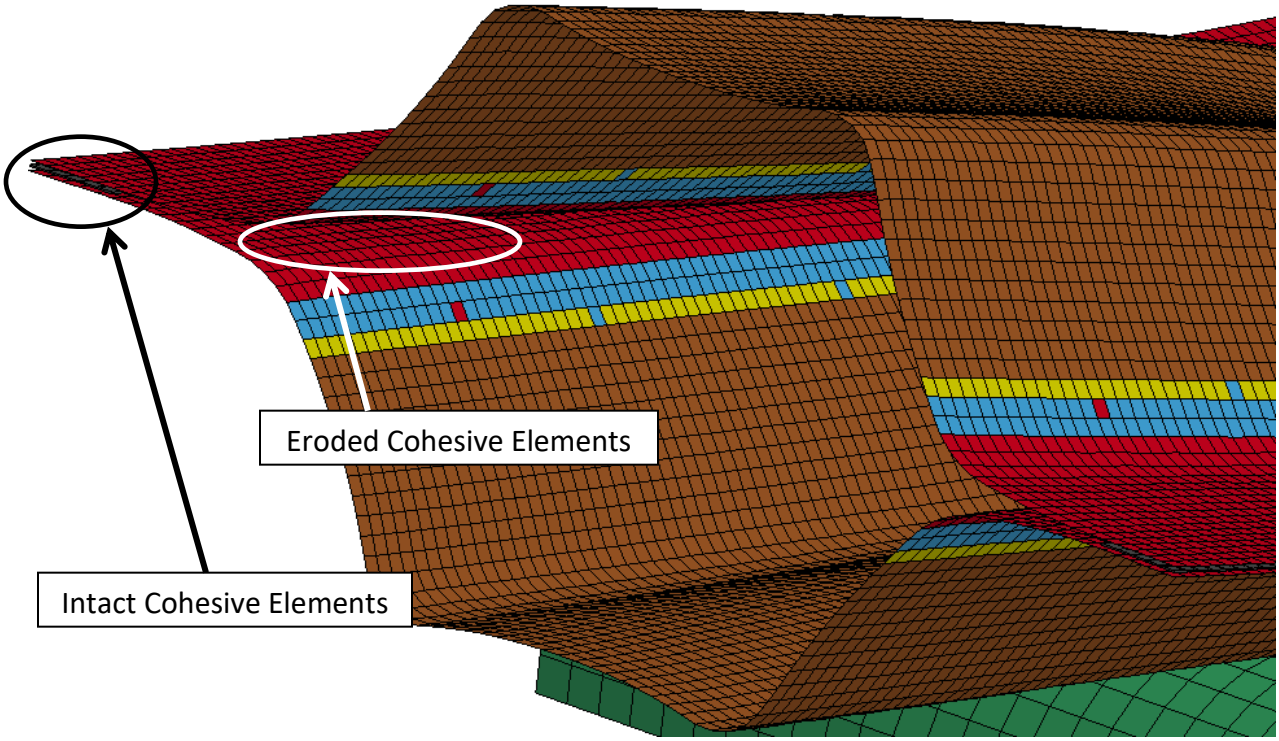

Figure 6.4: QS-3P-SF-GB simulation, showing the area where adhesive failure is predicted at the inner edge of the flange at the ends of the tube

Overall, for the quasi-static three-point bend models, the challenge for the adhesive model was in predicting the displacement-to-failure of the adhesive joint. Even with the height of the fully martensitic tubes increased to match the experimentally measured dimension, the displacement-to-failure was only reduced by 2 mm (an improvement of roughly 4%). While the predicted displacement-to-failure for the 1.8 mm thick model was 11.9% more than the experiments, this metric could not be used to assess the 1.2 mm thick model since those experiments had different modes of deformation (fully martensitic) or no failure at all (soft flange). Similarly, the different modes of deformation made it unsuitable to compare the energy absorption. Therefore, only the peak force of the model was validated against the

experimentally measured values for 1.2 mm thick QS-3P-FM-GB and 1.2 mm thick QS-3P-SF-GB tests (Figure 6.5).

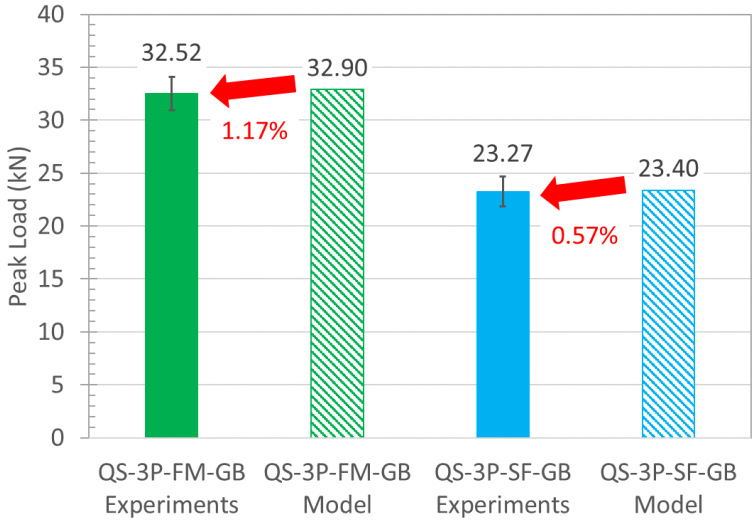

Figure 6.5: Comparison of peak forces of 1.2 mm thick QS-3P-FM-GB and 1.2 mm thick QS-3P-SF-GB experiments *vs.* their respective models

6.1.2 Dynamic Three-Point Bend Models

Figure 6.6 shows the loading response and energy absorbed by DM-3P-FM-GB specimens. Note again that wooden inserts were used only in this particular configuration of three-point bend test, and was modeled as a deformable solid with elastic material properties and generic mechanical properties of soft woods (Table 4.2, Section 4.5). The numerical model predicted flange separation at 39 mm of sled displacement, which was earlier than what was observed in the experiment, occurring when the sled came into contact with the honeycomb packs (Figure 6.7). The model correlated well with the experiment during the initial loading but under-predicted the peak force (10.8%), and as a result, the energy absorption was also under-predicted (15.9%).

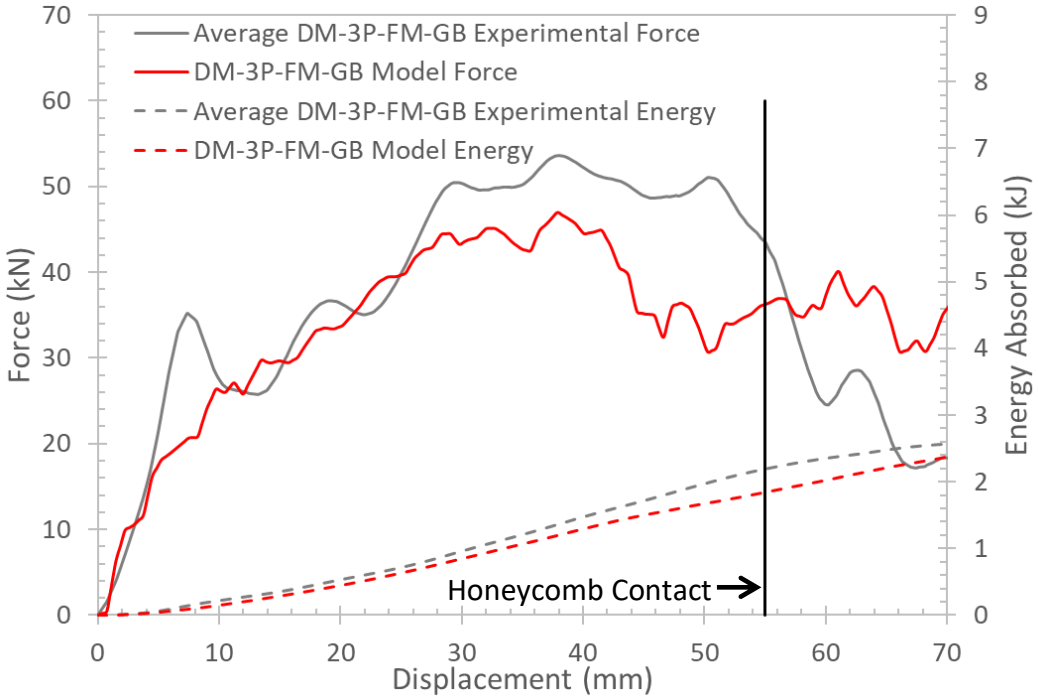

Figure 6.6: Average force and energy-displacement response of DM-3P-FM-GB experiment *vs.* simulation

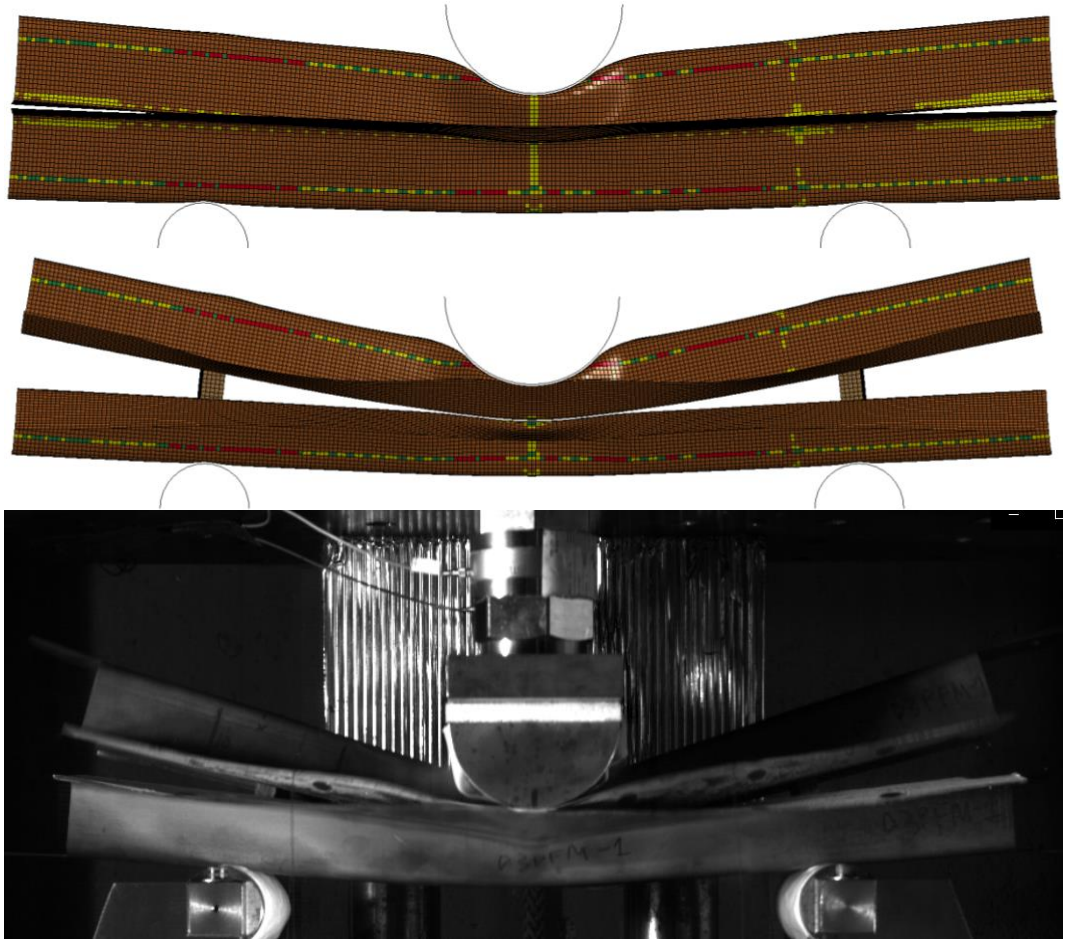

Figure 6.7: DM-3P-FM-GB experiment *vs.* simulation, in which early flange separation was predicted by the model (top), and comparison at the same indentor displacement between the model (middle) and the experiment (bottom)

The loading response and energy absorbed by the DM-3P-SF-GB specimen is shown in Figure 6.8. Note again that the experimental force was averaged between DM-3P-SF-GB-02 and DM-3P-SF-GB-03 only, as both of the load cell channels malfunctioned during the DM-3P-SF-GB-01 test, and that these two test plots were obtained by doubling the measured forces of the sole functioning load cell channel. Similar to what was observed in the experiment, the model predicted that most of the flange would stay intact and that only a small degree of joint failure would be observed on the inner edge of the flange at the ends of the tube. The measured force

was in reasonable agreement (16.0%) while the energy absorbed correlated well with the experiments (2.95%).

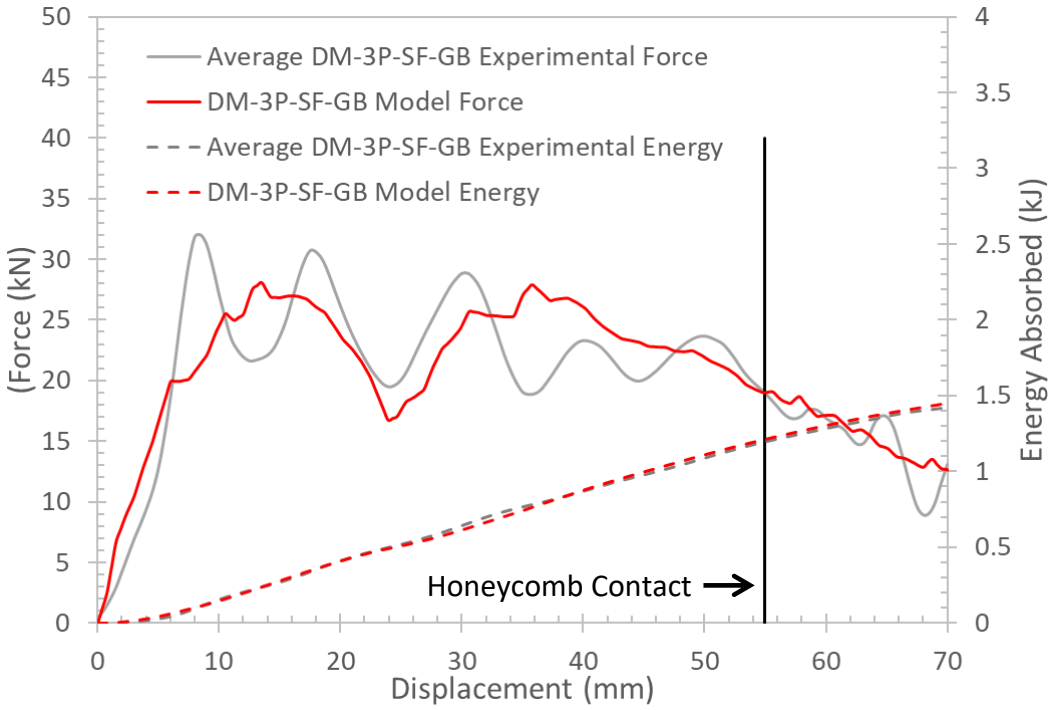

Figure 6.8: Average force and energy-displacement response of DM-3P-SF-GB experiments *vs.* simulation

Contrary to the 1.2 mm thick QS-3P-FM-GB simulation, the DM-3P-FM-GB simulation predicted an earlier displacement-to-failure compared to the experiments. The average displacement-to-failure over three DM-3P-FM-GB tests was 50.0 mm (standard deviation 3.43 mm), which was 22.1% more than the value predicted by the model. This was likely due to incorrect dimensions of the wooden insert models, since they were crudely cut from a piece of plywood to roughly fit inside the tube, which is a limitation of the current study. Overall, the predicted deformation pattern for both the DM-3P-FM-GB and the DM-3P-SF-GB tests were in good agreement with the experiments, and the loading response correlated reasonably well (Figure 6.9).

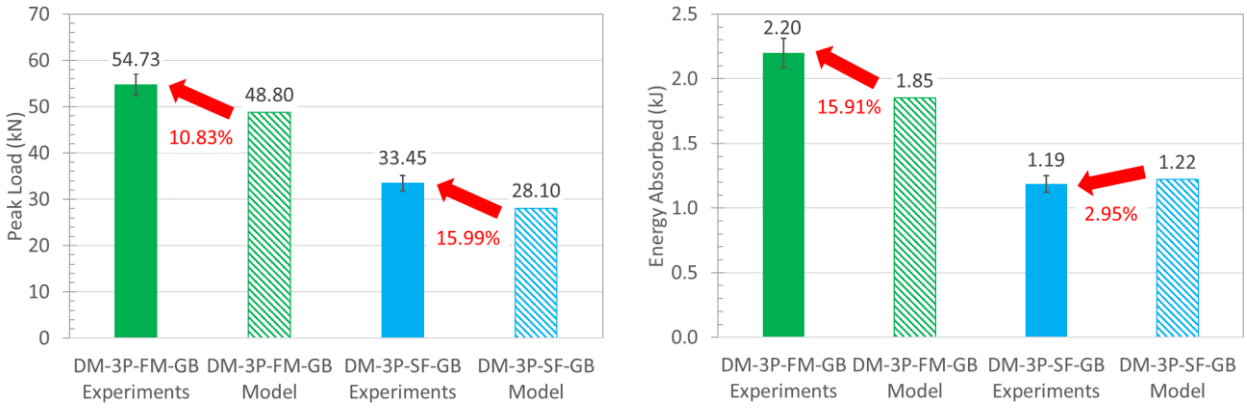

Figure 6.9: Comparison of peak forces (left) and energy absorptions (right) of DM-3P-FM-GB and DM-3P-SF-GB experiments *vs.* their respective models

6.2 Axial Crush Numerical Models

6.2.1 Quasi-Static Axial Crush Models

The predicted loading response and energy absorbed by the QS-AX-FM-GB specimens is shown in Figure 6.10. At 300 kN, the predicted peak force was greater than the measured peak force, and the model also predicted a stiffer response, that could be attributed to the build up of compliance in the equipment during testing. Based on the experimental peak force, displacement-to-peak force, and approximate cross sectional area of the tube, the Young's Modulus was calculated to be lower than that of steel (200 GPa), and approximately 3 mm of total compliance was present in the equipment. An asymmetric fold developed roughly a third of the way up from the bottom of the tube (Figure 6.11), whereas two tubes experienced global buckling deformation, and one tube experienced folding that initiated from the dimple. Extensive adhesive joint failure due to rapid crack propagation was predicted by the model and was also observed in the experiments.

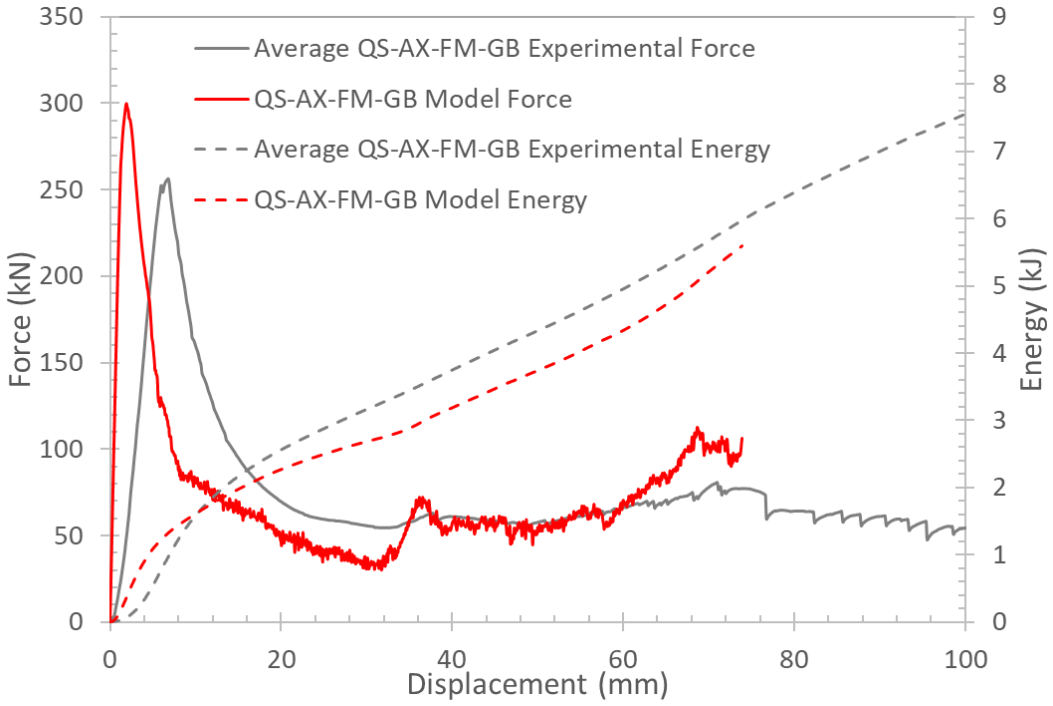

Figure 6.10: Average force and energy displacement response of QS-AX-FM-GB experiments *vs.* simulation

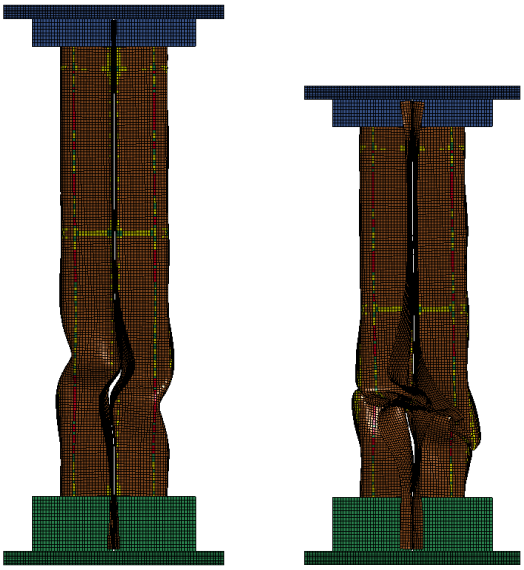

Figure 6.11: QS-AX-FM-GB model deformation, showing the development of an asymmetric fold away from the initiator (left) and the extensive base metal fracture as the experiment progressed (right)

The predicted loading response and energy absorbed by the QS-AX-3Z-GB specimens is shown in Figure 6.12 below. The peak force was noticeably over predicted but the overall predicted energy absorption was similar over 100 mm of displacement. The stiffer loading response predicted by the model could likely be accounted for by the fact that the experimental measurements are subjected to compliance in the machinery. Visually, the deformation was initiated by an asymmetric fold, where the dimple is folded in on one side, but the fold on the other side was offset vertically, as seen in Figure 6.14. Also, as the simulation progressed extensive adhesive failure was predicted, and the deformation shifts towards global buckling. This did not match symmetric folding deformation observed in the experiments, and it was suspected that it could be due to the hardness mapping of the model did not correspond to the physical sample's distribution. Therefore, another model was made with a revised mapping of bins along the tube, in which the material properties of each bin was unchanged, that matched the physically measured hardness data as much as possible (detailed in Section 4.1). Shown in Figure 6.14, the revised mapping sorted all elements in the top 125 mm of the tube into bin one (red elements, softest), followed by a "transition bin" with new material properties that were interpolated between bins one and two that covered the next 50 mm of the tube, followed by bin two for all elements in the next 100 mm, and the rest of the tube was unchanged. The idea was to ensure the top portion of the tube (near the fold initiator) matches the measured physical hardness distribution as closely as possible, while minimizing numerical artifacts such as a sharp transition from bin one directly to bin two, hence introducing an intermediate bin. The resulting peak force from the new model now correlates better with the experiment, but slightly more energy was absorbed (Figure 6.13). This was likely due to the proper symmetric

fold initiation predicted by the new model, in which the adhesive failure and flange separation was kept well under control throughout the simulation, thus leading to higher energy absorption.

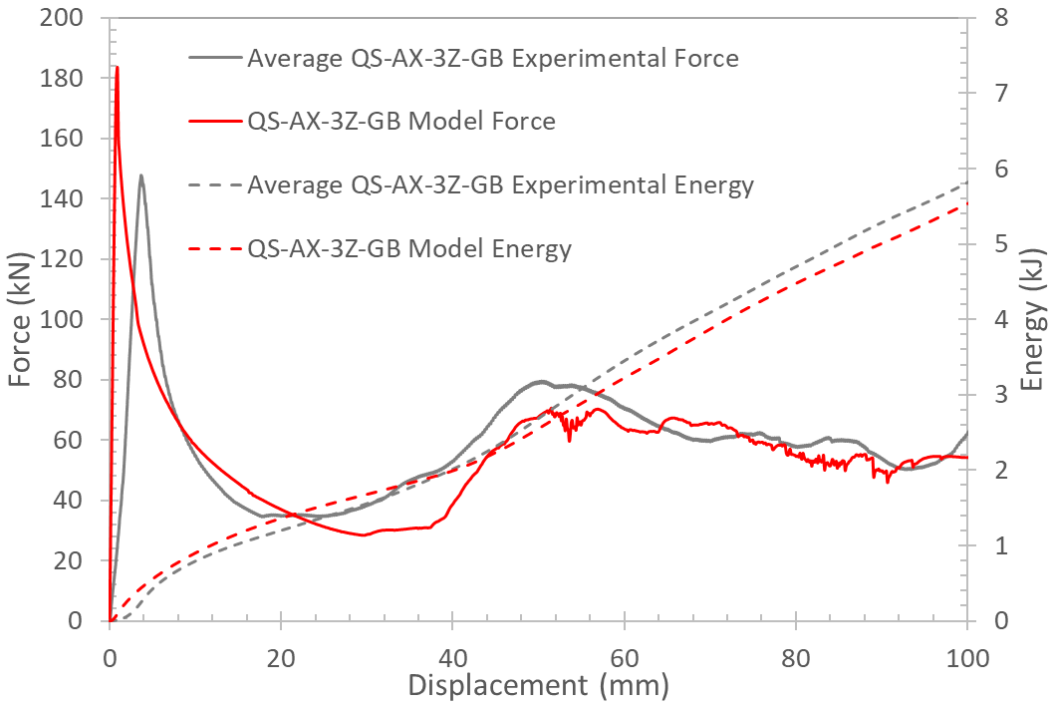

Figure 6.12: Average force and energy displacement response of QS-AX-3Z-GB experiments *vs.* simulation (Omer's (2014) predicted hardness distribution)

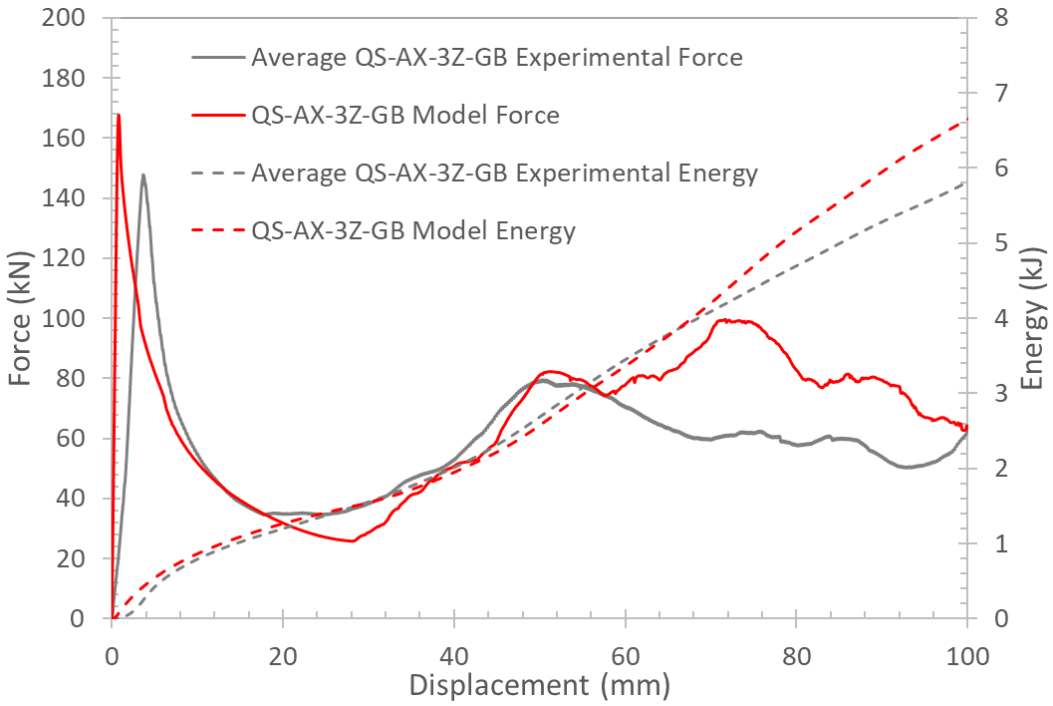

Figure 6.13: Average force and energy displacement response of QS-AX-3Z-GB experiments vs. simulation (Remapped zones corresponding to physical hardness distribution)

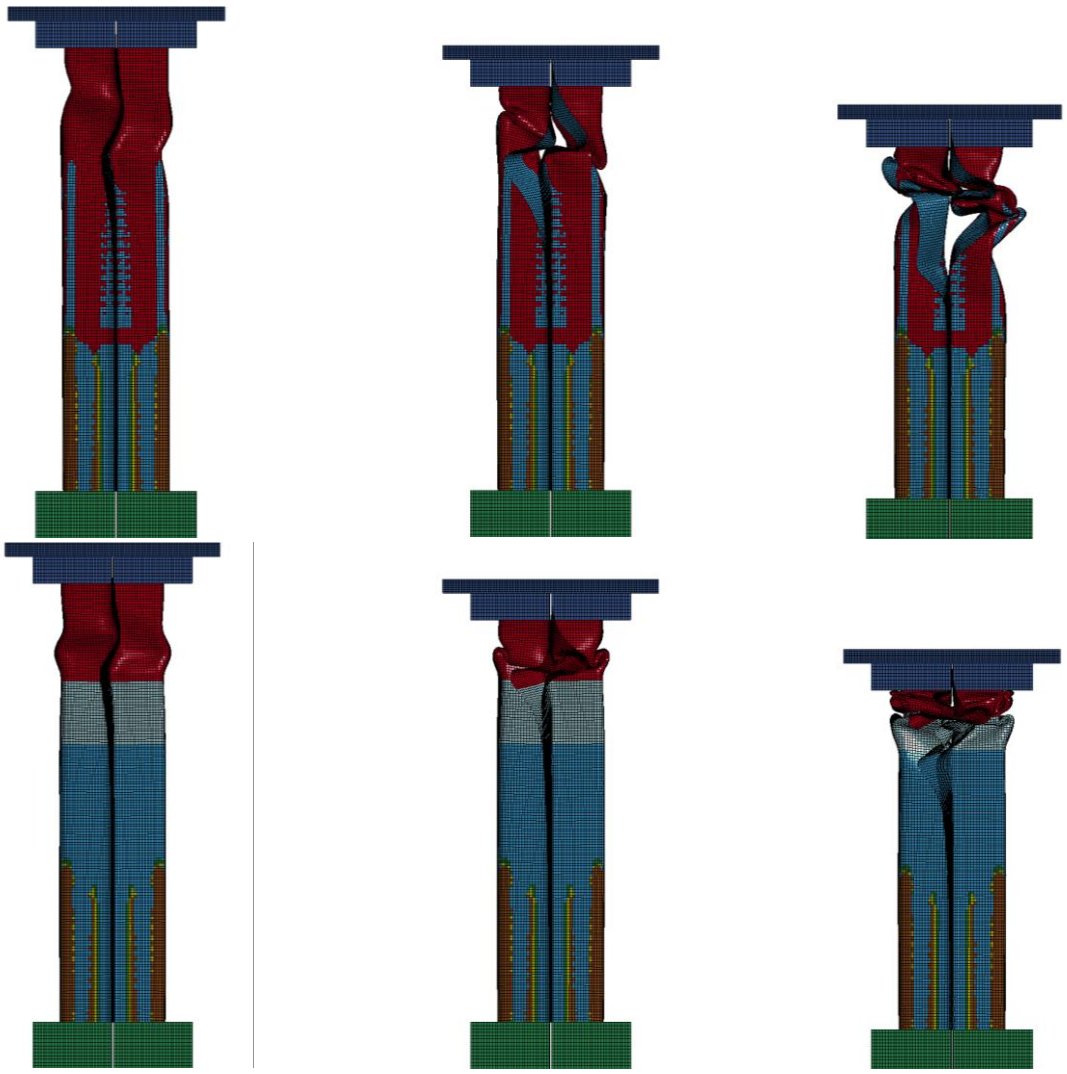

Figure 6.14: Deformation mode of QS-AX-3Z-GB model with Omer's (2014) predicted hardness (top row) and that of manually assigned hardness mapping corresponding to the measured values in the current work (bottom row), showing much improved folding pattern

Overall, the predicted peak force and energy absorbed by the QS-AX-FM-GB and QS-AX-3Z-GB tests were in reasonable agreement with the experiments (Figure 6.15). The predicted deformation pattern of the QS-AX-FM-GB test differed from what was observed in the experiments, in that no physical specimens initiated deformation from the bottom portion of the tube. The exact cause of the predicted deformation was unknown. On the other hand, the

predicted deformation of the QS-AX-3Z-GB tests was in better agreement with the experiments once the tubes were manually assigned a hardness mapping representative of the hardness measurements collected in this work. In addition, the new hardness mapping reduced the predicted peak force, improving the percentage difference between the model and the experiment from 23.5% to 12.9%.

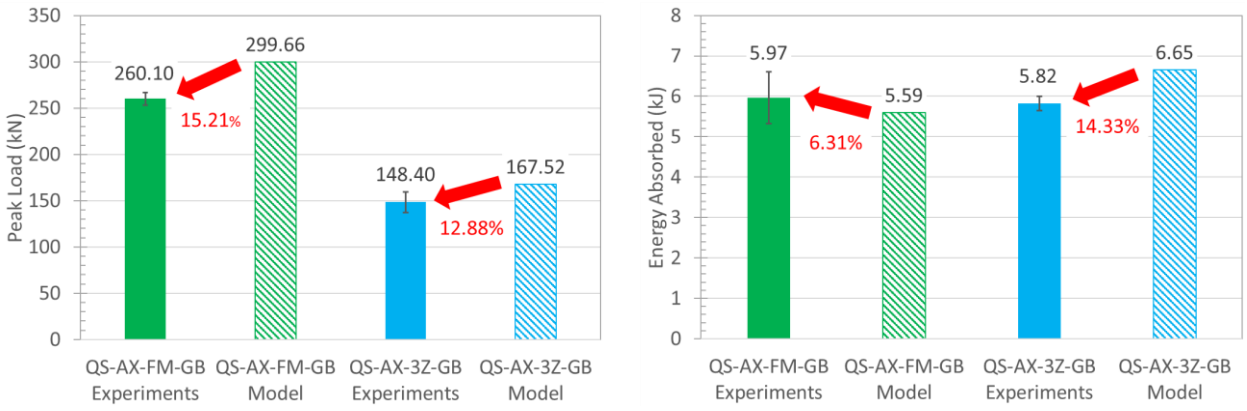

Figure 6.15: Comparison of peak forces (left) and energy absorptions (right) of QS-AX-FM-GB and QS-AX-SF-GB experiments *vs.* their respective models

As outlined in Section 4.3, selective mass scaling with a minimum time step of $1x10^{-5}$ s was used in all quasi-static simulations in order to keep the simulation time to within about 40 hours, Figure 6.16 demonstrates that this scaling had very little effect on the loading response of the quasi-static three zone axial crush models as an example.

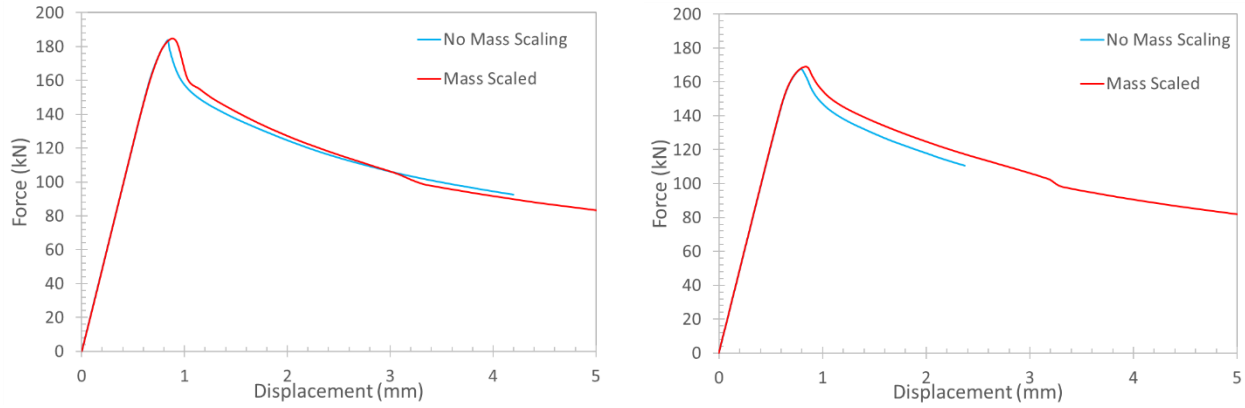

Figure 6.16: Loading response up to shortly after post peak force of Omer's (2014) predicted hardness distribution model (left) and revised physical hardness distribution model (right) for the quasi-static three zone simulations

6.2.2 Dynamic Axial Crush Models

The loading response and energy absorbed by the DM-AX-FM-GB specimens is shown in Figure 6.17. The predicted peak force, at roughly 520 kN, was lower than the measured peak force, at roughly 600 kN, however the initial loading and subsequent rapid reduction in force was well captured by the model. The predicted energy absorption also correlated well with the experiments, coming in at about 14.1 kJ compared to the measured value of 14.8 kJ upon honeycomb contact. However, all three tests demonstrated an initial folding deformation at the indent, while the model predicted a folding deformation half way along the tube, where the joint failed and the flange separated (Figure 6.18). As the first fold collapsed, the adhesive joint failure rapidly propagated further along the tube, and the fully martensitic steel experienced extensive fracture along the fold, effectively shearing the tube into two halves and the top half started to slide over the bottom half. The inability of the steel model to capture the folding initiation at the indent may be due to the omission of work hardening and plastic deformation effects, since the indent was made by simply displacing the nodes.

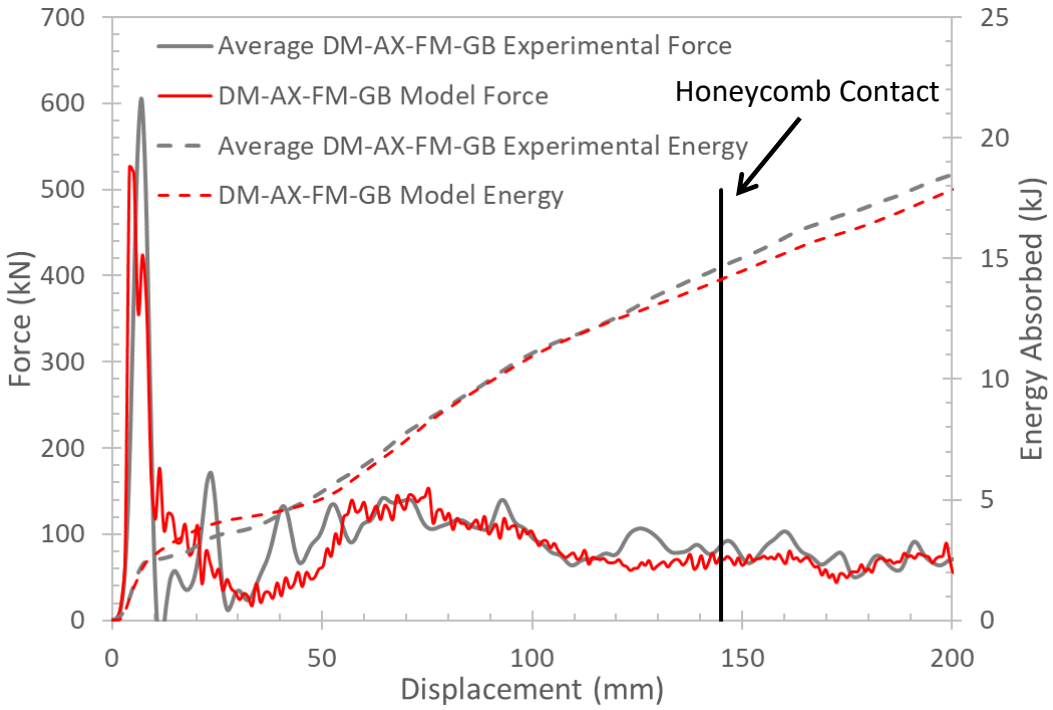

Figure 6.17: Average force and energy-displacement response of DM-AX-FM-GB experiments *vs.* simulation

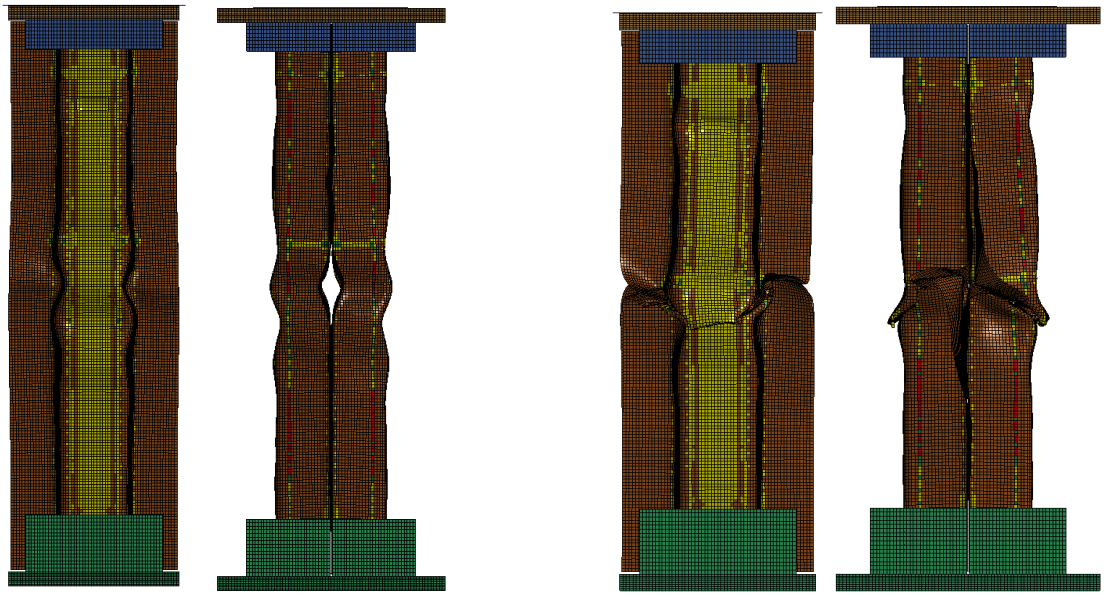

Figure 6.18: DM-AX-FM-GB model, showing adhesive failure initiation at the center of the tube (left) and extensive metal fracture due to global buckling deformation (right)

The loading response and energy absorbed by the DM-AX-3Z-GB specimen is shown in Figure 6.19. The predicted peak force correlates well with the measured peak force. However, a smaller initial peak is predicted and is shown to have a higher stiffness than what was measured in the experiment. Following the peak, the numerical model exhibited a high degree of noise and oscillation in the force displacement response, which was likely due to the complex continuous folding pattern of the tube causing issues with the contact algorithm. This noise led to a considerably higher predicted energy absorption compared to the experimentally measured value. While the indents successfully triggered a local folding deformation pattern, the crack propagated away from the crush zone much more rapidly than what was observed in the experiment (Figure 6.20). This rapid propagation impeded the flange from folding and interlocking as the crush zone proceeded along the tube, but did not prevent the other areas of the tube to develop folds. For comparison, the tube model with a 50 mm transition zone was also simulated under the same conditions, which demonstrated a deformation pattern that matched the experiments much more closely, where the crack propagation and flange separation were kept well under control.

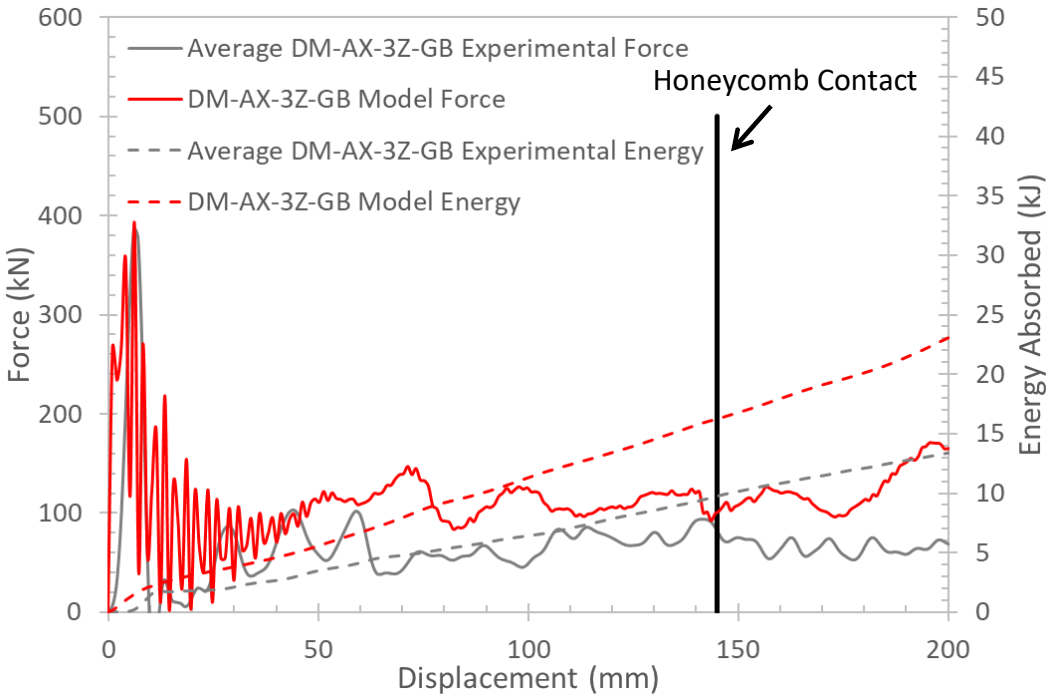

Figure 6.19: Average force and energy-displacement response of DM-AX-3Z-GB experiments *vs.* simulation

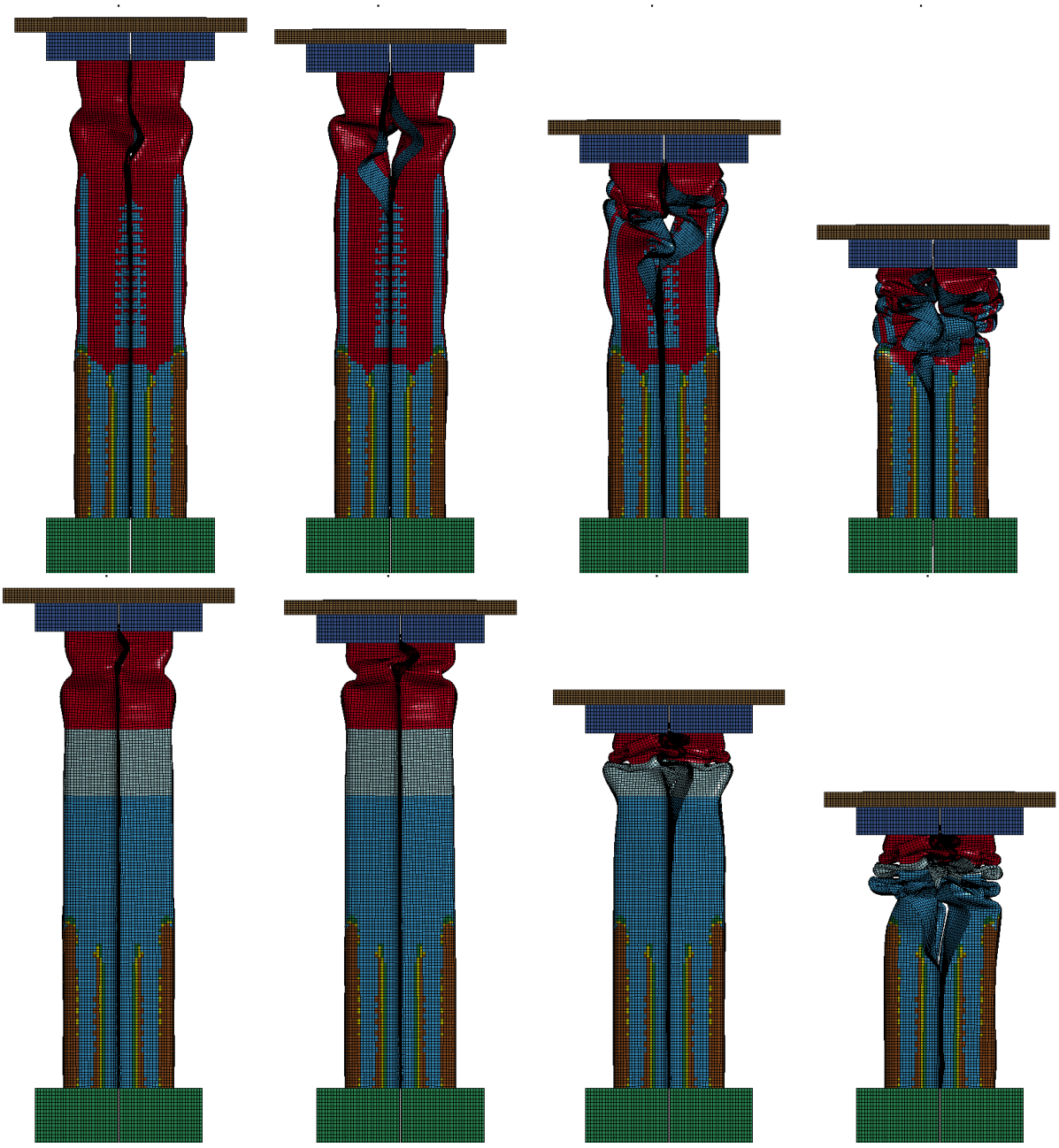

Figure 6.20: DM-AX-3Z-GB model Deformation mode with Omer's (2014) predicted hardness (top row) and that of manually assigned hardness mapping corresponding to the measured values in the current work (middle row), showing a deformation pattern that correlates much better with the experiment (bottom row)

Overall, the predicted peak forces and energy absorption of the DM-AX-FM-GB and the DM-AX-3Z-GB models were in good agreement with the experiments (Figure 6.21). The exception was the predicted energy absorption of the DM-AX-3Z-GB model, which was 66.9% higher than the measured value. The large difference was a result of the excessive oscillation (noise) in the predicted force-displacement response, which was likely caused by contact algorithm issues as a result of a tight continuous folding deformation pattern. As such, the predicted deformation pattern of the DM-AX-3Z-GB model with re-mapped hardness profile correlated well with the

experiments. However, the DM-AX-FM-GB model could not predict the deformation pattern observed in the experiments, in which deformation was initiated at the fold initiator, and was likely due to the lack of inclusion of forming history when the initiator was created.

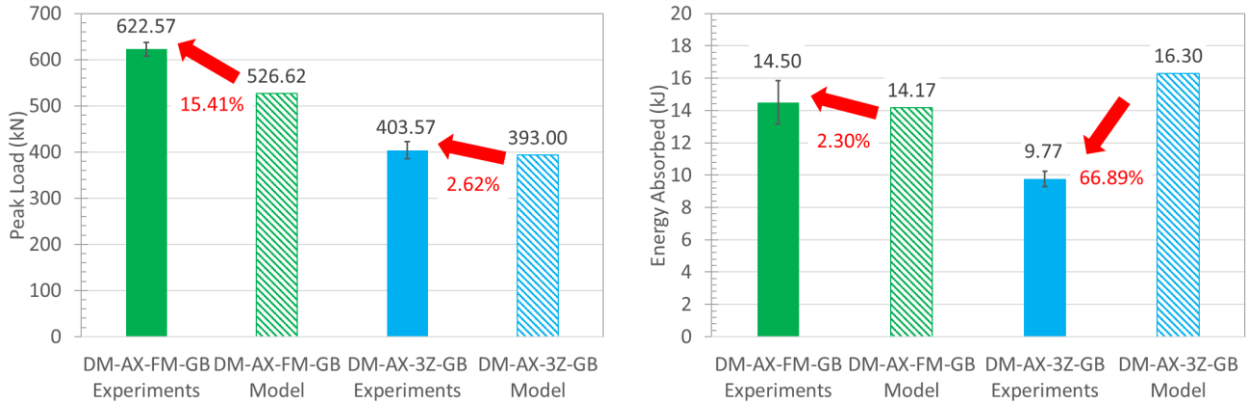

Figure 6.21: Comparison of peak forces (left) and energy absorptions (right) of DM-AX-FM-GB and DM-AX-SF-GB experiments *vs.* their respective models

6.3 Caiman Numerical Models

The loading response comparison between the experiment and the numerical model is shown in Figure 6.22 for QS-CM-FM-GB tests, and in Figure 6.23 for QS-CM-SF-GB tests. The fully martensitic model was able to accurately predict the response from the initial loading and up to the peak force, but experienced a reduction in force slightly earlier and also more gradually than the experiment. The soft flange model predicted a stiffer response during the initial loading but reached a similar peak force, and it also unloaded more gradually compared to the experiment. These small discrepancies in the loading response may be attributed to the inability of the steel material model to accurately capture the elastic deformation behavior of the tube, especially with a complex geometry such as the soft flange tube due to warpage, and not necessarily due to the adhesive model.

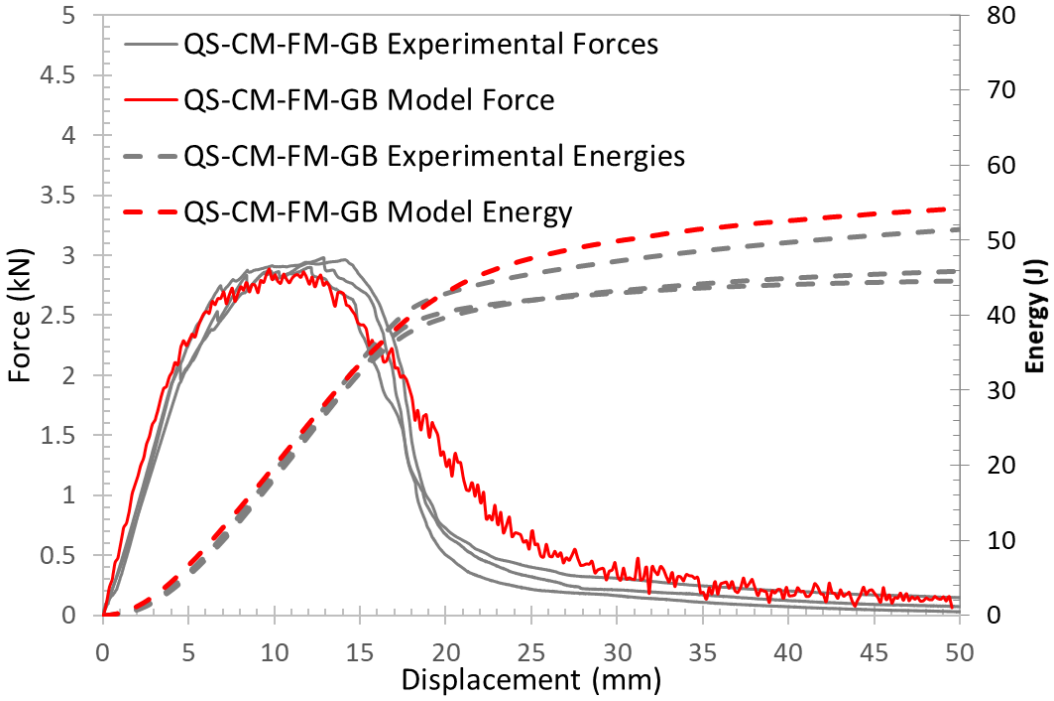

Figure 6.22: Average force-displacement response of QS-CM-FM-GB experiments *vs.* simulation

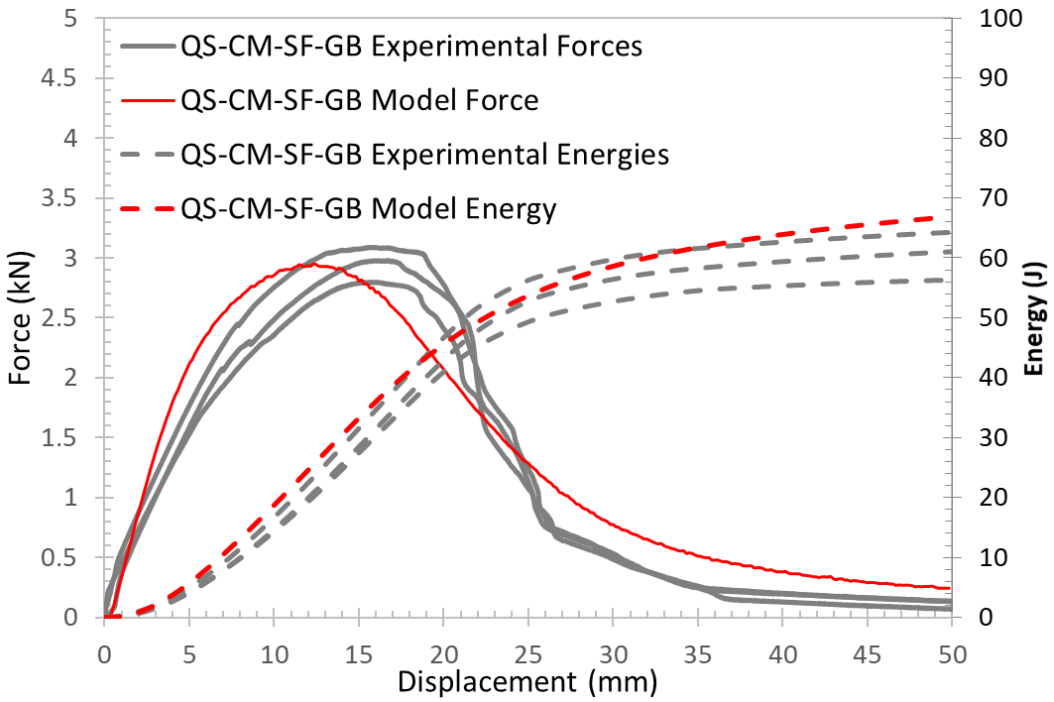

Figure 6.23: Average force-displacement response of QS-CM-SF-GB experiments *vs.* simulation

To further validate the adhesive material model, a local metric can be used to assess the cohesive model in its ability to predict the joint behavior more directly. The first local metric selected was tracking the crack propagation, or the unzipping of the adhesive joint along the bond line, and plotting it against the pin displacement (MTS crosshead displacement). This was done by importing the experimental test videos and the simulation videos generated by LS-DYNA into a free desktop application called Tracker, and following the location of the crack tip after each video frame as it travels along the tube. Figure 6.24 shows an example of an experimental test video being tracked, where the red and pink dots represent the crack tip opening and the bright blue dots represent the crack propagation. Length calibration was done by assigning the length of the bond line to the corresponding length in the video. Note that the pin displacement was obtained from video synced MTS data, not from tracking. The results of tracking the martensitic and soft flange experiments and simulation are shown in Figure 6.25.

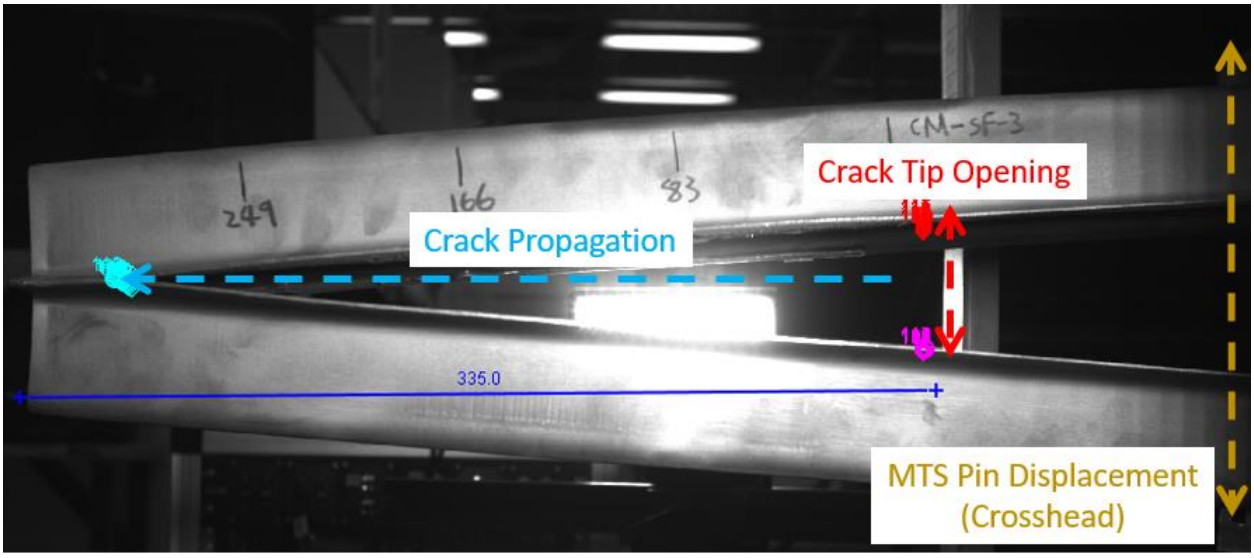

Figure 6.24: Example of a tracked Caiman experiment footage, showing the distance corresponding to crack propagation, crack tip opening, and MTS pin displacement

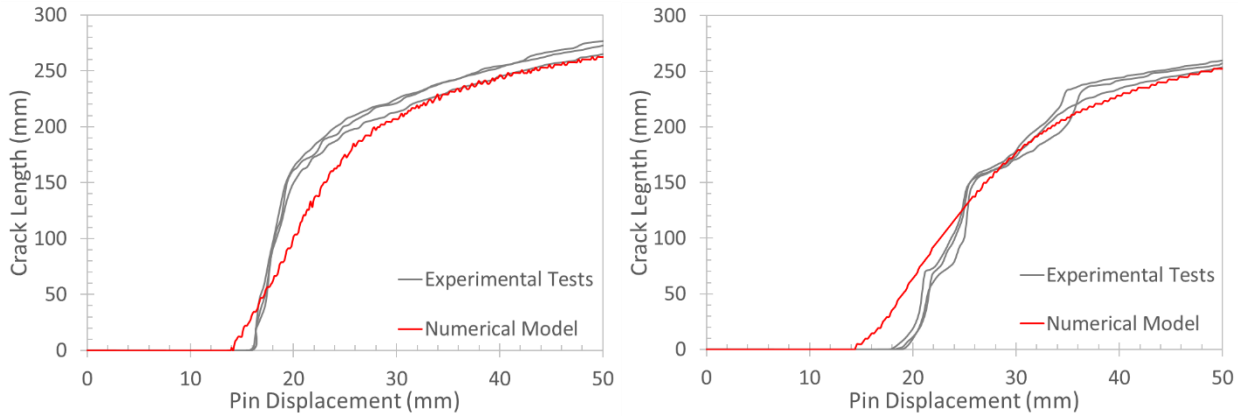

Figure 6.25: Crack length *vs.* pin displacement response for fully martensitic and soft flange Caiman tests, showing the common theme of earlier predicted crack initiation and less rapid propagation

It could be seen that the fully martensitic model predicted the crack propagating roughly 2 mm of pin displacement earlier than what was observed in the experiments, which demonstrated consistent results over three tests. Once the propagation began, the adhesive joint elements also failed more gradually than the experiments, but eventually leveling out after about 25 mm of pin displacement to match the rate of propagation in the experiments. Similarly, the soft flange model predicted propagation starting at the same pin displacement as the fully martensitic model, but was even more gradual than the fully martensitic model. The crack propagation in soft flange experiments started at roughly 18 mm of pin displacement, which is considerably later than at 14 mm as predicted by the model. The experiments also demonstrated several cycles of loading and unloading that resulted in a step-wise pattern in the force-displacement response, which was not captured by the model. Despite the differences near the initial rapid unzipping of the adhesive joint, the numerical model eventually matches well with the experimental rate of propagation after roughly 35 mm of pin displacement. The discrepancies between the experiments and the simulation at the initial rapid unloading phase

may be attributed to the fact that the steel adherend may be dominating the initial loading response, and the steel model was not adequately describing the loading and deformation behavior of the tube. In addition, the rate of propagation was directly related to the pin displacement at which propagation starts, i.e. the later the starting pin displacement, the more elastic energy is stored, and the more rapid the crack propagates. Therefore, a second local metric was chosen, where the crack propagation was plotted against the tracked vertical crack tip opening, thereby eliminating the consideration of when the propagation started and also minimizing the effect of the base metal adherend on the rate of crack propagation. As shown in Figure 6.26, by choosing a metric that assessed the behavior of the adhesive joint and the cohesive model as directly as possible, the predicted responses were able to correlate well with the experimental results. Note that only one test from each of fully martensitic and soft flange tests were tracked for this metric, since the previous results have shown that there was a high consistency between each test.

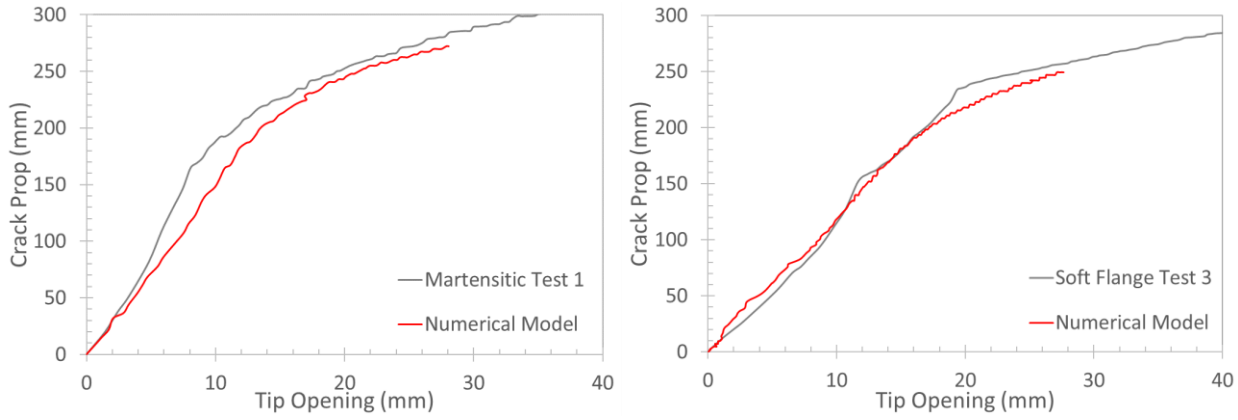

Figure 6.26: Crack propagation *vs.* tip opening response for fully martensitic and soft flange Caiman tests, showing better correlation between model and simulation with a metric that minimizes effect of base metal adherend deformation

Overall, the Caiman models were in excellent agreement with the experiments in terms of the loading response (Figure 6.27), deformation pattern, and crack propagation behavior. Looking at the tracking of crack length vs. pin displacement (Figure 6.25) for the fully martensitic specimens and model, a 2 mm difference in onset of crack initiation corresponded to approximately 12.5% off of the experimentally observed value. This difference was likely due to small differences in the predicted elastic deformation of the unbonded tube section, which could be caused by limitations of the steel constitutive model, or geometric differences between the model and the specimens, or both. Similarly, the tracking of crack length vs. pin displacement (Figure 6.25) for the soft flange specimens and model further suggest inadequacies in the steel model, in which the step-wise crack propagation behavior was not predicted.

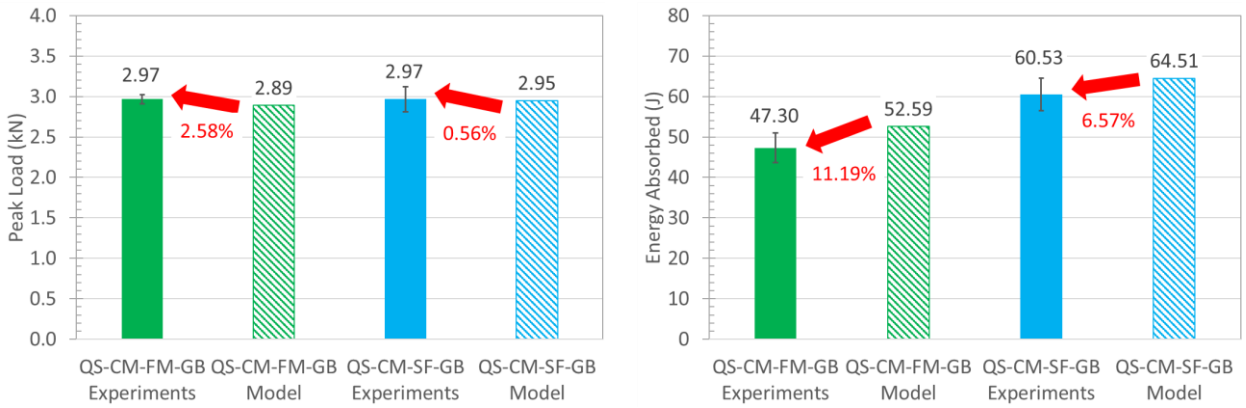

Figure 6.27: Comparison of peak forces (left) and energy absorptions (right) of QS-CM-FM-GB and QS-CM-SF-GB experiments *vs.* their respective models

Chapter 7 Conclusions and Recommendations

7.1 Conclusions

The following conclusions can be drawn from the experiments conducted in this research:

1. Surface preparation was identified to be a critical factor in ensuring cohesive failure. As-formed surfaces could experience interfacial failure, leading to lower joint strength and ultimately lower peak force and energy absorption.
2. The novel shimming technique developed to bond structures enabled uniform adhesive coverage and consistent bond line thickness throughout the flange. This technique could potentially be adapted to hybrid joints involving mechanical fasteners and adhesives.
3. Structural adhesive (IRSA 07333, 3M) can be used to join tailor hot stamped ultra-high strength steel and achieve consistent loading response, provided that proper steps for surface preparation are performed.
4. Despite physically using a wider blank, the measured Vicker's hardness of fully martensitic and soft flange hat sections agreed with Omer (2014) and Prajogo's (2015) models respectively (within 10% difference) (Figure 3.12). On the other hand, the formed three zone hat sections developed distinct differences from Omer's (2014) model, in which the averaged percentage difference across the hat section was 11.2%, with the highest difference of 24.2% on the side wall at the center of the 400 °C section (365 mm mark from the martensitic end). Another notable difference of 19.2% was located at the top surface of the 700°C section (where the fold initiator was). This area was critical in establishing the crush or impact pattern, and the difference resulted in

higher predicted peak force in the quasi-static axial crush, and less stable deformation mode in the dynamic axial crush experiment

The following conclusions can be drawn from the numerical models of the conducted experiments:

5. Due to the complexity of the forming operation as well the formulation of the numerical model, the three zone samples had a different hardness distribution compared to Omer's (2014) model. This led to differences in the loading response and the deformation pattern, which was corrected by modifying the three zone model to more reflect the measured physical hardness distribution.
6. In the three-point bend simulations, the CZM adhesive model was able to capture the abrupt joint failure in the 1.8 mm model at a similar displacement as observed in the experiment, but predicted the same failure in the 1.2 mm model at a much later displacement. The exact cause of this delay in predicted displacement-to-failure was uncertain, however it was suspected that the piecewise linear plasticity model of the base metal adherend was not accurately describing the deformation behavior of the physical part, therefore altering the transfer of load to the adhesive joint.
7. The three zone axial crush models demonstrated the importance of having an accurate mapping of hardness profile (and thus the correct flow stress curves) on the loading response and deformation pattern of the specimens.
8. The loading response of the Caiman models was in excellent agreement with the experiments, and the Caiman tracking results demonstrate that the CZM adhesive model could predict crack extension behavior with good accuracy.

9. Overall, the predicted global loading response correlated well with the measured response for all experiments in the initial load up and to peak force. With a few exceptions, the CZM adhesive model was able to predict the structural response of bonded components within 16%, based on kinetics and kinematics measured in the experimental tests.

7.2 Recommendations for Future Research

1. For future research, the three zone die should be modified such that shimming is possible for both heated zones to ensure a uniform contact across the entire hat section during forming and quenching. This will develop more pronounced individual zones of the hat section, which may improve their impact response
2. With respect to the bonding procedure, the recommendation for future research of similar geometry is to develop a more user-friendly bonding fixture such that the steel bars can be tightened with clamps that are driven simultaneously on each side of the flange. By applying a uniform force across the entire steel bar as opposed to at a singular point with the c-clamps, the adhesive will spread more evenly and consistently. In addition to better joint quality, another benefit with this method is an increased throughput by reducing bonding time.
3. It can also be worthwhile to develop another simple fixture for measuring the force required to flatten the warpage in the flange due to hot forming. This value can be used in numerical models to accurately represent residual stresses in the joint.

4. Another recommendation for improving experimental consistency is to machine out inserts that structurally support the three-point bend specimens to encourage bending without excessive collapse of the top hat section. The inserts should be made out of a material with readily available properties so that they can be accurately modeled in a FE simulation.
5. For the numerical models of tailored specimens, systematic error could be minimized by running the wider blank used in this work through a forming simulation similar to Omer (2014) and Prajogo's (2015) work to obtain a hardness distribution and geometric dimensions more representative of the physical hat sections produced. While the manual remapping performed on the three zone axial crush model was a simple solution with good results, the hat section models produced by the forming model may contain more fidelity for a wider range of loading scenarios.
6. An area of potential improvement for axial crush models is to model the formation of the fold initiators, rather than repositioning the nodes to create the fold imitator geometry without the corresponding forming history. With the inclusion of the forming history, the model may better predict the initiation and the continual deformation pattern of the bonded tube during an axial crush event.
7. Lastly, although the element size of 2.5 mm is in accordance with automotive norms, it could be beneficial to perform a mesh refinement study to obtain the grid convergence index for the current models.

References

3M (2012). Choosing and Using a Structural Adhesive. Viewed 14 June 2019, <https://multimedia.3m.com/mws/media/795693O/choosing-and-using-a-structural-adhesive-white-paper.pdf>

3M Canada (2015). 3M™ Impact Resistant Structural Adhesive. Viewed 20 April 2019, <https://multimedia.3m.com/mws/media/1034654O/impact-resistant-structural-adhesive-brochure-canada.pdf>

Adams, RD, Comyn, J, Wake, WC (1997). Structural Adhesive Joints in Engineering. 2nd edn. London. Chapman & Hall

Adhesives & Sealants (2015). History of Adhesives. Viewed 20 April 2019, <https://www.adhesives.org/resources/knowledge-center/aggregate-single/the-history-of-adhesives>

Åkerström, P, Bergman, G, & Oldenburg, M (2007). Modelling and Simulation in Materials Science and Engineering Numerical implementation of a constitutive model for simulation of hot stamping Numerical implementation of a constitutive model for, 15(2), 105–119. https://doi.org/10.1088/0965-0393/15/2/007

Alfredsson, KS, Biel, A, & Salimi, S (2015). International Journal of Adhesion & Adhesives Shear testing of thick adhesive layers using the ENF-specimen. International Journal of Adhesion and Adhesives, 62, 130–138. https://doi.org/10.1016/j.ijadhadh.2015.07.008

Anon, 2014. Audi A8: steel makes a comeback. ArcelorMittal USA. Viewed 5 March 2019, <https://usa.arcelormittal.com/news-and-media/our-stories/2017/may/05-11-2017>

Arrese, A, Insausti, N, Mujika, F, Perez-Galmes, M, & Renart, J (2019). A novel experimental procedure to determine the cohesive law in ENF tests. Composites Science and Technology, 170, 42–50. https://doi.org/10.1016/j.compscitech.2018.11.031

ASTM D3433-99 (2014). Standard Test Method for Fracture Strength in Cleavage of Adhesives in Bonded Metal Joints. American Society for Testing and Materials: West Conshohocken, PA.

Bardelcik, A, Ghavam, K, George, G, Worswick, MJ (2011). An Impact Model of a Hot Stamped Lab-Scale B- Pillar with Tailored Properties, in 3rd International Conference on Hot Sheet Metal Forming of HighPerformance Steel, Kassel, Germany, 2011.

Bardelcik, A, Salisbury, CP, Winkler, S, Wells, MA, & Worswick, MJ (2010). International Journal of Impact Engineering Effect of cooling rate on the high strain rate properties of boron steel. International Journal of Impact Engineering, 37(6), 694–702. https://doi.org/10.1016/j.ijimpeng.2009.05.009

Bardelcik, A, Worswick, MJ, Winkler, S, & Wells, MA (2012). A strain rate sensitive constitutive model for quenched boron steel with tailored properties. International Journal of Impact Engineering, 50, 49–62. https://doi.org/10.1016/j.ijimpeng.2012.06.007

Benevento, M (2016). Adhesives Helping OEMs Push the Performance Envelope with Lightweight Multi-Material Structures. Adhesives & Sealants. Viewed 30 March 2019,

<https://www.adhesives.org/resources/knowledge-center/aggregate-single/adhesives-helping-oems-push-the-performance-envelope-with-lightweight-multi-material-structures>

Boqaileh, K (2015). Experimental Testing and Modelling of Adhesively Joined T-structures. MASc. University of Waterloo

Budhe, S, Ghumatkar, A, Birajdar, N, & Banea, MD (2015). Effect of surface roughness using different adherend materials on the adhesive bond strength. Applied Adhesion Science, 3(1), 0–9. https://doi.org/10.1186/s40563-015-0050-4

Campilho, RDSG, Banea, MD, Neto, JABP, & Da Silva, LFM (2013). Modelling Adhesive Joints with Cohesive Zone Models: Effect of the Cohesive Law Shape of the Adhesive Layer. International Journal of Adhesion and Adhesives, 44, 48–56. https://doi.org/10.1016/j.ijadhadh.2013.02.006

Campilho, RDSG, de Moura, MFSF, & Domingues, JJMS (2005). Modelling single and double-lap repairs on composite materials. Composites Science and Technology, 65(13), 1948–1958. https://doi.org/10.1016/j.compscitech.2005.04.007

Cavallini, G, Davi, G, & Milazzo, A (2006). Boundary element modeling and analysis of adhesive bonded structural joints, 4(1), 31–48. https://doi.org/10.14713/ejbe.v4i1.773

Chastel, Y, & Passemard, L (2014). Joining technologies for future automobile multi-material modules. Procedia Engineering, 81, 2104–2110. https://doi.org/10.1016/j.proeng.2014.10.293

Chaves, FJP, Da Silva, LFM, De Moura, MFSF, Dillard, DA, & Esteves, VHC (2014). Fracture Mechanics Tests in Adhesively Bonded Joints: A Literature Review. The Journal of Adhesion, 90(12), 955–992. https://doi.org/10.1080/00218464.2013.859075

Courant, R. (1943). Variational methods for the solution of problems of equilibrium and vibrations. Bull. Am. Math. Soc. 49, 1–23 (1943)

Cricrì, G (2018). Cohesive law identification of adhesive layers subject to shear load: The Twice Notched Flexure Test. Procedia Structural Integrity, 12, 492–498. https://doi.org/10.1016/j.prostr.2018.11.069

da Silva, LFM, & Campilho, RDSG (2012). Advances in numerical modelling of adhesive joints. SpringerBriefs in Applied Sciences and Technology.

Dastjerdi, AK, Pagano, M, Kaartinen, MT, Mckee, MD, & Barthelat, F (2012). Acta Biomaterialia Cohesive behavior of soft biological adhesives: Experiments and modeling. Acta Biomaterialia, 8(9), 3349–3359. https://doi.org/10.1016/j.actbio.2012.05.005

Dastjerdi, AK, Tan, E, & Barthelat, F (2013). Direct Measurement of the Cohesive Law of Adhesives Using a Rigid Double Cantilever Beam Technique. Experimental Mechanics, 53(9), 1763–1772. https://doi.org/10.1007/s11340-013-9755-0

de Barros, S, Kenedi, PP, Ferreira, SM, Budhe, S, Bernardino, AJ, & Souza, LFG (2017). Influence of mechanical surface treatment on fatigue life of bonded joints. Journal of Adhesion, 93(8), 599–612. https://doi.org/10.1080/00218464.2015.1122531

Deb, A, Chou, CC, Srinivas, GR, Gowda, S, & Kurnool, G (2016). Behavior of Adhesively Bonded Steel Double Hat-Section Components under Axial Quasi-Static and Impact Loading. SAE 2016 World Congress and Exhibition, 2016–April(April). https://doi.org/10.4271/2016-01-0395

Dogan, F., Hadavinia, H., Donchev, T., & Bhonge, P. (2012). Delamination of Impacted Composite Structures by Cohesive Zone Interface Elements and Tiebreak Contact. Central European Journal of Engineering. https://doi.org/10.2478/s13531-012-0018-0

Eller, TK, Greve, L, Andres, MT, Medricky, M, Hatscher, A, Meinders, VT, & Van Den Boogaard, AH (2014). Plasticity and fracture modeling of quench-hardenable boron steel with tailored properties. Journal of Materials Processing Technology, 214(6), 1211–1227. https://doi.org/10.1016/j.jmatprotec.2013.12.015

Elmer's Products Inc. (2015). Krazy Glue Safety Data Sheet. Viewed 9 May 2019, <http://www.krazyglue.com/docs/default-source/MSDS-Sheets/skg0583.pdf?sfvrsn=8>

Fernandes, RL, Campilho, RDSG, Leitão, ACC, & Azevedo, JCS (2015). Numerical evaluation of the direct method for cohesive law extraction in shear by the End-Notched Flexure test. Procedia Engineering, 114, 94–101. https://doi.org/10.1016/j.proeng.2015.08.046

George, R (2011). Hot Forming of Boron Steels with Tailored Mechanical Properties Experiments and Numerical Simulations. MASc. University of Waterloo

George, R, Bardelcik, A, & Worswick, MJ (2012). Hot forming of boron steels using heated and cooled tooling for tailored properties. Journal of Materials Processing Technology, 212(11), 2386–2399. https://doi.org/10.1016/j.jmatprotec.2012.06.028

Ghumatkar, A, Budhe, S, Sekhar, R, Banea, MD, & De Barros, S (2016). Influence of adherend surface roughness on the adhesive bond strength. Latin American Journal of Solids and Structures, 13(13), 2356–2370. https://doi.org/10.1590/1679-78253066

Gowda, S, Deb, A, Kurnool, G, & Chou, C (2017). Prediction of the Behaviors of Adhesively Bonded Steel Hat Section Components under Axial Impact Loading. SAE Technical Papers, 2017–March(March). https://doi.org/10.4271/2017-01-1461

Gowda, S, Deb, A, Kurnool, G, & Chou, CC (2018). Behavior of Adhesively Bonded Steel Double-Hat Section Components under Lateral Impact Loading. SAE Technical Papers, 2018–April, 1–8. https://doi.org/10.4271/2018-01-1447

Green, D. W., Winandy, J. E., & Kretschmann, D. E. (1999). Mechanical Properties of Wood. In Wood Handbook. Viewed 16 June 2019, <https://www.fpl.fs.fed.us/documnts/fplgtr/fplgtr113/ch04.pdf>

Hagerty, JR, & Ramsey, M (2014). 'Super Glues Are the Secret to Making Cars Lighter'. The Wall Street Journal. Viewed 30 March 2019, <https://www.wsj.com/articles/super-glues-are-the-secret-to-making-cars-lighter-1410196062>

Haufe, A, Neukamm, F, Feucht, M, DuBois P & Borvall, T (2010). A comparison of recent damage and failure models for steel materials in crashworthiness application in LS-DYNA. 11th International LS-DYNA Users Conference

He, X. (2011). A review of finite element analysis of adhesively bonded joints. International Journal of Adhesion and Adhesives, 31(4), 248–264. https://doi.org/10.1016/j.ijadhadh.2011.01.006

Honda Canada (2017). Viewed 30 March 2019, <https://www.honda.ca/newsdetails/nca/en/news/release/Dramatic-Design-of-Reimagined-2018-Honda-Accord-Unveiled>

Hrennikoff, A. (1941). Solution of problems of elasticity by the framework method. Journal of applied mechanics 8.4: 169–175.

ISO 25217:2009 (2009). Adhesives – Determination of the Mode 1 Adhesive Fracture Energy of Structural Adhesive Joints Using Double Cantilever Beam and Tapered Double Cantilever Beam Specimens. International Organization for Standardization: Geneva, CH.

Kelly, G. (2004). Joining of Carbon Fibre Reinforced Plastics for Automotive Applications. PhD Thesis. Royal Institute of Technology

Kim, H, & Kedward, KT (2001). Stress Analysis of Adhesively-bonded Joints Under In-plane Shear Loading Stress Analysis of Adhesively-bonded Joints Under In-plane Shear Loading. The Journal of Adhesion, 76(1), 1–36. https://doi.org/10.1080/00218460108029615

Landrock, A., & Ebnesajjad, S. (2008). Adhesives Technology Handbook (2nd ed.).

Lanzerath, H, & Pasligh, N (2014). Benefit of Structural Adhesives in Full Car Crash Applications. SAE Technical Paper. https://doi.org/10.4271/2014-01-0811.Copyright

Lee, MH, Kim, HY, & Oh, SI (2006). Crushing test of double hat-shaped members of dissimilar materials with adhesively bonded and self-piercing riveted joining methods. Thin-Walled Structures, 44(4), 381–386. https://doi.org/10.1016/j.tws.2006.04.012

Liao C-H, Watson B, Worswick MJ, Cronin DS, Soldaat R, Malcom S, Nielson K (2016) Adhesively Bonded High Strength Steel Axial Crush Tube Investigation, ArcelorMittal Knowledge Innovation Summit, 2016

Liao, CH, Watson B, Worswick, MJ, Cronin, DS (2017). 'Mode I Rigid Double Cantilever Beam Test and Analysis Applied to Structural Adhesives.' Dynamic Behavior of Materials, Volume 1, Conference Proceedings of the Society for Experimental Mechanics Series, pp.73-81

Liu B, Liao C-H, Watson B, Cronin DS, Worswick M, Soldaat R, Bernert W, Malcolm S, Smith A, Nielson K, Brandys F. (2017). Adhesively Bonded Hot Formed Usibor® Hat Sections in Axial Crush and Three-Point Bend Loading, ArcelorMittal Knowledge Innovation Summit, June 13, 2017.

Liu, H, Jin, X, Dong, H, & Shi, J (2011). Martensitic microstructural transformations from the hot stamping, quenching and partitioning process. Materials Characterization, 62(2), 223–227. https://doi.org/10.1016/j.matchar.2010.12.003

Lonardo, PM, & Bruzzone, AAG (1989). Influence of Surface Roughness Parameters on the Mechanical Strength in Metal Gluing. CIRP Annals, 38(1), 571–574.

LSTC (2012). LS-DYNA KEYWORD USER'S MANUAL VOLUME II: Material Models. Version 971 R6.1.0

LSTC (2012). LS-DYNA KEYWORD USER'S MANUAL VOLUME II: Material Models

Lu, J, Newaz, GM, & Gibson, RF (2004). The role of adhesive in the mechanical response of adhesively bonded aluminum hat sections under axial compression. International Journal of Solids and Structures, 41(16–17), 4757–4767. https://doi.org/10.1016/j.ijsolstr.2004.02.042

Marzi, S, Hesebeck, O, Brede, M, & Kleiner, F (2009). A Rate-Dependent Cohesive Zone Model for Adhesively Bonded Joints Loaded in Mode I A Rate-Dependent Cohesive Zone Model for Adhesively. Journal of Adhesion Science and Technology, 23(6), 881–898. https://doi.org/10.1163/156856109X411238

May, M, Hesebeck, O, Marzi, S, Böhme, W, Lienhard, J, Kilchert, S, Brede, M, Hiermaier, S (2015). Rate dependent behavior of crash-optimized adhesives – Experimental characterization, model development , and simulation. ENGINEERING FRACTURE MECHANICS, 133, 112–137. https://doi.org/10.1016/j.engfracmech.2014.11.006

Mcgregor, I. J., Seeds, A. D., & Nardini, D. (1990). The Design of Impact Absorbing Members for Aluminum Structured Vehicles. SAE Technical Paper.

Merklein, M, Wieland, M, Lechner, M, Bruschi, S, & Ghiotti, A (2016). Hot stamping of boron steel sheets with tailored properties: A review. Journal of Materials Processing Technology, 228, 11–24. https://doi.org/10.1016/j.jmatprotec.2015.09.023

Mori, K, Bariani, PF, Behrens, BA, Brosius, A, Bruschi, S, Maeno, T, … Yanagimoto, J (2017). Hot stamping of ultra-high strength steel parts. CIRP Annals - Manufacturing Technology, 66(2), 755–777. https://doi.org/10.1016/j.cirp.2017.05.007

O'keeffe, C (2018). Investigation of Resistance Spot Weld Failure in Tailored Hot Stamped Assemblies. MASc. University of Waterloo.

Omer, K (2014). Development and Testing of a Hot Stamped Axial Crush Member with Tailored Properties. MASc. University of Waterloo

Omer, K, ten Kortenaar, L, Butcher, C, Worswick, M, Malcolm, S, & Detwiler, D (2017). Testing of a hot stamped axial crush member with tailored properties – Experiments and models. International Journal of Impact Engineering, 103, 12–28. https://doi.org/10.1016/j.ijimpeng.2017.01.003

Peroni, L, Avalle, M, & Belingardi, G (2009). Comparison of the energy absorption capability of crash boxes assembled by spot-weld and continuous joining techniques. International Journal of Impact Engineering, 36(3), 498–511. https://doi.org/10.1016/j.ijimpeng.2008.06.004

Petrie, E. M. (2006). Epoxy adhesive formulation. Handbook of Thermoset Plastics. https://doi.org/10.1036/0071455442

Prajogo, Y (2015). Hot Stamping of a Boron Steel Side Impact Beam with Tailored Flange Properties. MASc. University of Waterloo

Ripling, EJ, Mostovoy, S, and Patrick, RL (1964). Application of Fracture Mechanics to Adhesive Joints. Adhesion, STP360-EB, Committee D-14, Ed., ASTM International, West Conshohocken, PA, pp. 5-19, https://doi.org/10.1520/STP44560S

Schuecker, C, & Davidson, BD (2000). Evaluation of the accuracy of the four-point bend end-notched ¯ exure test for mode II delamination toughness determination. Composites Science and Technology, 60(11), 2137–2146.

Shields, J (1984). Adhesives Handbook, 3rd ed., Butterworth, London

Sønstabø, J. K., Morin, D., & Langseth, M. (2016). A Cohesive Element Model for Large-Scale Crash Analyses. 14th International LS-DYNA Users Conference.

Steiner P (2011). Adhesive Failure& Epoxy Failure. Viewed 20 April 2019, <http://theadhesivesexpert.com/adhesives-failure-epoxy-failure/>

Symietz, D (2005). Structural Adhesive Bonding: The Most Innovative Joining Technique for Modern Lightweight Design, Safety and Modular Concepts -Progress Report-. SAE International.

ten Kortenaar, L (2016). Failure Characterization of Hot Formed Boron Steels with Tailored Mechanical Properties. MASc. University of Waterloo

Trimiño, L. F., & Cronin, D. S. (2014). Non-direct similitude technique applied to the dynamic axial impact of bonded crush tubes. International Journal of Impact Engineering, 64, 39–52. https://doi.org/10.1016/j.ijimpeng.2013.10.001

Trimiño, L. F., & Cronin, D. S. (2016). Evaluation of Numerical Methods to Model Structural Adhesive Response and Failure in Tension and Shear Loading. Journal of Dynamic Behavior of Materials, 2(1), 122–137. https://doi.org/10.1007/s40870-016-0045-7

Trimiño, LF (2012). Analysis and Performance of Adhesively Bonded Crush Tube Structures. MASc. University of Waterloo.

Tummers, M., Omer, K., Abedini, A., Peister, C., Butcher, C., Worswick, M. J., … Soldaat, R. (2018). Introduction of a 1000 MPa crush tip within a Usibor® 1500-AS axial crush rail using in-die heated hot stamping. IOP Conference Series: Materials Science and Engineering, 418(1). https://doi.org/10.1088/1757-899X/418/1/012126

U.S. Department of Energy (2015). Multi-Material Lightweight Vehicles. Viewed 18 April 2019, <https://www.energy.gov/sites/prod/files/2015/06/f24/lm072_skszek_2015_o.pdf>

U.S. Department of Transportation (2012). Corporate Average Fuel Economy for MY 2017-MY2025 Passenger Cars and Light Trucks.

Vable, M, & Reddy Maddi, J (2006). Boundary element analysis of adhesively bonded joints. International Journal of Adhesion and Adhesives, 26(3), 133–144. https://doi.org/10.1016/j.ijadhadh.2004.12.003

Vaissiere, L, Laurent, JP, Reinhardt, A (2002). Development of pre-coated boron steel for application on PSA Peugeot Citroen and Renault bodies in white, International body engineering conference & exhibition

Wang, RX, Cui, J, Sinclair, AN, & Spelt, JK (2003). Strength of adhesive joints with adherend yielding: I. Analytical model. The Journal of Adhesion, 79(1), 23–48. https://doi.org/10.1080/00218460309561

Watson B, Liu B, Liao CH, Cronin DS, Worswick MJ, Soldaat R, Bernert W, Brown C, Malcom S, Smith3 A, Nielson K, Brandys F. (2018) Single Lap Shear Testing and Modelling of Usibor® 1500-AS Bonded with 3M Impact Resistant Structural Adhesive 7333, 2018 ArcelorMittal Global R&D Innovation Seminar, Hamilton, Canada

Watson, B, Liao, CH, Worswick, MJ, & Cronin, DS (2018). Mode I traction-separation measured using rigid double cantilever beam applied to structural adhesive. Journal of Adhesion, 1–21. https://doi.org/10.1080/00218464.2018.1502666

Xu, W, & Li, G (2010). International Journal of Adhesion & Adhesives Finite difference three-dimensional solution of stresses in adhesively bonded composite tubular joint subjected to torsion. International Journal of Adhesion and Adhesives, 30(4), 191–199. https://doi.org/10.1016/j.ijadhadh.2009.12.007

Yahyaie, H., Ebrahimi, M., Tahami, H. V., & Mafi, E. R. (2013). Progress in Organic Coatings Toughening mechanisms of rubber modified thin film epoxy resins. Progress in Organic Coatings, 76(1), 286–292. https://doi.org/10.1016/j.porgcoat.2012.09.016

Yang, X, Xia, Y, Zhou, Q, Wang, PC, & Wang, K (2012). Modeling of high strength steel joints bonded with toughened adhesive for vehicle crash simulations. International Journal of Adhesion and Adhesives, 39, 21–32. https://doi.org/10.1016/j.ijadhadh.2012.06.007

Yee, A., & Pearson, R. (1986). Toughening mechanisms in elastomer-modified epoxies, 21, 2462–2474.

Zachariah, A. (2006). Finite Element Modelling of Adhesive Interface between Steel and CFRP. MASc Thesis. Chalmers University of Technology.

Zhang, XM, Yue, TM, & Man, HC (1997). Enhancement of ceramic-to-metal adhesive bonding by excimer laser surface treatment. Materials Letters, 30(5–6), 327–332. https://doi.org/10.1016/S0167-577X(96)00229-7